UNIVERSITY OF PAVIA
Department of Brain and Behavioural Science
PhD course in Psychology, Neuroscience and Medical Statistics

Doctorate cycle XXXII

Graph theory applied to neuroimaging data reveals key functional connectivity alterations in brain of behavioral variant Frontotemporal Dementia subjects

Advisor:

Mario Grassi

PhD candidate:

Valentina Saba

Academic year

2016-2019

Alla mia famiglia, a coloro che non ci sono più,

a chi, con il suo Amore, mi ha accompagnata in questa avventura.

To my family, to those who left us,

to the man who, with his Love, drove me in this adventure.

Acknowledgemens

Al termine dell'esperienza universitaria, ringrazio il Prof. Mario Grassi per aver messo a disposizione la sua grande preparazione ed esperienza tecnico-scientifica in questi tre anni, in un ambito, per me, del tutto nuovo.

Ringrazio in modo particolare anche l'equipe del Centro per le Malattie Neurodegenerative (Università di Brescia) per aver messo a nostra disposizione i dati relativi allo studio e per aver costantemente collaborato per lo sviluppo di questo progetto.

Ringrazio di cuore il Dott. Fernando Palluzzi per il fondamentale contributo a questo lavoro, sia per la sua intelligenza che per la sua grande disponibilità.

Infine, vorrei ringraziare tutti i volontari dello studio che costituiscono l'anima della ricerca scientifica e chi, anche solo con un parere, ha dato un contributo a questo lavoro.

I miei speciali ringraziamenti vanno a tutti coloro che, con il cuore, mi sono sempre stati accanto in questi anni. Grazie mille alla mia famiglia. Grazie mille a Fernando. Grazie agli amici e ai colleghi, compagni indiscussi di questa avventura.

Grazie ai miei angeli che non ci sono più.

Valentina

Index

1. Preface

Brain functional architecture and anatomical structure have been intensively studied to generate efficient models of its complex mechanisms. Functional alterations and cognitive impairments are the most investigated aspects in the recent clinical research as distinctive traits of neurodegeneration. Although specific behaviours are clearly associated to neurodegeneration, information flow breakdown within the brain functional network, responsible to deeply affect cognitive skills, remains not completely understood. Applying graph theoretical methods to neuroimaging techniques is becoming popular in the study of brain dysfunctions. Although conventional graph theoretical analyses are helpful in dissecting disease mechanisms, the methodology is significantly hampered by several arbitrary choices. Descriptive metrics and their normalisation, network type (e.g., weighted versus unweighted), threshold values (fixed cut-off, fixed average degree, fixed edge density, or multiple thresholds over a range of values) are some of the critical points making network results difficult to reproduce. In addition, several network metrics and node centrality indices may assume different importance at either local or global scale, whether the graph model accounts for time variant (i.e., dynamic) or invariant (i.e., static) connectivity, and depending on the parcellation type (data resolution), according to Independent Component Analysis (ICA) and specific atlases. This original research project aimed to investigate large-scale functional network alterations through fMRI data, inspecting global and local network properties in patients affected by behavioural variant Frontotemporal Dementia (bvFTD), compared with a group of healthy controls (HC). The method consists in a novel graph procedure (MST-based) that combines individual tree-based global evidences and two-group topological aspects (nodes cluster and edges partition). The primary focus of this work was to propose a novel approach that might go beyond the classical network binarization methodologies. Currently, there are no objective ways of fixing threshold value to find main information flow routes and filter noise out. Resulting network properties strongly depend on how we construct it, and researchers are often forced to explore these properties across a wide range of different candidate thresholds. For our brain functional study, we decided to apply a method focused on useful network topology properties, but independent on threshold choices. When comparing graphs with the same number of nodes (N) and edges (N-1), the minimum spanning tree (MST) is an unambiguous method for brain network analysis avoiding methodological

biases and implicitly considering connectivity integration/costs trade-off. Nevertheless, MST performances were challenged both against conventional graph theory approaches (using threshold-based binarization), and model selection-based strategies. Secondly, we aimed to propose a methodology able to associate a complex biological system architecture to its functional properties. Despite cognitive impairments (generally called Dementia) damage a significative percentage of world population, the mechanisms that connect risk factors, onset and progression of Dementia remain less understood. Therefore, we focused on shortest-paths and information-flow based-model (MST) that better shows structural and functional link properties of the brain, comparing MST topological organization between bvFTD patients and HCs. The thesis is divided in eight chapter, where the first four introduce (i) the foundamental Graph Theory concepts including global and local network measure, complex network models and its application in functional brain studies, (ii) the brain topological organization, explaining the trade-off between wiring and metabolic costs, and (iii) the clinical, genetic and neuro-functional traits of Frontotemporal Dementia phenotypes, including causal relationships among them. MST-based model have been discussed in Chapters 5, including the principles and the guidelines to perform global (MST parameters and stronger disorder limit) and topological network analysis. Chapter 6 shows the Results of entire analysis, while Chapters 7 and 8 concern work Discussion and Conclusion. The latter describe in details MST performance related to functional alterations and its neuroscientific implications in bvFTD.

2. Graph theory concepts

Real biological systems usually show a high complexity in terms of structural and functional organization of their components, often characterized by sudden configuration changes, and non-stationary behaviours. Biological complexity may give rise to an exponentially large number of interactions among system elements, making an exhaustive analysis impractical or even impossible.

Mathematical methods offer a wide range of models to represent these systems, allowing a simplification of architectures with schematization of their interactions at different levels of complexity (Telesford et al., 2011). Network-based models are among the most powerful instruments used to describe and study complex systems properties (Ghasemi et al., 2014; Albert and Barabási, 2002). A network consists in a set of nodes (or vertices) and links (or edges) that constitute the node connections (Rutter et al., 2013). For example, in biological networks, nodes can be genes and/or protein and the relative links represent perturbation routes among them, as well as, nodes can be interpreted as brain areas, and their connections represents functional or structural relationships between them. In mathematical terms, a simple graph is indicated as $G = (V, E)$, i.e., as a function of a nodes set *V* and an edge set *E* (Estrada 2015; Rutter et al., 2013).

Information transfer along edges can be described through a graph theory concept of a *walk* (Telesford et al., 2011). A walk does not include movement restrictions, it describes a communication from one node to another, and this information can return to a node more than once or reuse an edge. The most restricted walk type is called *path*, in which neither nodes nor edges can be reused (Telesford et al., 2011). A graph can include closed walk, termed *cycle*, in which nodes and edges are distinct (except the first and the last node) drawing a path that returns to the first node (Estrada 2015; Kaiser 2011). In addition, in a graph can be found *loops*, i.e. edges that connect a node itself (Kaiser 2011).

A matrix is an efficacious and common computational format to represent a network, generally called *adjancency matrix* (A) (Estrada 2015). A is a square matrix, with an equal number *n* of rows and columns (n-by-n matrix), in which the single element is indicated as *Aij* (Estrada 2015).

2. 1. Graph measures

A network allows to characterize a complex system at different levels, using different metrics to analyse an entire network at global and local scales (Kaiser 2011). A summary of common network metrics is provided in **Table 1**, in which we described the properties of binary and undirected graphs, consistent with this network-based study (see Materials and methods, chapter 5).

Starting from the local scale, network properties concern its fundamental components: nodes and edges (**Table 1**; Kaiser 2011). Different edges types influence the local network metrics, as well as the resulting graph. Specifically, edges can be weighted or unweighted (binary). In the former, edges weights assume continuous or discrete (ordinal) values, showing connections strength. In the latter, weights are either 0 or 1, indicating the absence or presence of a connection, respectively. Therefore, a network with weighted edges is called *weighted graph*, while a binary network is called *unweighted graph*. A weighted graph can be converted to a binary graph applying a threshold: weights above threshold assumes 1, otherwise 0. Calculation and interpretation of network measures are easier in binary graphs respect to others, even if an objective threshold choice could be difficult (Kaiser 2011). Beside weighted or unweighted graphs, networks may be classified in directed or undirected. In a directed network, links show the direction of information transfer, while in an undirected network, information may travel in both directions. This concept is fundamental to establish nodes and edges centrality. Typically, a restricted number of nodes and edges are the most influential in a large network, in terms of connectivity and information spreading (Ghasemi et al., 2014; Kaiser 2011). One of the most representative local measures of node centrality is the *degree* (*k*), defined as the sum of its incoming and outgoing connections (**Table 1**). Local measures consider also the neighbours of a node. They involve all nodes that directly project to a node or receive from that node. Connectivity measure between neighbours is defined as *local clustering coefficient*, expressed as the ratio between the number of real connections between neighbours and the total number of possible connections between neighbours (**Table 1**). Node importance is often described as a proportion of how many shortest paths pass through a node, among all the shortest paths of the network. A shortest path is defined as the path with lowest number of links between two nodes (**Table 1**). To establish the number of shortest paths for a node, is necessary to calculate the shortest paths between all pairs of

nodes, and then to count how many shortest paths include a certain node. This measure can be expressed as the absolute number of shortest paths passing through one node (*stress centrality*) or the relative frequency of the shortest paths traversing one node over all the shortest paths in the network (*betweenness centrality*). The latter property is called node *betweenness* (**Table 1**), but in similar way is possible to consider also the *edge betweenness*, defined as the frequency of shortest paths containing a certain edge. Lastly, the *closeness centrality* (**Table 1**) is expressed as the reciprocal of total distance of a node to any other node of the network. A node with high closeness indicates that it is necessary a small number of steps to reach the others node in the network.

A network can be also characterized from its global properties (**Table 1**; Kaiser 2011). This detail level is useful to compare networks among different groups or among different subjects within the same group (Kaiser 2011). Indeed, aggregate measures are less affected by network specificity (e.g., number of nodes, number of edges). A commonly used property in networks comparison is the edges density, also called network connectivity, expressed as a proportion of existing edges in a graph respect all possible edges in the same graph (Kaiser 2011). In a direct graph with N nodes and E edges, each node can connect at most N - 1 other nodes, hence the edges density is equal to $d = E / ((N * (N - 1)))$. For undirected graph, the concept is the same, but a factor equal to 2 is added at the denominator to consider bidirectional links only one time: $d = E / ((2 * N * (N - 1)))$. An ideal case is when all potential links are real, corresponding to a connectivity value equal to 1. This phenomenon is rare in most biological systems, where we often observe low edges density values (Kaiser 2011).

In general, global properties describe two principal aspects of network elements: their segregation and integration tendency (Kaiser 2011; Rubinov and Sporns 2010; **Table 1**). Segregation is the capability to develop specialized processing within densely interconnected group of nodes. Firstly, it quantifies the presence of aggregation structures, commonly known as clusters or modules. As mentioned above, at local level, simple measures of segregation quantify the number of triangles around an individual node, as clustering coefficient. The mean of these local values for all network components constitute the "*global" clustering coefficient*. However, it can be heavily influenced by nodes with low degree, because it is normalized individually for each vertex. For this reason, sometimes a collectively normalized

measure is preferred, called *transitivity*. A more complete formulation of the segregation is the *modular structures* measure, because it can identify densely interconnected groups, combined with exact size and composition of these groups (Rubinov and Sporns 2010). As reported by Kaiser (2011), *modularity* is a single parameter quantifying functional blocks within network, that has received more attention in the last times (**Table 1**). It indicates the degree of graph subdivision in clearly delineated and nonoverlapping subnetworks.

Integration give information about communication quality, in terms of strength and efficiency (Kaiser 2011; Rubinov and Sporns 2010). This estimate is commonly based on the concept of path. Paths are sequences of nodes and edges, representing potential routes of information transfer between nodes in a graph. Their length is synonymous of integration strength, as well as of information flow efficiency: shorter paths allow a strong integration of graph components, with a higher power of information exchange. These notions are summarized by *characteristic path length L* measure, defined as average of shortest path length between all node pairs (**Table 1**). A complementary way to quantify the integration, is the inverse of average of shortest path length, known as *global efficiency* (**Table 1**). As reported by Rubinov and Sporns (2010), some authors consider global efficiency as a more effective measure of integration, because it is primarily influenced by shortest paths, contrarily to characteristic path length, primarily affected by long paths.

Table 1. Binary and undirected graph network metrics. Equations and description by Kaiser (2011) and Rubinov and Sporns (2010).

Measure	Equation	Description
Local measures		
Degree	$k_i = \sum_{j \in N} a_{ij}$	Number of links connected to a node. a_{ij} is the connection status between i and j: a_{ij} = 1 when link i, j exists, otherwise a_{ij} = 0 (a_{ii} = 0 for all i).
Shortest path length	$d_{ij} = \sum_{a_{uv} \in g_{i \leftrightarrow \mathrm{j}}} a_{uv}$	A path constituted by a lower number of walks; distance between nodes i and j. $g_{i \leftrightarrow \mathrm{j}}$ is the shortest path (geodesic) between i and j. $d_{ij} = \infty$ for disconnected pairs of nodes.
Betweenness centrality	$b_i = \sum_{h,j \in N} \frac{\rho_{hi}(i)}{\rho_{hi}}$	Relative frequency of how often that node is part of shortest paths. $\rho_{hi}(i)$ number of shortest paths between h and j that passes through i. ρ_{hi} number of shortest paths between h and j. Note: h≠j; h≠i; j≠i
Local clustering coefficient	$C_i = \frac{\Gamma_i}{k_i(k_i - 1)}$	Connectivity between neighbours referred to ith node. Γ_i is the edges betweennes of neighbors of i. k_i degree of the node i.
Closeness centrality	$L_i^{-1} = \frac{n-1}{\sum_{j \in N, j \neq i} d_{ij}}$	Reciprocal of total distance of a node to any other node of the network. n is the number of nodes, while d_{ij} is the shortest path length.

Number of triangles	$t_i = \frac{1}{2}\sum_{j,h\in N} a_{ij}\, a_{ih}\, a_{jh}$	Number of triangles around a node i. a_{xy} is the connection status between two nodes: a_{xy} = 1 when link x, y exists, otherwise a_{xy} = 0.
Segregation measures		
Clustering coefficient	$C = \frac{1}{n}\sum_{i\in N} C_i$	Mean of local clustering coefficient values of nodes. n is the number of nodes, while C_i is the local clustering coefficient of node i. $C_i = 0$ if $k_i < 2$.
Transitivity	$T = \frac{\sum_{i\epsilon N} 2t_i}{\sum_{i\epsilon N} k_i(k_i - 1)}$	Transitivity is another cluster coefficient but normalized collectively respect to the classic cluster coefficient. t_i is the number of triangles of node i, with degree equal to k_i.
Modularity	$M = \sum_{u\in M}\left[e_{uu} - \left(\sum_{v\in M} e_{uv}\right)^2\right]$	Subdivision in clearly delineated and nonoverlapping subnetworks. M are the graph modules, e_{uv} is the proportion of all links that connect nodes in module u with nodes in module v.
Integration measures		
Characteristic path length	$L = \frac{1}{n}\sum_{i\in N} \frac{\sum_{j\in N, j\neq i} d_{ij}}{n-1}$	Average of shortest path length between all node's pairs. n is the number of nodes, $d_{ij}$is the shortest path length of nodes pair i, j.
Global efficiency	$E = \frac{1}{n}\sum_{i\in N} \frac{\sum_{j\in N, j\neq i} d_{ij}^{-1}}{n-1}$	Inverse of average of shortest path length. n is the number of nodes, $d_{ij}$is the shortest path length of nodes pair i, j.

2. 2. Complex networks in biological systems

Graph theory is often called Complex Network Analysis. Although more studies aim to optimize complex system representation, the term “complex” introduce the concept of composite, i.e., dependent on several interacting variables, whose behaviour is hard to determinate. Thus, network representations of these system or complex networks will include their topological and structural complexities, pointing at the same time to schematise their features. Topology of network describes how the connections between elements of system are allocated (Fornito et al., 2015). Different topological characteristics have been used to introduce mathematical models able to reproduce dynamical and functional network properties (i.e., organization) observed in many biological systems, such as small-world and scale-free models. In contrast, random and regular network models show simpler structures determined through few parameters.

A random graph is often used as a standard null model used to test functional or architectural properties of other networks. Erdös-Rényi (1960) introduced the simplest model of this graph, defined as a set of nodes connected by edges in a random way. Starting from a specific number of isolated nodes (N), the probability p of being connected is the same for each pair of nodes, and its degree distribution follows a Poisson distribution (Estrada, 2015). A random graph shows a high connectivity level, with a short overall average path length, but a low local clustering index (Bullmore and Sporns, 2009).

Regular graph is characterised by nodes with the same degree r, in which the number of links is simply defined as r*N/2. Since each node has the same degree, it is impossible to define a degree distribution, but only a vertical straight line in correspondence to degree value (k) in the x-axis (Estrada, 2015). Opposite to random networks, a regular graph shows a higher clustering coefficient and a longer average path length (Bullmore and Sporns, 2009). Therefore, it is necessary to set N and p or N and k, to generate a random or regular network, respectively.

A key feature used to describe the behaviour and global properties of a complex network is the degree distribution P(k). Typically, many biological networks show a heavy-tailed P(k) distribution, characterized by the presence of few nodes with higher degree centrality than most network nodes (Barabasi and Albert, 1999). One of the most representative heavy-tailed

distribution is the power-law, in which the probability of a node having degree k is defined as P(k)~k^(-λ) (Estrada, 2015; Bullmore and Sporns, 2009). In biological systems, the exponent λ takes values between 2 and 3, in which the gradual decrease of degree distribution indicates an absence of a representative scale, from which the name “scale-free” derives (Bullmore and Sporns, 2009). Introduced by Barabási and Albert (1999), in a scale free model, P(k) follows a negative power of degree that means that the probability to find nodes with high degree will be low respect nodes with small degree. Especially known in molecular systems (Zhang and Horvath, 2005), a scale-free network is made through a process that favourably connects new nodes to nodes with higher degree centrality. Considering a lower connectivity capability of physically embedded networks, the power-law distribution can be substituted from a truncated power law distribution that better represent these networks (Bullmore and Sporns, 2009).

As introduced in chapter 2 and in this section, many complex network measures have been investigated in addition to degree distribution. Average path length and clustering coefficient play a key a role in complex network theory, and inspired researchers to build appropriate networks model to describe real systems (Wang and Chen, 2003).

In this regard, a popular concept in network theory is the definition of “small-world”, introduced through the study of social networks (Estrada, 2015). Small-world organization well represent human network relationships, characterised by a high local-level of clustering, and a general short distance between nodes (i.e., low average path length). This model, proposed by Watts and Strogatz (1998), shows hence intermediate properties between random and regular graphs (Bullmore and Sporns, 2009). Since that each node has about the same number of links, its connectivity distribution is called “exponential” or “homogeneous” network.

Beside social sciences, small-world network has been applied in several field, and particularly in Neuroscience for brain functional modelling (Bullmore and Sporns, 2012). This concept well fits with the brain functional organization proposed by different studies (**Figure 1**; Barbey 2018; Colon-Perez et al., 2016; Achard and Bullmore, 2007; Achard et al., 2006). Most of brain area relationships develop into local groups or clusters, and a minimum set of preferred paths connecting distant nodes at global level (i.e., long-range connections, involve physically or

functionally distant areas). These long-range connections tend to use a minimum number of nodes yet maintaining a high information-flow efficiency (Saba et al., 2019). Besides high global information transfer thanks to shortest paths length, and a low wiring cost for few longer connections, brain networks often display heavy-tailed degree distribution (power-law and truncated power-law; Mears and Pollard, 2016). This is the reason why small-world and scale-free distributions have been extensively used to describe topology and functional information flow in brain studies. Indeed, brain organization establishes a limited number of nodes with high degree (i.e., hubs), able to constitute highly connected subsets, forming what are known as rich clubs. Rich clubs represent the brain connectivity cores, and more general, hubs are the most important elements in information transfer because of their higher network centrality (Mears and Pollard, 2016). For the same reason, they also represent the major weak points of the brain network.

Since random attacks have a low probability to damage a relevant percentage of hubs, scale-free networks show a good resistance to random harm but are particularly exposed to targeted attacks (Mears and Pollard, 2016). In this regard, Achard et al., (2006) reported a truncated degree distribution of brain network with fewer large hubs, showing a higher resilience to targeted damage. Other studies, such as van den Heuvel et al., (2008), reported scale-free versus small-world network controversies, observed at different scales of functional connectivity. Most functional studies focussed on inter-regional connectivity, considering a brain parcellation with a fixed number of region (usually 90 regions), and reducing data resolution from point (voxel) resolution to regional resolution. As reported by van den Heuvel (2008), this approach could conceal a possible local scale-free organization of the human brain.

Although is hard associate brain topology to specific type of network models, other evidences are in favour of a complex organization that show intermediate small-world and scale-free networks characteristics. As introduced above, and described by many studies (Mears and Pollard, 2016; Fornito et al., 2015; Bullmore and Sporns, 2012; Knösche and Tittgemeyer, 2011; Achard 2006), modular organization is a powerful ground concept of brain topology, one of the first features observed in graphic studies of brain. Specific functions are performed within well-connected subsystems interconnected between them through an efficient and integrated global system (Mears and Pollard, 2016). Although this modular structure

(hierarchical in some cases) is not equivalent to the small-world model, brain networks show a naturally small-world properties, such as: (i) high density of relative short links between nodes located in close anatomical proximity to one other, and (ii) long-range connections with short average path length, allowing to connect modules with efficient global information-flow efficiency (Mears and Pollard, 2016).

As expected, many of these properties can be heavily impaired in brain diseases. Loss of small-world features, modules modifications and they hierarchical alterations, and hubs properties changes, are some the critical aspects (Mears and Pollard, 2016). Most pathological evidences regarded modifications in hubs centrality, shortest path architecture, and information exchange capacity (Mears and Pollard, 2016). However, recent literature showed hardly comparable and sometimes discordant scenarios, suggesting the necessity to develop coherent and robust models able to describe brain network alterations for different disorders with unambiguous results, associating complex anatomical and functional architectures to specific diseased phenotypes.

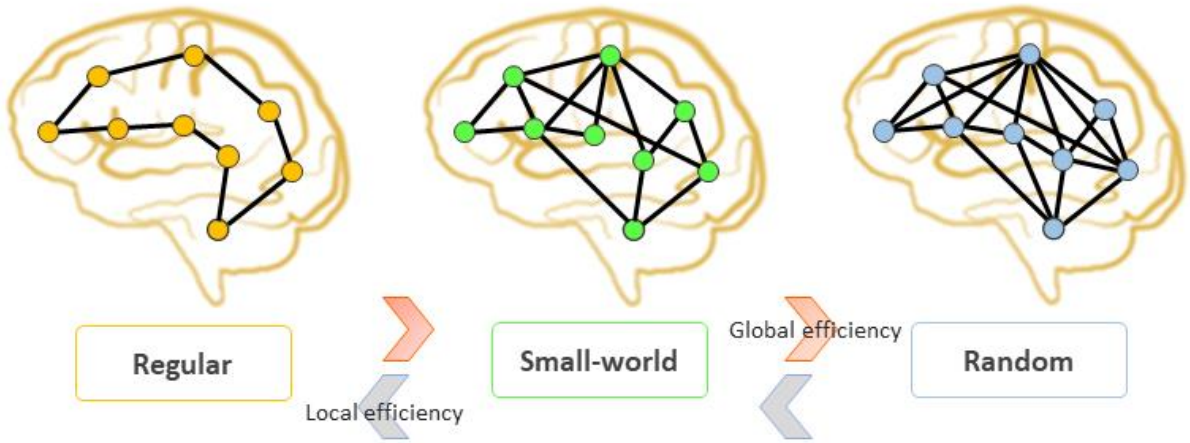

Figure 1. Brain small-world features.
Small-world network shows intermediate properties between random and regular graphs, ensuring an optimal equilibrium between global and local brain network efficiency. Adapted from Barbey 2018.

2. 3. Union of shortest path trees (USPT) and Minimum spanning tree (MST)

In modern neuroscience, human brain is considered as a complex system (Meier et al., 2015), for which network theory is increasingly becoming an essential modelling tool. As explained in the previous paragraph, some graph metrics have a higher descriptive power than others, at both functional and structural level. For instance, the functional brain architecture is the result of the need for an optimal integration among brain areas and the metabolic demand of their connectivity. Shortest path-based models are among the most effective tools in detecting critical structures optimizing the trade-off between functional integration and connection costs (Saba et al., 2019). Shortest paths between brain regions have been recently investigated also to understand the relationship between functional and structural brain networks, to highlight pathological network alterations that may be caused by the underlying neurodegenerative processes (Meier et al., 2015). At local level, shortest paths may reveal the presence of sub-structures essential for brain functioning. The impact of these local structures can be also measured in terms of global efficiency, proportional to the inverse of shortest paths, often strongly reduced in neuropathological disorders. Although shortest paths have been evaluated in terms of global connectivity (i.e., an average value of all shortest paths in a graph), a more informative approach considers all shortest paths as an underlying backbone topology for the functional brain network (Meier et al., 2015). As explained in detail in the next chapter, different studies suggest that the brain functional network adopts metabolic costs reduction when transporting information (Bullmore and Sporns, 2012). Therefore, a common practice to analyse complex functional networks is to reduce the initial (complete) network to its essential components (Meier et al., 2015). Recently, this was obtained exploiting shortest path-based algorithms. Focusing on shortest paths from the original graph aims to extract the essential *backbone*, or the main information *highways*, of the brain functional network (Meier et al., 2015; Tewarie et al., 2014).

A variety of complex network studies has been recently applied the union of shortest path trees (USPT), a sampling method used for functional brain network analysis (Meier et al., 2015). To build a USPT, is necessary identify the shortest path tree (SPT) associated at each node of the graph. A shortest path tree of a node A consists in all shortest paths from A to all other nodes (Meier et al., 2015). Considering the original network G, composed by N nodes and E links, we can obtain the USPT of G by combining all its shortest path trees. The USPT is

influenced by the topology and weights of the underlying graph G. Obviously, with constant edge weights, the resulting USPT will be entirely determined by the underlying network topology (Meier et al., 2015). Let us consider edge links in G as $l = i \rightarrow j$ (i.e., directed connection from i to j), and their associated weights $w_l = w_{ij} = w(i \rightarrow j)$. A path from two nodes A and B can be denoted by $P_{A \rightarrow B} = n_1 n_2 \dots n_{k-1} n_k$, with length equal to k∈N, where $n_1 = A$ and $n_k = B$, with $n_1 n_2 \dots n_{k-1}$ being the intermediate nodes along the path (Meier et al., 2015). The weight path $P_{A \rightarrow B}$ can be calculated as: $w(P_{A \rightarrow B}) = \sum_{l \epsilon P_{A \rightarrow B}} w_l$. Therefore, the shortest path $(P^*_{A \rightarrow B})$ between A and B will be the path minimizing the weight $w(P_{A \rightarrow B})$ over all possible paths in $A \rightarrow B$, expressed as: $w(P^*_{A \rightarrow B}) \leq w(P_{A \rightarrow B})$ (Meier et al., 2015). In most cases, link weights are real positive numbers, hence the shortest path is unique. Since SPTs catch the most relevant routes in terms of network efficiency, USPTs can be used as a framework for evaluating network connectivity performances, including key information flow routes. Furthermore, when describing diseased versus healthy subjects, USPT-based models can efficiently extract critical node interactions, determining the observed case-control differences and removing the background noise from full connections (Meier et al., 2015). Commonly, studies of real-world networks are based on cost optimization algorithms, often based shortest paths, revealing critical information flow paths in complex systems, including functional brain connection routes. Therefore, SPTs are powerful tools to detect information flow routes with high probability of being involved in complex diseases onset and progression (Meier et al., 2015).

An interesting feature of USPTs is that they always include a *minimum spanning tree* (MST; Meier et al., 2015). An MST is an extremely efficient binary representation of the original graph, characterized by N nodes and (N - 1) edges. It assembles connections minimizing the sum of edge weights, and excluding edges forming cycles (Stam et al., 2014). An MST has the minimum total edge weight of all possible spanning trees of the original graph. The regime in which USPT and MST coincide is called *strong disorder*, implying that the information travels entirely along MST links (Meier et al., 2015; Tewarie, et al., 2014; Van Mieghem and Magdalena, 2005; Van Mieghem and van Langen, 2005). Recently, MSTs have been successfully applied to functional data of patients affected by different brain disorders to demonstrate functional disruptions respect healthy controls (Saba et al., 2019; van Lutterveld et al., 2017; Fraga González et al., 2016; Stam et al., 2014; Tewarie et al., 2014). Given MSTs

efficiency and high sensitivity to small fluctuations of connection weights (Van Mieghem and Magdalena, 2005), they can intrinsically provide an accurate representation of subtle and critical topological perturbations at local scale. On the other hand, MST sparseness could raise some issues at global scale. However, it has been demonstrated that if the MST weight distribution is consistent with a power law with sufficiently small exponent value, the global information flow of the underlying network is entirely sustained by MST paths (Meier, et al., 2015; Van Mieghem and Magdalena, 2005; Van Mieghem and van Langen, 2005). The MST method handles very different network configurations, with extremes represented by linear and star shapes. In the former, each node has a maximum of two edges (i.e., path-like tree) and two extreme leaves (i.e., nodes with only one link). Whereas, in a star, all nodes are leaves, except the central node to which the others are connected (Stam, et al., 2014). Every network can be described through a set of characteristic graph metrics reflecting its specific configuration and weights. MST measures provide information about graph centrality (maximum degree k_{max}, maximum betweenness $B_{\max}$), distance (diameter *d*, eccentricity *Ecc*), association (assortativity *Ass*), and topological properties (degree divergence *K,* leaf fraction *Lf*, tree hierarchy T_h). These definitions are given in **Table 2**. Short distances and overload prevention properties suggest a good tree configuration or network integration. If a tree has a star-like (i.e. highly connected) topology, it will be characterized by a greater information exchange capacity (i.e., spread of information across the tree), yet a greater probability of central node overload. The opposite behaviour is true if the graph has a line-like topology van (Lutterveld, et al., 2017; Stam, et al., 2014).

Table 2. Description of MST global measures. Definitions by Yu et al., (2016) and Stam et al., (2014). Published in Saba et al., 2019.

Measure	**Definition**
k_{max}	*Degree (k)* of a node is the number of links connecting one node to another in the network, and *maximum degree* k_{max} indicates the highest value of node degree in the network
B_{max}	*Betweenness centrality* (*B)* of a node indicates the number of shortest paths passing through the normalized node such that $B \in$ [0,1], and *maximum betweenness* B_{max} indicates the highest value of betweenness centrality in the network
d	*Diameter (d)* identifies the longest distance, measured in number of edges, between any two nodes; *d* has a range from 2 to N-1
Ecc	*Eccentricity (Ecc)* of a node indicates the distance of a node with respect to any other node, in term of longest distance between them. Here, Ecc represents the average value (i.e., the arithmetic mean) for all nodes
Ass	*Assortativity (Ass)* describes node tendency to link to other nodes, characterized by the same or similar degree, which can be quantified by computing the Pearson correlation coefficient of the degrees of pairs of nodes connected by an edge
K	*Degree divergence (K)* is a measure of broadness of the degree distribution in the whole network, defined as the ratio between the variability and the average of node connections. It is expressed as: $\langle k$^2 $\rangle$ / $\langle k \rangle$
Lf	*Leaf fraction (Lf)* is the ratio between the number of nodes with only one edge (i.e., "end-points" in the graph) and the maximum possible number of edges (i.e., the number of nodes minus 1, N-1). Stars-type graph is defined by *Lf* = (N-1)/(N-1) = 1, while linear-type graph by *Lf* = 2/(N-1)
T_h	*Tree hierarchy* (T_h) is a measure of type configuration characterized by a combination of short distances and prevention of overload of any node. For a path it is equal to 2/m, while approaches 0.5 for a star, and can assumes values between 2/m and 1 for trees with intermediate configurations. It is expressed as: $Lf \ / \ ((2m * B\_max))$

N = number of nodes in an MST; m = number of edges in a MST

3. Brain networks: from anatomy to topology

Human brain is covered by a tiny layer of less than 3 mm called grey matter, that constitutes the cortex. Anatomically separated regions of cortical grey matter are strongly connected each other by axonal projections and to subcortical grey matter nuclei. All axonal projections form a white portion, called white matter, which mostly connect the two cerebral hemispheres (Papo et al., 2014). Globally, brain organization is characterized by large-scale networks of grey matter regions connected by white matter tracts, with complex patterns of synaptic connections between locally neighbouring neurons belonging to the same cortical area, showing qualitatively complex organization at both micro and macro scales. Therefore, an exhaustive network connectivity map would be a task of unmanageable technical difficulty (Papo et al., 2014).

Given such a complexity, the first simulation of a biological neural network was introduced only in 1950's (Papik et al., 1998), when brain behaviour mechanisms and its neurosensory organization was used as a possible successful model to explain many psychiatric phenomena. Only one year after, the first artificial neuron definition was published (Papik et al., 1998). Further progresses in computer technology allowed to develop more sophisticated neural functions, respect to the first relatively simple model. In 1980s, mathematical neural models became relevant to practical applications, including medical use. This led to the development of four main fields in these studies: modelling, bioelectric signal processing, diagnostics, and prognostics (Papik et al., 1998).

Beside modelling of brain functions and neurosensory organs, bioelectric signal filtering evaluation and development of artificial intelligences over biological systems responses, developments of brain network models brought to interesting responses in classification and prediction of clinical phenotypes (Papik et al., 1998). As introduced in the previous chapter, network modelling may greatly improve the interpretation of physical and instrumental findings, enabling a higher diagnostic accuracy and, through the identification of phenotype-specific features, it can discriminate different subtypes of same disease as well as different disorders showing similar phenotypes. In addition, retrospective network-based parameter analysis can be applied to obtain prognostic information (Papik et al., 1998), focusing on onset disease prediction and its development.

Further advancement of these applications is also due to the development of neuroimaging techniques (Papo et al., 2014). Neuroimaging allows the inspection of large-scale network organization of the brain, at macroscopic scale, in a direct and non-invasive way. Some neuroimaging techniques have enough spatial resolution to measure structural features and functional properties, such as cortical thickness and low-frequency endogenous oscillations, in hundreds of cortical areas and in major subcortical nuclei. Anatomical or functional connectivity measures can be extracted from these data (Papo et al., 2014).

Firstly, graph theoretical studies suggested a new perspective on how we can observe brain, introducing the fundamental concept of topology system, until now inferred from the anatomical architecture (Papo et al., 2014). Brain network topology is represented as a set of connected brain regions (nodes), either custom- or atlas-defined. Node connections are not necessarily quantifiable in terms of physical units; hence a graph representation typically contains non-metric abstract relationships (Papo et al., 2014). Independence from underlying data offers a several of advantages, including: (i) quantification of topological features with the same mathematical language at macro and micro scale; (ii) creation of a connection between functional and anatomical network organization; (iii) comparison of different brain topologies across species; (iv) construction of brain network models that are comparable with other biological and non-biological systems (Papo et al., 2014).

As introduced in the previous section, topological characteristics of brain networks include different aspects coming from complex network models. Combination of high clustering and low shortest path length between nodes, confers it a high global efficiency (Papo et al., 2014). Functional modular decomposition highlights a repartition tendency at different levels. Community structure can be described by modular grouping, in which each module comprises a group of highly connected nodes that are relatively isolated from nodes belonging to other modules. In many complex biological systems, including brain, a modular organization often implies the existence of nested sub-modules or, in other terms, a hierarchical structure, where inter-modular links are mediated by connector hubs with a high betweenness. (Papo et al., 2014). Likewise, brain topology partition in rich clubs (see paragraph 2.2) identifies small cores of nodes with high degree (i.e., highly linked to each other), but with poorly connected peripheral nodes. So, rich club hubs represent the connectors among brain modules, playing a high integration role through minimum path length motifs management (Papo et al., 2014).

Starting from this non-trivial organization, an important question concerns the relationships among brain network topology, its anatomical architecture, and its information-processing capacity. Several studies (Papo et al., 2014; Bullmore and Sporns, 2012; Laughlin and Sejnowski, 2003) focused on how a high complex functional organization may come with a so limited physical space, following the principle of wiring and metabolic costs minimization. Spatial co-location of nodes in the same modules may strongly reduce information flow-costs thanks to functional proximity of these elements, that are often also anatomically proximal. Less clear are the inter-connections of hubs in rich clubs that are anatomically separated, improving network integration, but increasing minimizations costs (Papo et al., 2014). Although human brain functional networks are still largely unsolved, brain anatomical and functional complexity could be the result of continuous adaptive trade-offs, in response to the need for balance among wiring efficiency, costs optimization, and system resilience.

Many computational and information-processing brain abilities are performed by dynamically coupled or synchronized neuronal populations. Neuronal activities fluctuations, induced by synchronization of different groups of them in relations to spontaneous or specific task, may result in transient functional networks. This dynamic feature modulates cortical interactions, increasing the general brain areas relations power, delivering a common idea of its involvement in cognitive functions. Improving functional topology, from a single neuronal scale to a group of nodes (and their interactions), increases system complexity, requiring spatial fragmentation to sample the underlying dynamic system. This implies a system anatomical subdivision in different parts, and each of them can be reduced to structureless points or nodes (Papo et al., 2014).

Brain functional connectivity, usually defined as a statistical relationship between signals activity of brain regions (i.e., nodes), is often interpreted as a result of the underlying anatomical architecture, validated on functional connectivity metrics (Bullmore and Sporns, 2012). Currently, functional techniques to infer economic trade-off organization about brain connectivity enabled a deeper understanding of the processes underlying complex brain disorders, even if were not universally defined best parameters to interpret cerebral activity, and how these can influence topological properties of the resulting networks.

3. 1. Wiring and metabolic brain network costs

Brain organization is one of the most expensive body systems in terms of build costs and activities maintenance, however many brain processes regulate these wiring and metabolic costs (Bullmore and Sporns, 2012). On the other hand, costs minimization is not the only driving force of this organization. Complex adaptative brain network behaviours, such as information processing and robustness to perturbations, play a leading role. Moreover, according to a simple economy principle, high global efficiency of information-flow between spatially distant neurons (or brain areas) could not be possible (Bullmore and Sporns, 2012).

Brain connections probability distribution is dominated by efficient shortest paths, with fewer possible long-distance connections (Betzel and Bassett, 2018; Bullmore and Sporns, 2012). In both micro-and macro scales, a connection probability depending to spatial distances has been observed. At cellular level, there is a higher synaptic connection probability between cells spatially closed, as well as, at regional level, shortest distance between brain areas may predict a greater axonal projection (Bullmore and Sporns, 2012). Nevertheless, functional or topological advantages might compete with this evidence. Topologically neighbouring neurons, directly connected by single synapse, are more functionally advantageous respect polysynaptic links between nodes at the same spatial distance, but topologically located far away. Hence, there is a functional advantage to direct or monosynaptic link between nodes located far apart in space, also if it is energetically expensive (Bullmore and Sporns, 2012). It has been demonstrated that graph models representing neuronal morphology that consider a competition between wiring costs and path length minimization, bring to more realistic reproductions of different type of neurons. As already introduced, in addition to wiring costs, much of brain expenses are due to metabolic or energetic demand of biochemical neuronal maintenance for transmission of electrical signals. These costs are minimized by myelination but increased by greater axon length and diameter (Bullmore and Sporns, 2012).

Typical modular small-world characteristics attributed to brain networks, such as high network clustering and efficiency, are much more attractive in terms of both segregated and integrated information processing (Bullmore and Sporns, 2012; Knösche and Tittgemeyer, 2011). Segregation or modularity results in a functional specialization of brain areas, showing a higher clustering and connectivity with areas with the same functional role (Bullmore and Sporns, 2012). At the same time, these modules show an optimal global efficiency of inter-

modular connections thanks to a high functional integration level (Knösche and Tittgemeyer, 2011). Often, in large-scale brain networks, areas involved in the same topological module are also anatomically neighbours. This configuration offers the maximum benefit for wiring and metabolic costs, favouring segregated processing and rapid dynamical reconfigurations (Bullmore and Sporns, 2012). Hubs integration involves long-distance connections that are energetically expensive but reducing information flow routes length and bringing a faster, more direct, and less noisy information transfer. This trade-off between minimization costs and maximization of functional efficiency contributes to the observable brain integration. In response to external stimuli, brain topological adaptative capability can reconfigure functional organization in a successful and rapid way. Some researcher studied this phenomenon through functional connectivity analysis based on dynamical modelling (e.g., in response to changing experimental task demands, progressive learning of a task). When cognitive demand is high, the network adopts a more efficient but more expensive configuration (i.e., using long-distance connections). Differently, when the cognitive demand is lower, brain functional network relaxes into a lesser costly configuration, with higher clustering and higher modularity (i.e., minimum percentage of long connections; Bullmore and Sporns, 2012).

To this scenario, Betzel and Bassett (2018) added a further idea of long-distance connections role, considering them not only as merely topological shortcuts, introducing the hypothesis that long-distance connections are used by the brain as canals for unique input and as a novel target for area's outputs, favouring novel or complex task development through interaction enhancing of areas functionally different (Betzel and Bassett, 2018). Spatial location and weight of incoming and outgoing connections between brain areas model their functional properties, so that the larger the variability of connection lengths distribution of a brain area, the greater its functional importance within the network. Moreover, long-distance connections architecture of brain networks showed non-random correlations, translating in high similar patterns of incoming and outgoing connections. This feature has been interpreted as a greater brain network robustness: even if some links is lost, others similar links can be ensuring the functional performance. Novel interpretations on brain functional architecture, and on role of its components, have been introduced in the last years. We may consider long-distance connections not only as a cause of efficiency and path length changes, but also like a

fundamental way for novel task development, providing specificity and robust bridges between spatially neighbourhoods and brain areas (Betzel and Bassett, 2018).

3. 2. Large-Scale functional networks

Brain activity can be recorded through different noninvasively neural techniques over several times series. In this work, we focused on resting-state condition, known as spontaneous activity during quiet waking, obtained using functional magnetic resonance imaging (fMRI). Through imaging techniques is possible obtain functional networks, from which most classical neuroimaging studies aimed to identify brain regions differentially activated during specific cognitive tasks (Sporns, 2011). Recent studies go beyond the idea of a "selective" regional activation in order to a task, showing that cognitive neural correlations are not limited to the appearance of task-related activations. Beside specific activation of circumscribed brain regions, cognitive tasks have been associated to activity pattern modification in control conditions, i.e., when the brain is in resting state (Sporns, 2011). Some specific areas, including praecuneus/posterior cingulate cortex, medial frontal cortex, and lateral parietal cortex, formed this decreasing activation pattern bringing at the formulation of unknow coherent system, but recognizable during resting state. This system was called *default mode*, as a physiological baseline involving organized areas interrupted when attention-demanding goal-direct cognitive tasks are required (Sporns, 2011). Many studies contributed to improve these evidences, showing that brain areas commonly deactivated in the default mode system during goal-direct cognitive task, were interconnected and dynamically correlated, forming therefore a functional network (i.e., default mode network, DMN). Moreover, this functional network can be observed during a sensory task with low cognitive demand, but it is deactivated in working memory task (Sporns, 2011). In line with previous evidences, DMN showed anticorrelations with brain regions involved in high cognitive demand, such as prefrontal cortex. Instead, praecuneus/posterior cingulate cortex seems constituting a key area in this network since its functional connections covered entirely the mentioned pattern and showed a strong inverse correlation with activity-related brain regions. In general, functional connectivity within DMN appeared trustable and reproducible, in which its topology was supported to underlying long-range structural connections between brain regions (Sporns,

2011). Thanks to different methods (e.g. independent component analysis, ICA) of functionally linked brain regions identification, the DMN is not the only functional pattern recognizable by resting state from spontaneous brain activity. In fact, some studies revealed five or six functional modules partially overlapping, including among the most cited central, occipital and default mode modules (Mears and Pollard., 2016; Sporns, 2011; Salvador et al., 2005). A common characteristic of these resting state networks is a set of interconnected brain regions that interact in specific cognitive fields, such as episodic memory, visual and motor planning (Hohenfeld et al., 2018; Mears and Pollard, 2016; Trojsi et al., 2015; Sporns, 2011; Chavez et al., 2010). In addition, coherence in brain activity across spatially distributed brain regions, have been reported by some studies through analysis of low frequency fluctuations of blood oxygen-level dependent (BOLD) during resting-state experiment, classifying these modules as *intrinsic connectivity networks* (ICN; Barbey, 2018; Park and Friston, 2013; He et al., 2009). Some representative ICNs are default mode network, dorsal attention network, executive control network, salience network, sensorimotor, visual, and auditory systems (**Figure 2**; Park and Friston, 2013; Raichle 2015; He et al., 2009).

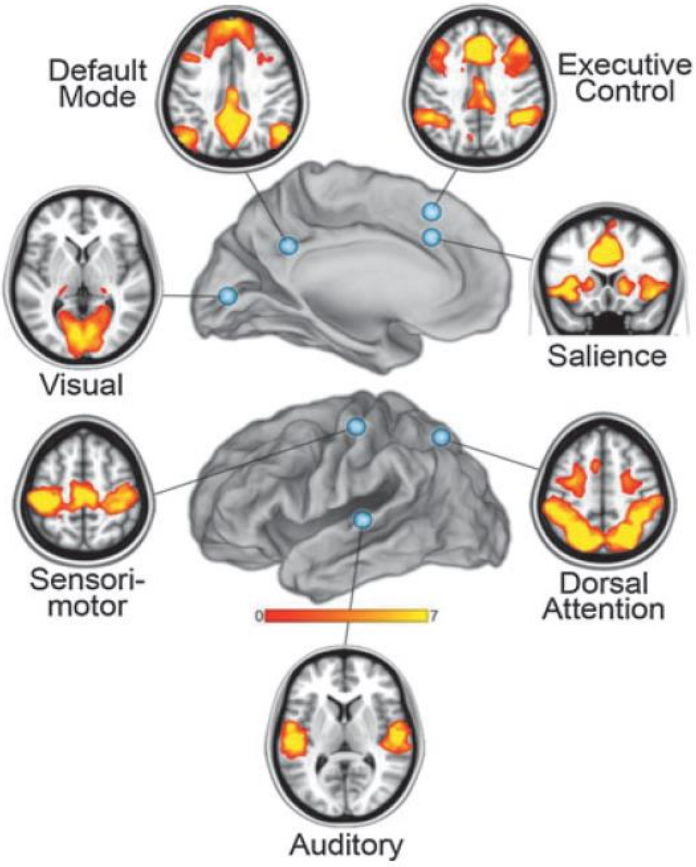

Figure 2. Anatomical localization of brain functional areas of intrinsic connectivity networks. Activated functional areas are highleted by red-to-yellow colour range, indicating the lower and the higher fuctional activity level, respectively. Figure by Raichle 2011.

The characteristics of brain topology described in the previous sections, such as modularity and its hierarchical community structure, find an application also in the context of functional networks organization (Barbey, 2018; Park and Friston, 2013). Hubs play key different roles in the connectivity infrastructure, serving as “provincial hub” when they reinforce intra-module connections or as “connector hubs”, when provide a link between modules (Barbey, 2018). Therefore, they play a fundamental role for a high information exchange capacity both within and between ICNs, translatable in mutual interactions between cognitive processes. It has been estimated that almost 70% of the total shortest paths are mediated by a rich club of strongly connected hubs (Barbey, 2018). Recent studies added an interesting functional interpretation to this scenario, where hubs role emerged in network transition capacity in many easy-to-reach states, using highly accessible representations of prior knowledge and experience referred to as crystallized intelligence. Brain network topology is modelled on the base on new knowledge and prior experiences, from which is possible observe different changes as new neurons, synapses, and connections, promoting the accessibility of crystallized intelligence. Several ICNs (mostly the DMN) show these latter characteristics, supporting semantic and episodic memory representations (central to crystallized intelligence), and providing a baseline resting state from which these representations can be readily accessed. Although hubs provide access to easy-to-reach states, other abilities seem to be supported by weak connections enabling a higher flexibility of information processing and promoting a higher-order brain network structure (Barbey, 2018). Some studies identify these connections as difficult-to-reach states, favouring more complex adaptation processes, supported by flexibility and intelligence behaviour. Starting from new experiences, difficult-to-reach states are based on the fluidity of the adaptation process, through the selection and assembly of new representations with high cognitive demands. As in the case of crystallized intelligence, different ICNs have these characteristics, regarding mostly the frontoparietal and cingulo-opercular networks, both supporting cognitive control. Specifically, frontoparietal network carry out the top-down regulation and the control of mental operations that, in response to environmental change and adaptive task goals, are maintained by the cingulo-opercular network (Barbey, 2018).

Brain small world topology relies on the base of these transition phenomena. According to neuroscience network theory, ICNs show small-world topology as a critical state close to a

phase transition between a regular and random network (Barbey, 2018). Specific cognitive abilities are associated to the transition towards regular networks, while broad or general abilities rely on functional topologies tending to more random configurations. Frequently, ICNs do not show uniform topologies, exhibiting different degrees of variability in line with an architecture that supports dynamic functional connectivity profiles. A lower within-modules variability ensures specific mental capacity, while a higher inter-modular variability provides a more flexible, small-world topology of broad mental abilities. This functional organization promotes a strong flexibility of INCs, allowing to switch between easy- and difficult-to-reach states with greatest dynamic plasticity, mostly exhibited by networks that are strongly associated with fluid intelligence, such as the frontoparietal network (Barbey, 2018).

Concerning cognitive control research, three ICNs have been mostly investigated: the default mode network (DMN), the salience network (SN) and the central executive network (CEN; Barbey et al., 2015). **Table 3** and **Figure 3** show brain regions involved in these INCs, with their characteristic areas. As already mentioned above, the DMN is specialized in internal focus of attention during self-referential cognitive activity, autobiographical memory, and social cognition, while the CEN supports external focus of attention during goal-directed, cognitively demanding tasks (**Figure 3**; Barbey et al., 2015). In other terms, internally oriented tasks selectively activate the DMN, whereas externally oriented tasks preferentially engage the CEN. This opposite activities of these two networks are mediated by the SN, employed in direct attention to behaviourally salient events in the internal and/or external environment (**Figure 3**). In fact, the SN provides a balance between DMN and CEN recruitment, supporting the interactions between processing of internally versus externally oriented tasks (Barbey et al., 2015).

Barbey et al. (2015) reported the concept of feedback control used by associated areas in cognitive control system to regulate different processes in a variety of brain systems. They described how computational models indicate two primary steps to implement cognitive control: (i) “goal setting” process, consisting in a selection of goals through reward prediction by the basal ganglia; and (ii) “goal searching”, a process that individuates actions that could be feasible to obtain the goal, selecting them by matching the current state with the maintained goal state. Complex behaviour, such as adaptation and coordination, is favourited

by this mechanism, allowing the maintenance of homeostatic balance across ICNs (Barbey et al., 2015).

Table 3. Brain regions involved in the three functional networks. Taken from Barbey et al., (2015).

ICN	ICN-associated brain regions
Default mode network	ventromedial prefrontal cortex, posterior cingulate cortex, angular gyrus and medial temporal lobe
Salience network	anterior insula and dorsal anterior cingulate cortex
Central executive network	mainly includes dorsolateral prefrontal cortex and posterior parietal cortex

ICN = intrinsic connectivity network

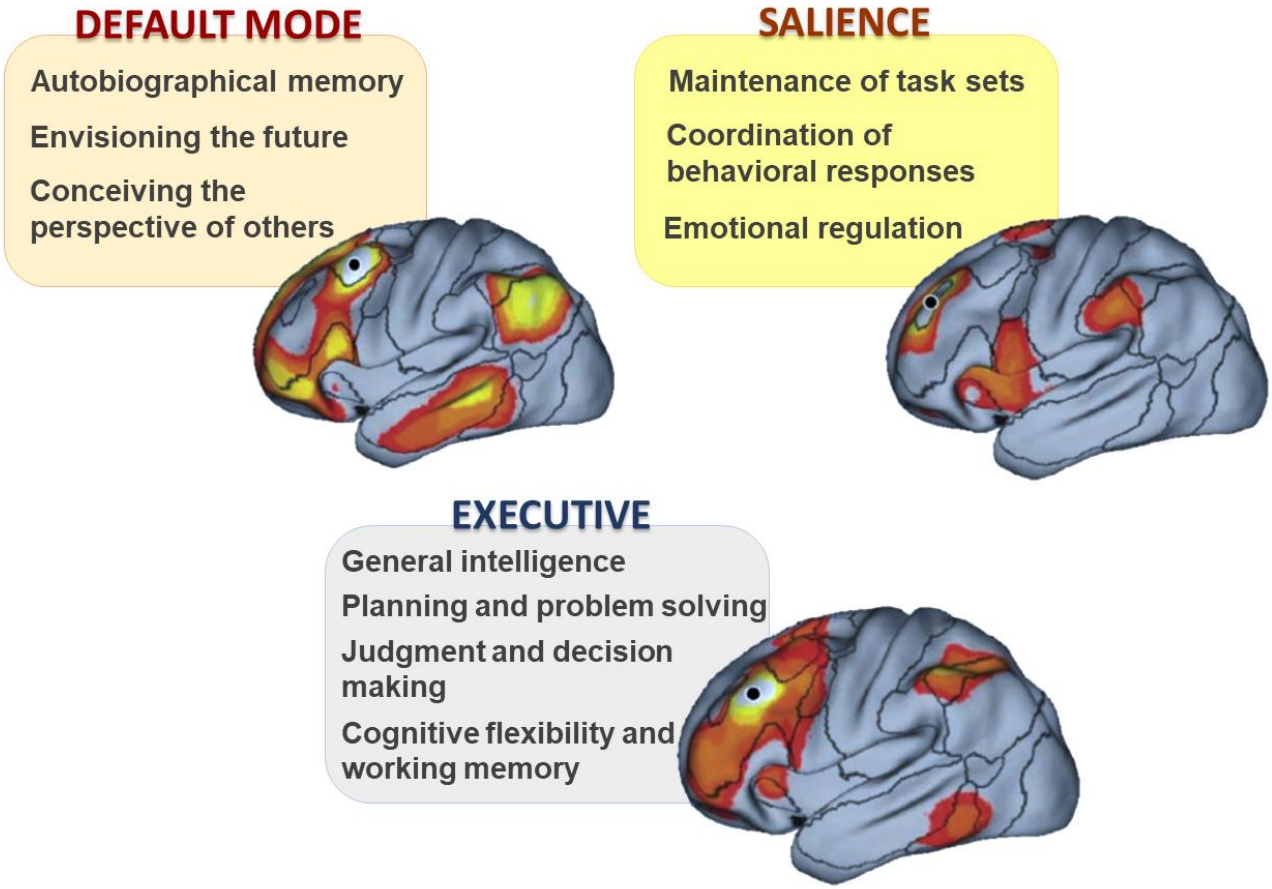

Figure 3. Functional brain areas activity in sagittal section of the three mostly investigated intrinsic connectivity networks with main cognitive features. Modified from Barbey et al., 2015.

4. Frontotemporal Dementia

General population aging in modern society places us in front of a near future with millions of dementia patients, bringing ever more complex and unmanageable social and economic questions (Haass and Neumann, 2016). Frontotemporal Dementia (FTD) is a neurodegenerative disorder, known as the common cause of young onset dementia (Liu et al., 2019; Young et al., 2018; Olney et al., 2017; Haass and Neumann, 2016; Woollacott and Rohrer, 2016). FTD includes clinically and pathologically different groups of disorders, characterized by changes in behaviour, social conduct, executive functioning, language or speech due to brain atrophy generally localized in the frontal and/or the temporal lobes (Liu et al., 2019; Young et al., 2018; Olney et al., 2017; Woollacott and Rohrer, 2016).

4. 1. Brief history and epidemiology

"Progressive deterioration of language associated with left temporal lobe atrophy" was the first know description of a patient with Frontotemporal Dementia (FTD) provided by Pick in 1892 (Liu et al., 2019; Olney et al., 2017). In the following 34 years, were descripted some fundamental knowledges about neurodegenerative features of these pathology. Alois Alzheimer in 1911 examined in-depth Pick's clinical cases, showing the presence of silver staining argyrophilic cytoplasmic inclusions within neurons thanks to histologic analysis (Liu et al., 2019; Olney et al., 2017). Subsequent studies brought firstly to the identification of "Pick's atrophy" to distinguish patients with atrophy in the frontal and temporal lobes, and secondly were delineated Pick's bodies from Pick's cells from which they defined "Pick's disease" as a neuropathological entity (Olney et al., 2017). Until 1970s, anatomical, clinical and pathological principles discovered by previous researchers were shelved, characterizing this period for a dearth of research into Dementia. In this scenario, only few researcher groups continued these studies through clinical description accompanied by neuroanatomical and pathological analysis, even if their work will be appreciated only decades afterwards (Olney et al., 2017). Delay, Brion and Escourolle defined clinical and neuropathological differences between Alzheimer disease and Pick's disease. Pick's disease was described as a localized atrophy in frontotemporal lobes, and sparing of the posterior lobes, with ballooned cells and cortical-sub-cortical gliosis at histological level, characterized by increased behavioural alterations,

lack of insight, and a very low influence from apraxia and agnosia. Instead, Alzheimer disease showed a more general cerebral atrophy, characterized histologically by neurofibrillary tangles and senile plaques, with clinical symptoms such as agnosia, apraxia, and spatial orientation problems (Olney et al., 2017). Few years after 1970s, Constantinidis created the first subdivision of pick's disease into three subtypes and only one of these groups showed classical pick's bodies, from which pick's bodies were not fundamental for Pick's disease diagnosis (Olney et al., 2017). In addition, the same decade saw an important improvement in diagnostic criteria: arteriosclerotic dementia left the role of underlying pathology for senility (acquired between 1950s and 1960s), and the concept of dementia was associated to those of Alzheimer's neuropathology. Indeed, this belief brought to the idea that the dementia was so rare and impossible to distinguish from Alzheimer's disease (Olney et al., 2017). So, Alzheimer's disease (AD) became the most studied neuropathology in the USA, but some researcher groups in Europe focused on large cohorts of people with non-Alzheimer's dementia. From 1990s to beginning of 2000, there were important progress about Dementia features, also thanks to use of different diagnostic instruments such as neuroimaging and neuropsychiatric testing (Olney et al., 2017). In particular, in the 1980s, Mesulam coined the term *primary progressive aphasia* (PPA; i.e., a specific subtype of FTD), while Snowden defined the term of *semantic dementia* to indicate patient originally described by Pick with predominant left temporal atrophy and aphasia (Olney et al., 2017). At the beginning of 1990s, the first research criteria for FTD was invented (as "Clinical and neuropathological criteria for frontotemporal dementia"; The Lund and Manchester Groups, 1994), which was revised late in the same decade, when the FTD spectrum was divided in three categories: *behavioural variant*, *nonfluent aphasia variant* and *semantic dementia variant* (Olney et al., 2017); demonstrating both to distinguish FTD from AD also during life and a better characterization of patients in specific FTD subtypes (Olney et al., 2017).

While some decades ago dementia was considered a very rare pathology, today FTD is the second most common presenile dementia in subjects under age 65 (Young et al., 2018; Olney et al., 2017; Woollacott and Rohrer, 2016). Although its frequency is less respect to AD, the incidence of this neuropathology is between 1.61 and 4.1 cases per 100000 people annually, with a prevalence of 10.8 per 100000 (together with PSP and CBD, related FTD disorders), with age onset peaks between 65 and 69 years (Olney et al., 2017). Although the average age of

onset is estimated between 45 and 65 years, very early onset has been recorded under the age of 30, as well as in aging subjects. Until now, no prevalence differences between men and women have been documented. Concerning FTD subtypes, behavioural variant Frontotemporal Dementia (bvFTD) involve about 60% of cases (Olney et al., 2017). A possible underestimation of cases affects this percentage, mainly due to low disease frequency in a relative large at-risk population, and secondly to the lack of FTD recognition and its overlap with several other neurological disorders, including ALS (Young et al., 2018; Olney et al., 2017; Woollacott and Rohrer, 2016). This influences the general estimates for world-wide population, because epidemiology results strongly depend on collected subjects (Young et al., 2018).

4. 2. FTD-phenotypes clinical classification

FTD is a generic term involving three recognizable clinical syndromes: *behavioural variant Frontotemporal Dementia* (bvFTD), *semantic-variant Primary Progressive Aphasia* (svPPA), and *non-fluent-variant Primary Progressive Aphasia* (nfvPPA; Liu et al., 2019; Mann and Snowden, 2017; Olney et al., 2017; Haass and Neumann, 2016; Woollacott and Rohrer, 2016). In addition, FTD often overlap other neurodegenerative disorders associated to motor deficits, called *corticobasal degeneration* (CBD), *progressive supranuclear palsy* (PSP), and *amyotrophic lateral sclerosis* (ALS; Liu et al., 2019). Each FTD-phenotype is characterized by cognitive and behavioural markers, sometimes overlapping among them (Liu et al., 2019).

The bvFTD subtype is the most conceptually separable phenotype and, as the name suggests, it shows different altered behaviours, such as progressive personality and behavioural instability, apathy, and disinhibition in interpersonal interactions (Liu et al., 2019). Other early changes can be alterations in food preference and eating behaviour, alterations in empathy, and dysexecutive symptoms. It has been observed that bvFTD patients may show typical symptoms of a psychiatric disorder, such as depression, schizophrenia, and bipolar disorder, making hard to discriminate a characteristic FTD behaviour from psychosis (Liu et al., 2019).

Other phenotypes are included in PPA group, which intuitively include alterations related to a progressive decline in linguistic ability, mostly during the early stage of the disease (Liu et al.,

2019). Specifically, this symptomatology is more pronounced into the first two years from the onset, in which deficits in object naming, syntax, or word comprehension can be observed. In theory, three PPA subtypes can be identified, including semantic, non-fluent and logopenic variants, even if the logopenic variant is not classified as FTD, but usually associated to Alzheimer's disease (Liu et al., 2019). For this reason, only semantic (svPPA) and non-fluent (nfvPPA) variants will be considered in this chapter. The svPPA and nfvPPA are generally characterized by distinct pattern of language deficits. In svPPA, anomia and single word comprehension deficits are evident, while fluent speech and correct grammar issues characterize the initial phase of the disease (Liu et al., 2019). In this case, semantic memory is damaged due to the anterior temporal lobe degeneration. Conversely, patients with nfvPPA show articulation deficits expressed by slow, laboured, and halting speech production, in addition to incorrect grammar or syntax. As in the case of svPPA, some opposite skills remain almost intact, including semantic knowledge for words (Liu et al., 2019).

In addition to standard phenotypes, there are motor syndromes associated to FTD-spectrum, including motor neuron disease (FTD-MND), and two variants with parkinsonism, called corticolbasal syndrome (CBS) and progressive supranuclear palsy syndrome (PSP-S; Liu et al., 2019). These motor syndromes can be found in association with FTD variants: up to 15% of patients with FTD are affected also by MND, while about the 30% of FTDs have mild MND features (Liu et al., 2019). Moreover, FTD patients may show features of CBS or PSP. In the MND case, people affected may show both upper motor neuron signs, including hyperreflexia, extensor planar response, and lower motor neuron signs characterized by weakness, muscle atrophy, and fasciculation (Liu et al., 2019). Others MND symptomatology are dysarthria, dysphagia and pseudobulbar affect. Concerning CBS, different aspects are involved in this pathology, considered as a heterogeneous syndrome, including behavioural, cognitive and motor changes (Liu et al., 2019). Lastly, PSP presents instead atypical parkinsonism features, such as axial and symmetrical rigidity, decreased saccadic velocity, and early postural instability with falls (Liu et al., 2019).

4. 3. Biological FTD biomarkers

As introduced above, FTD is associate to a pathological process of frontal and temporal brain lobes degeneration. At histological level, there are three main conditions characterized by abnormal neuronal, and sometimes glial, accumulation of aggregated proteins (Liu et al., 2019; Mann and Snowden, 2017; Woollacott and Rohrer, 2016). About 90% of patients show abnormal intracellular aggregates of tau and TDP-43 (RNA- DNA-binding protein), subdivided in about 45% of FTDL-tau and about 50% of FTLD-TDP (Liu et al., 2019; Mann and Snowden, 2017). The remaining part, about 5% of cases, shows mostly abnormal intracellular fused in sarcoma inclusion (FUS), termed FTDL-FUS (Liu et al., 2019; Mann and Snowden, 2017).

Nowadays, the only certain FTD risk factors are mutation in specific genes, so that the most cases derived from unknow causes, also called *sporadic* cases (Woollacott and Rohrer, 2016). On the other hand, is been demonstrated that between 30 and 50% involve patients with a positive FTD-family history, while only 10-15% of cases have a clear autosomal dominant inheritance pattern. Most of familial cases are associated to mutations in one of three main genes: MAPT (microtubule-associated protein tau), GRN (progranulin), and C9orf72 (chromosome 9 open reading frame 72) (Liu et al., 2019; Mann and Snowden, 2017; Woollacott and Rohrer, 2016). Over the past few years, another mutation has been associated to familial case of FTD: TBK1 (TANK binding-kinase 1). Other rare genetic causes involve VCP (vasolin containing protein), CHMP2B (charged multi-vascular body protein 2B), SQSTM1 (p62/sequestome1), TARDBP (transactive response DNA-binding ptotein-43), UBQLN2 (ubiquilin 2), and OPTN (optineurin) (Liu et al., 2019; Woollacott and Rohrer, 2016).

Among FTD phenotypes, bvFTD show a higher heritability respect to PPA, where nfvPPA has a more probable familiar origin than svPPA (Woollacott and Rohrer, 2016). An uncertain heritability has showed by FTD-MND, of which several studies are controversial about its genetics (Woollacott and Rohrer, 2016). In addition to heritability tendency and clinical evidences, genetic screening help clinicians to individuate precise FTD phenotypes features. For instance, bvFTD is usually associated to mutations in each of the three main genes (Mann and Snowden, 2017). However, some clinical aspects are more evident in patients with MAPT mutation, such as behavioural disinhibition, while in GRN and C9orf72 apathy typically prevail. In addition to behavioural disinhibition, MAPT mutations often cause semantic alterations

that results absent in GRN and rarely in C9orf72 (Mann and Snowden, 2017). Similarly, GRN is associated to nfvPPA up to a third of mutation events, while for the remaining part is associated to bvFTD. However, nfvPPA is not connected to MAPT mutations, and it is rare for C9orf72. Lastly, for the overlapping FTD-ALS syndrome, an association with expansions in C9orf72, without mutations in MAPT or GRN, have been found. As a support to the clinical differences in these three main genes, different patterns of atrophy have been observed through neuroimaging techniques. **Figure 4** reports a summary of the associations between clinical and genetic traits and FTD phenotypes.

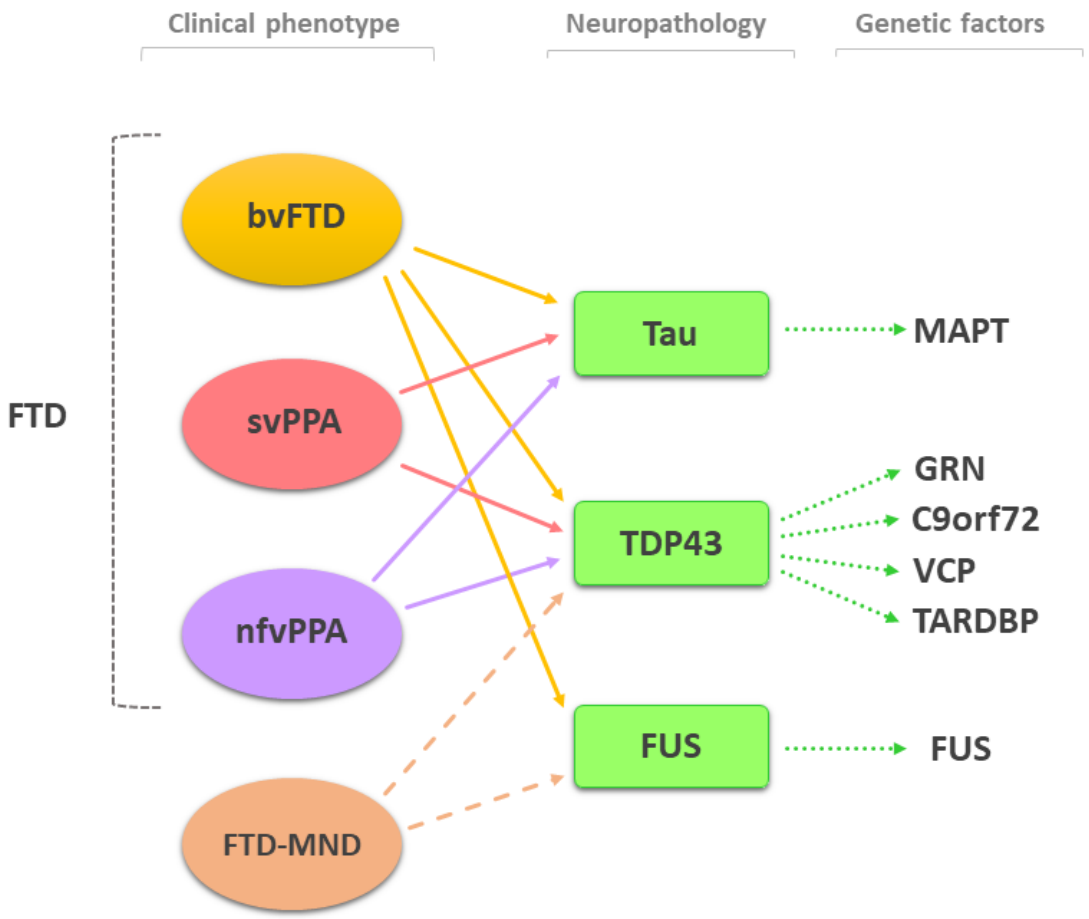

Figure 4. Schematic representation of association among clinical FTD phenotypes and FTD-MND, neurophatological and genetic biomarkers.

4. 4. Neuroimaging FTD biomarkers

Although clinical syndromes contributed to distinguish well-specific patterns of behavioural and language impairments, individual effects variability combined to some overlap of brain regions of interest, lead to a highly heterogeneous scenario (Gordon et al., 2016). Probably, this is due to varied genetic contributions and pathological processes occurring in single subjects (Gordon et al., 2016). Recently, neuroimaging studies focused on enrich the set of information already available, pointing to reach a more specific detail level to improve our understanding of FTD (Mahoney et al., 2015; Whitwell et al., 2011, 2012; Borroni et al., 2008). Each FTD group typically shows a detectable neuroanatomical pattern. Starting from bvFTD, different studies indicated volume loss mainly in frontal and temporal lobes, with involvement of prefrontal cortex, anterior temporal areas, insula region, anterior cingulate, thalamus and striatum (Gordon et al., 2016). Regional patterns in bvFTD are supported at group level but some traits, such as differences in degree of hemispheric asymmetry and in predominance of frontal and temporal lobe atrophy, emerge at individual scale (Gordon et al., 2016). As reviewed by Gordon et al. (2016), from cluster analysis, some studies indicated at least four neuroanatomical subtypes of bvFTD. Two of them show predominantly frontal atrophy with focal frontal-dominant and a more spread frontotemporal subtype, while the other two show predominantly temporal impairments, corresponding to a focal temporal-dominant and a more common temporo-frontal-parietal subtype (Gordon et al., 2016). Concerning svPPA patients, they show a more marked asymmetric temporal lobe atrophy, mostly in the anterior and inferior areas. In the first phase, regional grey matter loss involves inferior temporal and fusiform gyri, temporal pole, and parahippocampal and entorhinal cortex, in addition to amygdala and hippocampus. With the disease progression, the pattern expands anteriorly and posteriorly, involving orbitofrontal, inferior frontal, insular and anterior cingulate cortices in the first case, and temporo-parietal regions in addition to corresponding regions in the contralateral hemisphere for the second case. Although also in nfvPPA patients atrophy involve mostly the left hemisphere cortical regions, their distribution is different from those svPPAs. Firstly, they are included areas as inferior frontal gyrus, dorsolateral prefrontal cortex, and superior temporal gyrus and insula, while other regions are included during the progression of the disease, such as prefrontal and temporal lobe structures, anterior frontal, lateral temporal, and anterior parietal lobes (Gordon et al., 2016).

Beside neuroanatomical features changes, functional brain activities are used to investigate brain deviations in FTD, even if today its literature available is limited (Hohenfeld et al., 2018). Functionally brain networks can be individuated thanks to neuronal activities, measuring the synchronised time-dependent fluctuations in blood oxygenation levels through resting-state fMRI (Gordon et al., 2016). Correlated activations among brain areas can individuate different pattern of spatially distinct cortical and subcortical region, but functionally connected (Gordon et al., 2016). All the three main functional networks are involved in FTD, that are the default mode network (DMN), the salience network (SN), and the executive network (EN), in addition to semantic network (Hohenfeld et al., 2018; Gordon et al., 2016). An interesting relationship between SN and DMN networks have been observed in bvFTD. As reported by Gordon et al. (2016), different studies suggested a reduced activity in areas of the SN, that are responsible of emotional significance and appropriately responses, including frontal lobe, anterior cingulate, insula, amygdala, medial thalamus and ventral striatum (Gordon et al., 2016). This reduced connectivity in SN seems to bring a compensatory phenomenon in DMN, so its connectivity results increased (Hohenfeld et al., 2018; Gordon et al., 2016), even if other studies also found an its connectivity reduction. Some studies demonstrated alterations also in EN, dorsal attention and auditory networks (Hohenfeld et al., 2018).

In svPPA patients, a major reduced connectivity concerns the semantic network, involving left anterior temporal lobe, inferior and ventral regions of temporal lobe, bilateral frontal cortex, left amygdala, hippocampus, caudate and occipital regions (Gordon et al., 2016). A smaller alteration in SN have been found in svPPA respect to bvFTD (Hohenfeld et al., 2018). Instead, there are few evidences about nfvPPA, but preliminary studies indicated a minor connectivity in the frontal operculum, primary and supplementary motor areas, and inferior parietal lobule, that constitute the bridge between language and motor networks responsible of fluent speech (Gordon et al., 2016).

5. Materials and methods

This chapter will describe the analytical methods applied in this work, from data collection, and data elaboration, to graph-based model application and features extraction. **Figure 5** shows the analysis workflow of the rs-fMRI data, discussed in detail below.

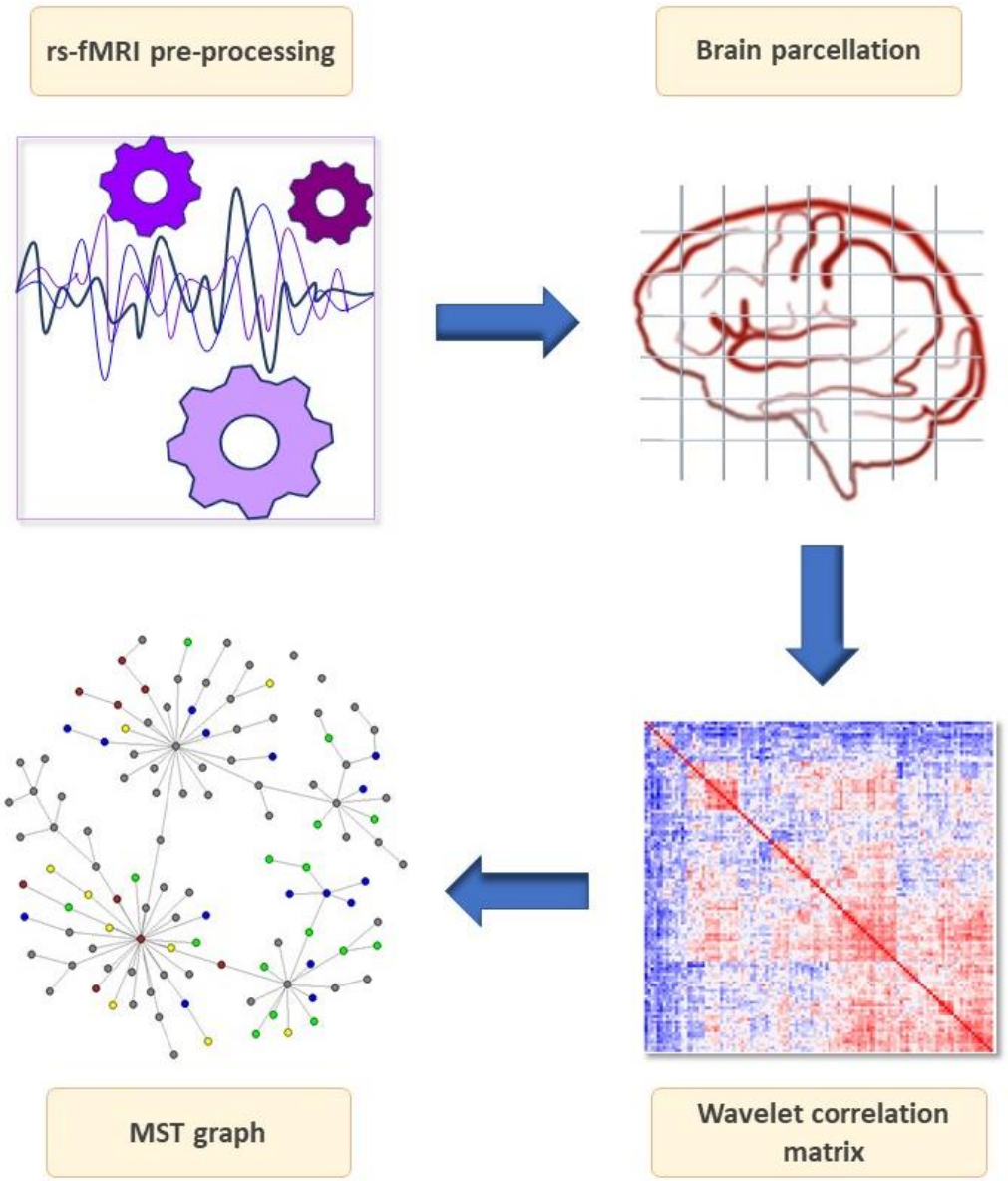

Figure 5. Study workflow of rs-fMRI data.
The figure shows the most important steps of connectome extraction. Pre-processing and brain parcellation are the first phases of rs-fMRI elaboration. Wavelet correlation matrix and minimum spanning tree (MST) network calculation represent the analysis phase. Wavelet transformation was applied to the average voxel time series mapped to AAL 116 brain regions of interest (ROI), from which have been obtained the statistical relationships between nodes (i.e., wavelet correlation matrices). MSTs was extracted from each wavelet correlation matrix. Their parameters and topological features (including edges partition and nodes cluster) have been calculated. Figure modified by Saba et al., 2019.

5. 1. Study design

A group of 41 subjects with a probable bvFTD diagnosis (according to current criteria; Gorno-Tempini, et al., 2011) was recruited at the Centre for Neurodegenerative Disorders, at the University of Brescia (Brescia, Italy). This study concerned sporadic cases of bvFTD, confirmed by a genetic screening for the most frequent monogenic causes of FTD (i.e., GRN, C9orf72 and MAPT; Cosseddu et al., 2018), from which none patients had these pathogenic mutations. In addition, extensive neuropsychological assessment and structural MRI imaging was performed for all subjects.

For the healthy control group, was recruited 39 voluntary individuals, and all subjects performed a brief standardised neuropsychological assessment (Mini-Mental State Examination; with MMSE >= 27). **Table 4** summarizes demographic information of the two groups.

Informed consent was obtained from all participants, and conformed to the Helsinki Declaration, the study was approved by the Brescia Hospital Ethics Committee (Brescia, Italy).

Table 4. Demographic and clinical features of partecipants. For both groups, the values are reported as mean ± standard deviation, and the top letters *a* and *b* indicates independent two-group t-test and Pearson chi-squared test, rispetively. Modified by Saba et al., 2019.

	bvFTD	HC	P-value
Age (year)	65.6 ± 7.01	61.7 ± 6.5	0.010^{a}
Sex	M = 26; F = 15	M = 13; F = 26	0.014^{b}
Education (year)	9.1 ± 3.82	10.3 ± 3.84	0.161^{a}
CDR	6.7 ± 3.84	0.0 ± 0.0	---

CDR = clinical dementia rating

5. 2. Functional magnetic resonance imaging (fMRI)

Brain anatomical or functional large-scale networks can be assessed through different neuroimaging techniques. Brain activity involves neurophysiological techniques, such as electroencephalography (EEG) and magnetoencephalography (MEG), able to detect timing of activity and its locus, measuring electrical and magnetic extra-skull signals, respectively (Farahani et al., 2019; Pievani et al., 2011). Other functional techniques are based on biological signals, for example positron emission tomography (PET) detects changes in metabolism, while functional magnetic resonance imaging (fMRI) focuses on changes in blood oxygenation levels (Farahani et al., 2019). Lastly, structural architecture can be assessed using diffusion tensor imaging (DTI; Farahani et al., 2019). In this work will be discussed the functional brain organization using fMRI signals acquisitions.

PET and fMRI show a lower temporal resolution respect other technique but offer a significant spatial resolution, an advantageous feature to localize signals origin (Farahani et al., 2019). Although PET has a higher spatial resolution than fMRI, it is very expensive and needs radioactive isotopes to work (Farahani et al., 2019). For these reasons, in addition to its non-invasivity and repeatability in adults and children (Gore, 2003), fMRI is becoming popular in neural function studies since it can well describe brain area activities during a specific task, or during resting-state condition (rs-fMRI; Farahani et al., 2019).

Resting-state, also called task-free or intrinsic connectivity fMRI, detects spontaneous low frequency fluctuations in the blood oxygen level dependent (BOLD) signal in quiet conditions, in which patients do not produce specific tasks (Lee et al., 2013; Pievani et al., 2011; Gore, 2003). In this condition, the working-principle of fMRI remains valid: an increment of neuronal activity in a cortex region stimulate an increment of blood flow in response to a higher request of oxygen (Gore, 2003). Specifically, BOLD signal fluctuations express variations of the ratio between oxyhaemoglobin and deoxyhaemoglobin, providing an indirect marker of neuronal activity (Pievani et al., 2011). Although this measure is widely accepted, their interpretation may vary depending on subject conditions, including blood flow, volume within tissue and local oxygen tension changes (Pievani et al., 2011). A typical fMRI feature is the time-delay (several seconds), due to the so-called hemodynamic response. This is necessary after an intensive neural activation, allowing the vasodilatation and the wash-out of the

deoxyhaemoglobin from the locus to occur (Gore, 2003). Imaging acquisition progresses have brought a complete cross-sectional image in less than one second, allowing to detect the hemodynamic responses to transient events without influences from physiological motion. Applying the average of many signals, fMRI- multiple recordings increases data reliability (Gore, 2003).

In this work, all images were obtained using a 1.5T Siemens Avanto MRI scanner (Siemens, Erlangen, Germany) with a circularly polarized transmit-receive coil. In a single session, the following scans were collected from each subject: (i) dual-echo turbo spin echo (TSE) (repetition time = 2500 ms, echo time [TE] = 50 ms), to exclude presence of macroscopic brain abnormalities, according to exclusion criteria; (ii) 3D magnetization-prepared rapid gradient echo (MPRAGE) T1-weighted scan (TR=2050 ms, TE = 2.56 ms, matrix = 1 x 1 x 1, in-plane field of view [FOV] = 256 x 256 mm^2, slice thickness = 1 mm, flip angle = 15°); (iii) T2*-weighted echo planar (EPI) sensitized to blood oxygen level dependent (BOLD) contrast (TR = 2500 ms, TE = 50 ms, 29 axial slices parallel to anterior commissure–posterior commissure line (AC-PC) line, matrix = 64 x 64, field of view = 224 mm, slice thickness = 3.5 mm), gap between slices 1.75 mm for rs-fMRI. EPI images were collected during rest for an 8-minute period, resulting in a total of 196 volumes.

There are several signal noising-factors defined as temporal fluctuation caused by, for example, head movement, scanner instabilities, and physiological noise (Griffanti, et al., 2014; 2015). Although these effects are present also in task-specific fMRI, they mostly affect resting state performance due to the absence of *a priori* assumptions of brain areas activation. Often, it may be difficult to recognize neural activities from non-neural noise when they are correlated, therefore an efficient cleaning procedure is necessary. According to Jenkinson et al. (2012) protocol, fMRI data pre-processing were performed by the Centre for Neurodegenerative Disorders (University of Brescia, Brescia, Italy) using FSL 5.0.8 neuroimaging software.

5. 3. Brain parcellation

The brain parcellation into 116, subdivided in 90 cortical and subcortical, and 26 cerebellar regions of interest (ROIs, **Table 5**) was obtained applying the automated anatomical labelling atlas (AAL; Tzourio-Mazoyer, et al., 2002) on cleaned fMRI data. From each ROI, mean time series was extracted averaging the signal from all its voxels through Marsbar software (http://marsbar.sourceforge.net/; Brett, et al., 2002). Subsequently, we used a descriptive aggregation to obtain 8 (right and left) macro-ROI (referred to as lobes or "macro-regions"): Frontal, Temporal, Occipital, Parietal, Insular, Limbic, Subcortical Grey Matter (SCGM; including Thalamus), and Cerebellum (including Vermis).

Table 5. Keys for brain areas and clusters membership. Table showing AAL 116 brain regions, with AAL Identifiers (Region name), macro-region or lobe (Lobe), lobe short name (Lobe key), MST cluster for patients (bvFTD cluster color), MST cluster for healthy controls (HC cluster color). Published in Saba et al., 2019.

ID	Region name	Lobe	Lobe key	bvFTD clusters color	HC cluster color
1	Precentral_L	Frontal	FroL	red	red
2	Precentral_R	Frontal	FroR	red	red
3	Frontal_Sup_L	Frontal	FroL	green	brown
4	Frontal_Sup_R	Frontal	FroR	green	green
5	Frontal_Sup_Orb_L	Frontal	FroL	green	green
6	Frontal_Sup_Orb_R	Frontal	FroR	green	green
7	Frontal_Mid_L	Frontal	FroL	green	brown
8	Frontal_Mid_R	Frontal	FroR	green	cyan
9	Frontal_Mid_Orb_L	Frontal	FroL	green	green
10	Frontal_Mid_Orb_R	Frontal	FroR	green	green
11	Frontal_Inf_Oper_L	Frontal	FroL	red	red
12	Frontal_Inf_Oper_R	Frontal	FroR	green	red
13	Frontal_Inf_Tri_L	Frontal	FroL	green	brown
14	Frontal_Inf_Tri_R	Frontal	FroR	green	cyan
15	Frontal_Inf_Orb_L	Frontal	FroL	green	brown
16	Frontal_Inf_Orb_R	Frontal	FroR	green	brown
17	Rolandic_Oper_L	Frontal	FroL	red	red
18	Rolandic_Oper_R	Frontal	FroR	green	red
19	Supp_Motor_Area_L	Frontal	FroL	green	red
20	Supp_Motor_Area_R	Frontal	FroR	red	red
21	Olfactory_L	Frontal	FroL	green	green
22	Olfactory_R	Frontal	FroR	green	green
23	Frontal_Sup_Medial_L	Frontal	FroL	green	green

24	Frontal_Sup_Medial_R	Frontal	FroR	green	green
25	Frontal_Med_Orb_L	Frontal	FroL	green	green
26	Frontal_Med_Orb_R	Frontal	FroR	green	green
27	Rectus_L	Frontal	FroL	green	green
28	Rectus_R	Frontal	FroR	green	green
29	Insula_L	Insula	InsL	red	red
30	Insula_R	Insula	InsR	green	red
31	Cingulum_Ant_L	Limbic	LimL	green	green
32	Cingulum_Ant_R	Limbic	LimR	green	green
33	Cingulum_Mid_L	Limbic	LimL	red	red
34	Cingulum_Mid_R	Limbic	LimR	red	red
35	Cingulum_Post_L	Limbic	LimL	yellow	brown
36	Cingulum_Post_R	Limbic	LimR	yellow	brown
37	Hippocampus_L	Limbic	LimL	cyan	cyan
38	Hippocampus_R	Limbic	LimR	yellow	cyan
39	ParaHippocampal_L	Limbic	LimL	cyan	cyan
40	ParaHippocampal_R	Limbic	LimR	yellow	cyan
41	Amygdala_L	Limbic	LimL	cyan	cyan
42	Amygdala_R	Limbic	LimR	grey	cyan
43	Calcarine_L	Occipital	OccL	cyan	cyan
44	Calcarine_R	Occipital	OccR	cyan	cyan
45	Cuneus_L	Occipital	OccL	yellow	cyan
46	Cuneus_R	Occipital	OccR	cyan	cyan
47	Lingual_L	Occipital	OccL	cyan	cyan
48	Lingual_R	Occipital	OccR	cyan	cyan
49	Occipital_Sup_L	Occipital	OccL	cyan	cyan
50	Occipital_Sup_R	Occipital	OccR	cyan	cyan
51	Occipital_Mid_L	Occipital	OccL	cyan	cyan
52	Occipital_Mid_R	Occipital	OccR	cyan	cyan
53	Occipital_Inf_L	Occipital	OccL	cyan	cyan
54	Occipital_Inf_R	Occipital	OccR	cyan	cyan
55	Fusiform_L	Occipital	OccL	cyan	cyan
56	Fusiform_R	Occipital	OccR	cyan	cyan
57	Postcentral_L	Parietal	ParL	red	red
58	Postcentral_R	Parietal	ParR	red	red
59	Parietal_Sup_L	Parietal	ParL	yellow	cyan
60	Parietal_Sup_R	Parietal	ParR	yellow	cyan
61	Parietal_Inf_L	Parietal	ParL	yellow	cyan
62	Parietal_Inf_R	Parietal	ParR	red	cyan
63	SupraMarginal_L	Parietal	ParL	red	red
64	SupraMarginal_R	Parietal	ParR	red	red
65	Angular_L	Parietal	ParL	yellow	brown

66	Angular_R	Parietal	ParR	yellow	brown
67	Precuneus_L	Parietal	ParL	yellow	brown
68	Precuneus_R	Parietal	ParR	yellow	brown
69	Paracentral_Lobule_L	Parietal	ParL	red	red
70	Paracentral_Lobule_R	Parietal	ParR	red	cyan
71	Caudate_L	SCGM	SCGL	green	cyan
72	Caudate_R	SCGM	SCGR	green	cyan
73	Putamen_L	SCGM	SCGL	red	red
74	Putamen_R	SCGM	SCGR	green	red
75	Pallidum_L	SCGM	SCGL	red	red
76	Pallidum_R	SCGM	SCGR	green	red
77	Thalamus_L	SCGM	SCGL	red	brown
78	Thalamus_R	SCGM	SCGR	red	brown
79	Heschl_L	Temporal	TemL	red	red
80	Heschl_R	Temporal	TemR	green	red
81	Temporal_Sup_L	Temporal	TemL	red	red
82	Temporal_Sup_R	Temporal	TemR	green	cyan
83	Temporal_Pole_Sup_L	Temporal	TemL	red	cyan
84	Temporal_Pole_Sup_R	Temporal	TemR	yellow	cyan
85	Temporal_Mid_L	Temporal	TemL	yellow	brown
86	Temporal_Mid_R	Temporal	TemR	yellow	brown
87	Temporal_Pole_Mid_L	Temporal	TemL	red	cyan
88	Temporal_Pole_Mid_R	Temporal	TemR	yellow	green
89	Temporal_Inf_L	Temporal	TemL	cyan	cyan
90	Temporal_Inf_R	Temporal	TemR	cyan	cyan
91	Cerebellum_Crus1_L	Cerebellum	CerL	cyan	cyan
92	Cerebellum_Crus1_R	Cerebellum	CerR	cyan	cyan
93	Cerebellum_Crus2_L	Cerebellum	CerL	cyan	cyan
94	Cerebellum_Crus2_R	Cerebellum	CerR	cyan	cyan
95	Cerebellum_3_L	Cerebellum	CerL	cyan	cyan
96	Cerebellum_3_R	Cerebellum	CerR	cyan	cyan
97	Cerebellum_4_5_L	Cerebellum	CerL	cyan	cyan
98	Cerebellum_4_5_R	Cerebellum	CerR	cyan	cyan
99	Cerebellum_6_L	Cerebellum	CerL	cyan	cyan
100	Cerebellum_6_R	Cerebellum	CerR	cyan	cyan
101	Cerebellum_7b_L	Cerebellum	CerL	cyan	cyan
102	Cerebellum_7b_R	Cerebellum	CerR	cyan	cyan
103	Cerebellum_8_L	Cerebellum	CerL	cyan	cyan
104	Cerebellum_8_R	Cerebellum	CerR	cyan	cyan
105	Cerebellum_9_L	Cerebellum	CerL	cyan	brown
106	Cerebellum_9_R	Cerebellum	CerR	cyan	brown
107	Cerebellum_10_L	Cerebellum	CerL	grey	grey

108	Cerebellum_10_R	Cerebellum	CerR	grey	grey
109	Vermis_1_2	Cerebellum	CerL	cyan	cyan
110	Vermis_3	Cerebellum	CerR	cyan	cyan
111	Vermis_4_5	Cerebellum	CerL	cyan	cyan
112	Vermis_6	Cerebellum	CerR	cyan	cyan
113	Vermis_7	Cerebellum	CerL	cyan	cyan
114	Vermis_8	Cerebellum	CerR	cyan	cyan
115	Vermis_9	Cerebellum	CerL	cyan	cyan
116	Vermis_10	Cerebellum	CerR	cyan	cyan

5. 4. Wavelet correlation of brain regions

For each subject, the final dataset (i.e., pre-processed and parcelled dataset) was composed by 193 mean time-series extracted from each brain region. Statistical relationship between brain region can be calculated through several correlation estimate (Zhang et al., 2016; Zalesky et al., 2012): in this work, we used wavelet correlation.

Wavelet decomposition was applied on each temporal series characterized by weighted coefficients, proportional to the total amount of energy emanated from the system, relative to a defined scale and brain location (Bullmore et al., 2004). Considering the total energy as a frequency-time, temporal series can be processed at different hierarchical scale resolutions. Specifically, the low-frequency components correspond to coefficients of approximative scale, while the high-frequency components indicate finer scale coefficients (Bullmore et al., 2004). In each decomposition scale, wavelet analysis ensures high flexibility for non-stationary characteristics of the data, favouring its multi-modularity application to fMRI data (Bullmore et al., 2004). Therefore, wavelet correlation guarantees a more homogeneous representation of the original time series and their transformations thanks to a higher robustness and noise reduction (Zhang et al., 2016; Bullmore et al., 2004).

We applied the maximal overlap discrete wavelet transform (MODWT; Achard, et al., 2006) with a Daubechies wavelet filter (length equal to 8) to band-pass filter on mean time series, and calculate wavelet coefficients for the wavelet scales, as indicated by Zhang et al. (2016). The frequency ranges (or scales) obtained by a wavelet decomposition directly depend on the sampling frequency of the data, so that our TR was equal 2500 ms (Nyquist frequency = 0.2 Hz) and then four frequency bands (i.e., scales) were used; scale one: 0.2-0.1 Hz; scale two: 0.05-0.1 Hz; scale three: 0.025-0.05 Hz; and scale four: 0.013-0.025 Hz. Successively, we calculated the correlation matrix for each subject, whose *ij*th elements were established by the estimated wavelet correlations between brain regions *i* ($\lambda_i^{(s)}$) and region *j* ($\lambda_j^{(s)}$):

$$r_{ij} = \frac{cov(\lambda_i^{(s)}; \lambda_j^{(s)})}{\sqrt{var(\lambda_i^{(s)})var(\lambda_j^{(s)})}}$$

We used bvFTD/HC connectivity-based Wilcoxon rank sum tests to compare the four scales and select the frequency band with higher informative content. We focused on wavelet decomposition scale two (s = 2), as only this scale reached the significance in bvFTD/HC bivariate connectivity global measures (**Table 6**). In particular, we quantified bivariate connectivity of the wavelet correlation matrix for each subject (Lynall, et al., 2010), with three global measures: (i) *strength*, defined as the average of columns mean; (ii) *diversity,* defined as the average of the columns variance, and (iii) *zero correlation,* defined as the number of correlations with P > 0.05, testing the null hypothesis, H_0: $\rho_{ij} = 0$ (see paragraph 5.6).

5. 5. MST-based method

As introduced in the Preface (and Chapter 1), several common graph approaches are affected by dependence from fixed graph features (e.g., fixed density or node degree). We used a minimum spanning tree (MST) based-method to overcome issues concerning arbitrary threshold, characterized by connections that minimize the sum of edge-weights, excluding edges that form a cycle (Stam, et al., 2014). Among existing methods for MST search, we applied the Prim's algorithm (Cormen, et al., 2001). Tanks to its efficient structure, characterized by N nodes and E = (N-1) edges, it yields perfectly comparable networks among different samples, without dependences from vertices and edges number variability. It represents the best possible synthesis of the original graph information, achieved through the most important subgraph (Stam, et al., 2014).

We used MST global measures (definitions in **Table 2**, chapter 2, paragraph 2.3) to characterize network configurations (star- or linear- shape; **Figure 6**), providing information on graph centrality (k_{max} and $B_{\max}$), distance (d and *Ecc*), association (*Ass*), and topological features (K and *Lf)*. Specifically, a star-type configuration ensures a better network integration with an increase of maximum betweenness $B_{\max}$ and leaf fraction *Lf*, and a decrease of diameter d and eccentricity *Ecc* (van Lutterveld, et al., 2017). In addition, maximum betweenness $B_{\max}$ and degree divergence K correlate positively with the presence of some high-degree tree nodes in a network (Mears and Pollard., 2016). Lastly, positive assortativity (Ass > 0) indicates that nodes with same degree tend to connect, so that the high degree nodes (hubs) tend to be connected to each other (Bullmore and Sporns, 2009). However, in biological networks with

hierarchical structure is typical a negative assortativity (Ass < 0), where hubs are connected to nodes with lower degree nodes (Newman, 2003).

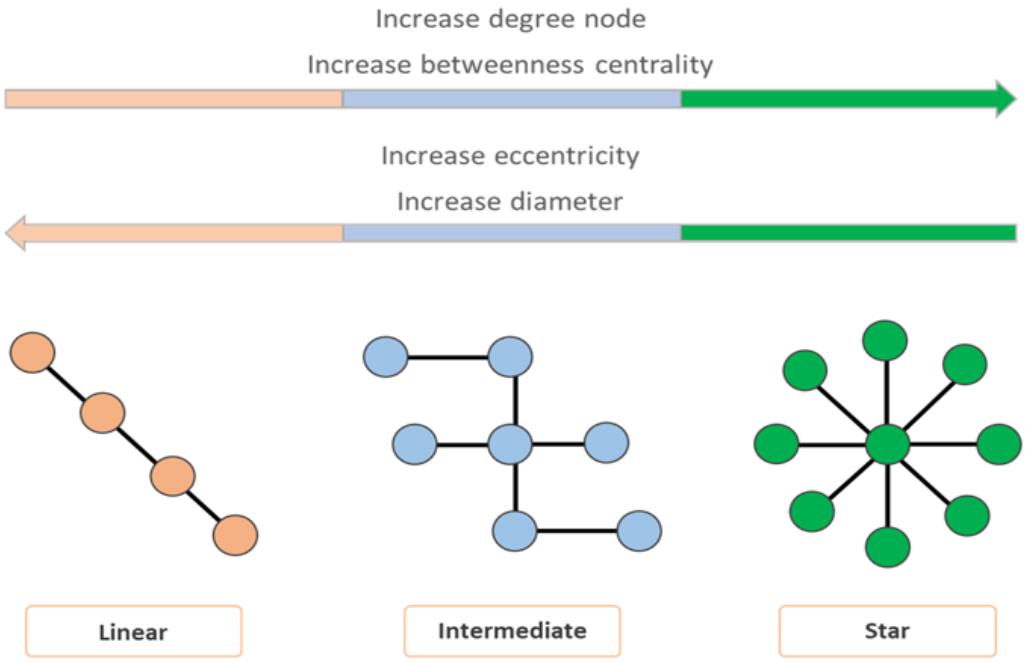

Figure 6. **MST configurations with main features.** Linear and star shapes represent the extreme MST configurations. Star-shape shows the better network integration, contrary to linear-shape configuration characterized by lowest efficiency. The figure is adjusted from (Numan et al., 2017; van Dellen et al., 2014).

5. 6. Topological overlap measure (TOM) and shortest path tree (SPT)

In the present study, we implemented a procedure to avoid some of the intrinsic limitations of the MST approach: the absence of triangular connections (i.e. absence of clustering metric) and graph sparseness with a limited number of edges of the resulted network.

First, we applied *topological overlap measures* (TOM; Mumford et al., 2010; Zhang and Horvath 2005; Ravasz et al., 2002) to the network adjacency matrix to compensate the absence of triangular connections in the MST. This allowed to analyse MSTs in terms of aggregation or clustering without biases. Specifically:

$$TOM_{ij} = \frac{l_{ij} + a_{ij}}{min\{k_i, k_j\} + 1 - a_{ij}}$$

where $l_{ij} = \sum_u a_{iu}\, a_{ju}$ is the overlap estimate between two nodes neighborhoods, a_{ij} is the ijth-element of adjacency matrix, k_i and k_j are the degree measures of ith-node and jth-node, expressed as $k_i = \sum_{u \neq i} a_{iu}$; $k_j = \sum_{u \neq j} a_{ju}$. Two nodes have a greater overlap if their relationship and with their common nodes is high (Mumford, et al., 2010). Therefore, TOM modulates neighbourhood characteristics of nodes, quantifying the topological overlap between two nodes against all other nodes in the network. Nodes with high TOM values identify a neighbourhood (Ravasz et al, 2002).

Secondly, MST is characterized by (N-1) edges, resulting a sparse graph with a limited number of edges. Therefore, through the *shortest path tree* (SPT) problem (Meier, et al., 2015; Van Mieghem and Magdalena, 2005), we evaluated the network performance of MST, quantifying if MST is a satisfactory representation of the whole graph (i.e., whether the sparse tree may be considered as a critical backbone of original network; Tewarie, et al., 2014). An SPT is mainly sensitive to the small, non-negative link weights, around zero. Starting with a full graph *G*, the probability distribution for the link weights of G around zero can be described by a power distribution: $F(x) = \Pr(X \leq x) \sim x^{\alpha}$, where $x \in [0,1]$ represents weights, and the exponent $\alpha > 0$, defines the *extreme value index* of the probability distribution (Van Mieghem and Magdalena, 2005). Three specials α-trees correspond to precise α ranges. The $\alpha \to \infty$ regime matches a unique weight for all links (i.e., *w* = 1). In the $\alpha = 1$ regime, link weights result to be uniformly distributed. Finally, in the $\alpha \to 0$ regime, link weights show strong fluctuations. For $\alpha \to 0$, defined as the *stronger disorder condition*, the shortest path tree of G coincide with a MST (Van Mieghem and Magdalena, 2005; Van Mieghem and van Langen, 2005), and the information flow within the network follows only MST links (Meier, et al., 2015).

Therefore, we tested the $\alpha \to 0$ regime (i.e., MST) of the weighted original graph *G* for each subject in three steps:

1) Define a full graph *G* (*N, E*) by fixing to zero the not statistically significant (P > 0.05) wavelet correlations, r_{ij}. The null hypothesis: H_0: $\rho_{ij} = 0$ was evaluated with the Mutual Information test, $MI = -N \ln(1 - r_{ij}^2)/2$ (Edwards, et al., 2010), where N is the number of brain areas.

2) Apply topological overlap measures (i.e., TOM) to the matrix $R^{(0)}$, where $r_{ij}^{(0)} = r_{ij}$ if P < 0.05 and $r_{ij}^{(0)} = 0$ if P ≥ 0.05. MST was created by edges weights defined as:

$w_{ij} = \min\left(1/TOM_{ij}\,; 100\right)/100$. This transformation ensures that weights are enclosed in the range [0, 1], and the most important edges (with small weights, i.e. large TOM values) represent the strongest neighbourhood connections.

3) Ranking weights w_{ij} in descending order and estimating the α exponent from the power function $F(x) = c \cdot x^{\alpha}$, by plotting *Y* = log10 (*F*(*x*)) versus *X* = log10 (*x*). A straight line with an R-squared index approaching 1 is indicative of good fit to the power function, and slope $\hat{\alpha} \rightarrow 0$ indicates SPT coincidence with MST.

5. 7. Edges partition and nodes clustering in MST

Two-group comparisons of topological MST properties were applied to the individual wavelet correlation matrices, between bvFTD and HC, averaged over subjects. Topological structure of nodes and links in an MST have a key role to capture paths with higher importance in information flow (Meier, et al., 2015). It is possible to identify an MST subnetwork showing a higher average node (or link) betweenness centrality compared to the rest of MST (Wu et al., 2006). In other terms, this subset of nodes (or links) is used more often than others, and their paths can be considered as a set of superhighways (SHW) in MST, i.e. the most important "roads". Other links in MST constitute "secondary roads". Identifying SHW enabled to subdivide MST edges (links) in two distinct components with significantly different transport properties.

Based on SHW's definition, we applied the method suggested by (Wu, et al., 2006), on both scale-free and Erdos-Renyi (i.e., random) networks, for edges partition in MST. Briefly, considering the fully connected network with the previous TOM-based link weights, we extracted one MST for each case-control group. Through an iterative process, we removed links in descending order of their weights and calculated the degree divergence value (K), which decreases in each cycle with link removals. As demonstrated by (Braunstein, et al., 2007), the process ends when K < 2, and the largest remaining component is the SHW set.

Lastly, we measured node betweenness differences (i.e., bvFTD – HC) to assess the amplitude of information flow connectivity gain or loss, and we defined a threshold *b* as the non-zero median of the absolute betweenness differences. Areas showing differences above b (or below -b), will be taken as markers of functional connectivity gain (or loss).

Clustering nodes in a tree is more complex respect to other graphs. Several types of clustering algorithms have been developed which revealed to be limited and unsuitable to MST characteristics (Yu, et al., 2015). Here, we used a novel approach for MST clustering suggested by (Yu, et al., 2015) based on the geodesic distance matrix D, where the ijth-elements of D represent the number of links of a shortest path between two nodes. As proposed by the authors, we computed vector similarities as the Spearman's distance, $d_S = 1 - r_S$, where r_S is the Spearman's rank correlation between all row pairs of D. Next, we applied the iterative hierarchical clustering algorithm, using d_S as input and average-linkage method (Gordon, et al., 2016) to define the distance between two clusters. This method merges node pairs into corresponding clusters by decreasing similarity until all nodes are merged into one cluster. The different stages of the algorithm were represented in the form of a dendrogram. We partitioned the case-control MSTs in an equal number of clusters using the same cut-off value (0.2) on each case-control dendrogram.

5. 8. Methodological comparison

MST properties were compared with other common graph theory approaches to measure the extent of network metrics reproducibility and wavelet scale specificity. As first method we applied the efficiency cost optimization (ECO; De Vico Fallani, et al., 2017) criterion, imposing a fixed edge density threshold, based on the trade-off between network efficiency and wiring cost. We further applied two methods defining per subject optimal correlation thresholds, based on the extended Bayesian information criterion (EBIC; Foygel and Drton, 2010), and spectral analysis (Borate et al., 2009; Perkins and Langston, 2009). Finally, we tested the performances of a scale free model-based method that chooses the correlation threshold optimizing power law fitting for each subject (Mumford, et al., 2010).

ECO algorithm filters connectivity based on the optimization of two fundamental properties of complex networks (including brain): wiring cost economy and connection efficiency (De Vico Fallani et al., 2017). Modularity (segregation) and, simultaneously, integration of information, summarized in global and local efficiency parameters, are used to characterize either structural or functional brain networks structure. In complex systems, wiring economy tends to minimize the number of links (i.e., the connection cost), leading to a sparse network, yet optimizing information flow among nodes and communities. According to this principle, ECO suggests a density threshold filtering out the weakest links, maximizing the ratio between the overall efficiency and its wiring costs. Its formulation depends on the connection density that maximize the quality function:

$$J = \frac{E_g + E_l}{\rho}$$

where $E_g$and E_l represent the global and local network efficiency respectively, and ρ is the connection density, whose formulations and values are defined a priori for different network topology (De Vico Fallani et al., 2017). As exposed above and in chapter 1, MST offers the same efficiency/economy-based approach, with the further advantage of no need for a priori optimization function and full reproducibility for different subject, in different conditions.

EBIC evaluates the best-fit model using the extended Bayesian information criteria for multivariate data generated by sparse graphical models (Foygel and Drton, 2010). Considering all possible models with equal priors (i.e., parameters), model selection consists in the choosing the one with minimum BIC value:

$$BIC_\gamma(E) = -2l_n(\widehat{\Theta}(E)) + |E|\ log\ n + 4\ |E|\gamma\ log\ p$$

where E is the edges set of a graph and $l_n(\widehat{\Theta}(E))$ indicates the maximized log-likelihood function of the associate model. The criterion is indexed by γ parameter $\in [0, 1]$, in which if $\gamma = 0$ the classical BIC is recovered. The parameters *p* and *n* represent the number of variables and the sample size, respectively. When γ is positive, EBIC shows strong improvement in false discovery rate over the classical BIC, and even more so over cross-validation (Foygel and Drton, 2010). Starting from $\gamma = 0.5$, we tested different graphs using a correlation thresholds set (between 0.5 and 0.95), from which we choosed the graph with minimum EBIC.

Spectral analysis threshold uses an euristic approach to identify an appropriate network cut-off (Borate et al., 2009). Starting from a defined threshold, the procedure creates a graph from correlation matrix, whose links exceeds the threshold. The graph is represented as an adjacency matrix (A) and a degree matrix (D). From spectral graph theory, the Laplacian matrix is expressed as A-D, from which eigenvalues and eigenvector are computed. Considering the eigenvector associate with the smallest non-zero eigenvalue, it is possible to calculate the number of clusters using a sliding window (10 elements wide), identifying a new cluster when the highest minus lowest value in the window exceeded the *median value + std. dev /2*. This procedure is repeated from a correlation threshold equal to 0.99 to incrementally smaller correlation (0.01), until the maximum number of clusters per iteration if found. The corresponding threshold is considered the best one. Eigenvalues and eigenvectors decomposition of the Laplacian matrix should avoid the problem of finding an arbitrary threshold, returning cut-off values based on the underlying data community structure.

Scale-free model selects the optimal weighted power of the weighted correlation matrix that maximize the scale free nature of the network, avoiding the choice of an arbitrary correlation threshold (Mumford et al., 2010). Scale free has a biologically plausible connectivity distribution, even if, as discussed in the chapter 2, many studies contest this point of view concerning functional brain network. Starting from Pearson correlation between all pairs of voxels (r_{ij}), Mumford et al. (2010) used a signed similarity measure defined as $s_{ij} = \frac{r_{ij}+1}{2}$, and the soft power adjacency function results in $a_{ij} = {s_{ij}}^{\beta}$ for i≠j, while $a_{ij} = 0$ when i=j. Fixing the power parameter β, they used the scale free fit index $R^2 = cor(\log(p(k)), \log(k))^2$ to obtain the power of adjacency matrix that maximize the scale free nature of the network. R^2 of a transformed network is a function of β. The choice condition follows scale-free distribution criterion, selecting only whose parameters value that well-approximate the scale-free topology, such as R^2 higher than 0.8. The main limitation of this work is the enforcing of a scale free network nature, that from one hand cannot fully represent the biological system, and on the other hand could yield very different and non-reproducible results at different data scales and resolutions.

Differently from MST topology, these networks include triangular connections and cycles (i.e., they are not acyclic graphs), where classical clustering-based indices can be calculated. MST-

specific indices are leaf fraction and alpha, while non-MST indices include clustering coefficient, average path length, and efficiency. Common metrics include maximum degree, maximum betweenness, degree divergence, diameter, eccentricity, and assortativity. Wilcoxon rank sum tests were calculated for every method at each wavelet scale.

5. 9. Statistical analysis

Global network connectivity (strength, diversity, and zero correlation), and MST global parameters (maximum degree, maximum betweenness, diameter, eccentricity, assortativity, degree divergence, leaf fraction, extreme value index, R-squared), provided a dataset of 80 rows (subjects) and 12 columns (parameters) for further statistical analysis. Since data were generally not Gaussian, non-parametric, Wilcoxon signed rank test was used to compare FTD and HC groups P-values were adjusted using Benjamini–Hochberg correction, and fixing the significance threshold at $P < 0.05$ (two sided). Sex and age showed significant differences between groups; therefore, data were corrected for age, sex and age*sex interaction.

Global measures from the two case-control average correlation matrices were also compared by permutation tests as follows: (i) by computing the observed absolute difference between the global measure in FTD and HC groups, (ii) by permuting group assignments of the individuals' values of the global measures for FTD and HC groups (B = 10000 iterations), and (iii) by repeating step (i) to obtain B = 10000 sampled permutations of the absolute differences between FTD and HC groups. Then, P-values were obtained using the sample permutation distribution with the same significant threshold of the individual signed rank tests.

5. 10. Software

Network analyses, graph visualization, and statistical analyses were performed in R (R Core team, 2018), using packages igraph (Csardi and Nepusz, 2006), WGCNA (Langfelder and Horvath, 2008), brainwaver (Achard, 2015), brainGraph (Watson, 2018), huge (Zhao et al., 2012) and custom R functions.

6. Results

6. 1. Global functional connectivity and stronger disorder limit

For each subject, we examined the complexity of rs-fMRI data using bivariate measures (i.e., strength, diversity, and zero correlation) computed as summary regional values of the wavelet correlations (**Table 6**). Scale 2 was the only reaching significance at these three tests (**Figure 7** and **Table 6**). In bvFTD respect to HC, diversity and zero correlation showed a significant increase, while strength showed significant decrease ($P < 0.05$ for every test). The significant increment of wavelet correlation diversity and its percentage of zeros (median HC: 25% vs. median bvFTD: 35%) indicated a decreased heterogeneity and increased null functional connectivity between brain regions in bvFTD compared to HCs. In addition, strength decrease denounces a generalized connectivity weakening in bvFTD respect to HCs.

By analysing TOM-based weighted fully connected graphs for each subject (see Materials and methods, paragraph 5.7), we obtained good fitting for the power function (**Figure 7** and **Table 6)**. High R^2 (R-squared) indices were observed in both groups (0.93-0.97 for HC and 0.90-0.99 for bvFTD). When the extreme value index was estimated ($\hat{\alpha}$), excluding outliers, low values (0.14-0.57 for HC and 0.10-0.42 for bvFTD) were found. Values of $\hat{\alpha}$ less than 1 indicated a strong disorder limit tendency.

6. 2. MST global graph metrics

MSTs indicated brain connections alterations in bvFTD patients when compared to controls (**Figure 7** and **Table 6**). Data suggested a reduction of the degree centrality and leaf fraction, and an increment of distance metrics in the bvFTD group. Their trees were composed by nodes with a lower maximum degree and number of leaves. Moreover, the trees were characterized by a higher inter-distance, translating in a higher diameter and eccentricity in bvFTD compared to HC trees. These measures indicated brain impairments in bvFTD, highlighting less node-connections and loss of efficiency in exchange information capacity, that support a linear-shaped configuration network. Conversely, HC tree metrics showed a better network integration, characterised by parameter values that tend to a star-type configuration (i.e., an

increase in the number of hubs and leaf points, and a decrease of diameter and eccentricity). Although assortativity index was not significant, it confirmed the topological hierarchy and biological nature of all MSTs, with assortativity values less than 0, for both groups. Lastly, permutation testing of two-group differences on the average correlation matrices yielded similar results (data not shown).

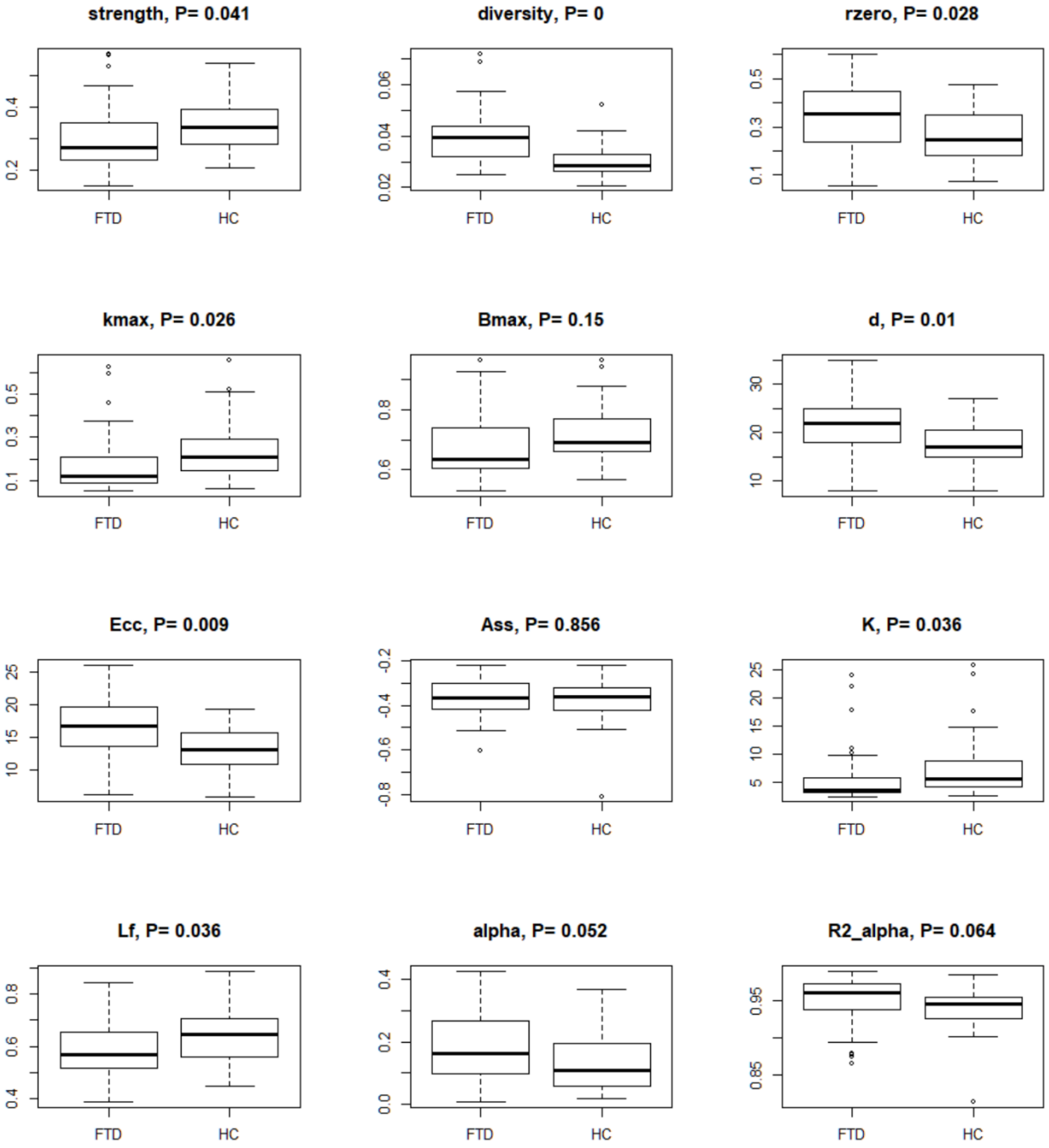

Figure 7. Box-plots with P-values for global connectivity measures and MST global parameters comparisons through Wilcoxon rank sum test. The null hypothesis of the test is that the distributions of the HC and bvFTD do not differ (i.e., true location shift equal to 0). A Benjamini–Hochberg p-values adjustment and age, sex, and age*sex interaction data corrections were used.

Table 6. Wilcoxon rank sum tests for global connectivity parameters at every scale for the Minimum Spanning Tree (MST) method. Wilcoxon rank sum tests in bvFTD subjects versus HCs are shown. Tests estimate differences (Estimate column) are calculated for each scale (1 to 4), for every global connectivity parameter. Estimates are adjusted for age, sex, and age*sex interaction. Strength, diversity, and rzero are directly derived from the correlation matrix, while the other metrics refer to the resulting networks.

	Estimate	Lower CI95%	Upper CI95%	P-value	Adjusted P	
Dmax	0,01442	-0,01448	0,04255	0,34255	0,47267	
kappa	0,21579	-0,28824	0,73230	0,34255	0,47267	
Lf	0,01673	-0,03254	0,05984	0,55265	0,64476	
Bmax	0,01746	-0,02807	0,06148	0,37138	0,47267	
d	2,10417	0,00000	4,58333	0,05925	0,20737	
Ecc	1,68624	-0,05496	3,32904	0,05894	0,20737	**SCALE 1 (0.1-0.2 Hz)**
Ass	-0,11588	-0,39607	0,00357	0,05894	0,20737	
alpha	-0,01197	-0,06604	0,04685	0,73758	0,79432	
R2_alpha	0,00712	-0,00282	0,01499	0,16365	0,37022	
strength	-0,02068	-0,05407	0,01853	0,25759	0,45078	
diversity	0,01146	0,00648	0,01651	0,00001	**0,00019**	
rzero	0,04168	-0,01975	0,10343	0,12638	0,35387	
Dmax	-0,05762	-0,10164	-0,01739	0,00735	**0,02572**	
kappa	-1,18848	-2,51235	-0,22204	0,01731	**0,03626**	
Lf	-0,05269	-0,10142	-0,00993	0,01813	**0,03626**	
Bmax	-0,03524	-0,07124	0,00928	0,12881	0,15027	
d	4,00000	1,83333	6,19437	0,00216	**0,01006**	
Ecc	2,93085	1,15884	4,91268	0,00127	**0,00890**	**SCALE 2 (0.05-0.1 Hz)**
Ass	0,00208	-0,03263	0,03961	0,85569	0,85569	
alpha	0,04668	0,00224	0,09600	0,03712	0,05197	
R2_alpha	0,01287	-0,00001	0,02221	0,05034	0,06407	
strength	-0,04348	-0,08428	-0,00587	0,02562	**0,04061**	
diversity	0,00818	0,00473	0,01162	0,00000	**0,00006**	
rzero	0,07991	0,01578	0,13949	0,01000	**0,02799**	
Dmax	-0,03310	-0,09612	0,02609	0,26577	0,50231	
kappa	-1,03387	-2,51607	0,44432	0,15788	0,50231	
Lf	-0,02024	-0,06730	0,03615	0,49489	0,69040	
Bmax	-0,02928	-0,07750	0,02170	0,28269	0,50231	
d	2,00000	-0,87468	4,89493	0,16584	0,50231	
Ecc	1,64220	-0,43966	4,12897	0,13127	0,50231	**SCALE 3 (0.025-0.05 Hz)**
Ass	-0,01353	-0,06186	0,03039	0,59178	0,69040	
alpha	0,00773	-0,02620	0,04472	0,59178	0,69040	
R2_alpha	-0,01004	-0,02795	0,00671	0,24957	0,50231	
strength	-0,00800	-0,06312	0,05292	0,81830	0,81830	
diversity	0,00364	-0,00266	0,00991	0,28703	0,50231	

rzero	0,01044	-0,05878	0,07106	0,74482	0,80211	
Dmax	0,02005	-0,02236	0,07560	0,27097	0,97290	**SCALE 4 (0.013-0.025 Hz)**
kappa	0,55049	-0,73763	2,08696	0,31399	0,97290	
Lf	0,00862	-0,03823	0,05606	0,69643	1,00000	
Bmax	0,02674	-0,01439	0,08160	0,18834	0,97290	
d	-0,60417	-3,15036	1,92892	0,67527	1,00000	
Ecc	-0,66379	-2,58496	1,30105	0,55265	1,00000	
Ass	0,00502	-0,04325	0,04635	0,90098	1,00000	
alpha	-0,00287	-0,02025	0,01554	0,73037	1,00000	
R2_alpha	0,01017	-0,01086	0,03014	0,34747	0,97290	
strength	0,00678	-0,05874	0,08161	0,90098	1,00000	
diversity	-0,00007	-0,01233	0,01199	1,00000	1,00000	
rzero	-0,01035	-0,06976	0,05427	0,68581	1,00000	

Legend: Estimate = estimated median of the pairwise differences between subjects in bvFTD against HCs; Lower CI95% = lower bound of the confidence interval (95%); Upper CI95% = upper bound of the confidence interval (95%); P-value = nominal P-value of the Wilcoxon test; Adjusted P = Benjamini-Hochberg adjusted P-value; Dmax = maximum degree; kappa = digree divergence; Lf = leaf fraction; Bmax = maximum betweenness; d = diameter; Ecc = eccentricity; Ass = assortativity; alpha = extreme value index; R2_alpha = R-squared of the alpha index; rzero = zero correlation.

6. 3. MST topological two group comparison

Cluster, spatial, and anatomical data were integrated through a network representation, showing the topological properties of the two-group average for HC and bvFTD graphs (see Materials and methods section, paragraph 5.7). The results of edge partitioning and node clustering are shown in **Figure 8** (A), (B) and **Figure 9** (A), (B). Every node in **Figure 8** (A), (B), coloured by cluster membership, correspond to a single brain area belonging to a specific macro-region or lobe (i.e., node name), and traversed by two kinds of functional connections: (i) superhighways (bold grey), and (ii) secondary functional routes (thin grey). Finally, **Figure 10** (A), (B) displays lobe partition (node colour), node degree centrality (node size), and superhighways information flow connectivity (edge thickness) for bvFTD and HC groups, respectively.

In **Figure 8** (A), (B) and **Figure 10** (A), (B) emerged the HC multiple-star structure, whose central nodes, namely Lingual-L, Occipital-Inf-R, Precuneus-L, and Cerebellum-6-L regions (nodes #47, #54, #67, and #99 in **Figure 10** (B)), serve as starting points for superhighways and bridge components in the tree backbone. This architecture was impaired in the MST of bvFTD

patients, where few conserved stars, namely Precuneus-L and Cerebellum-6-L (nodes #67 and #99 in Figure **10** (A)), maintained a reduced functional connectivity, leading to a general isolation of Frontal and Temporal areas from central nodes.

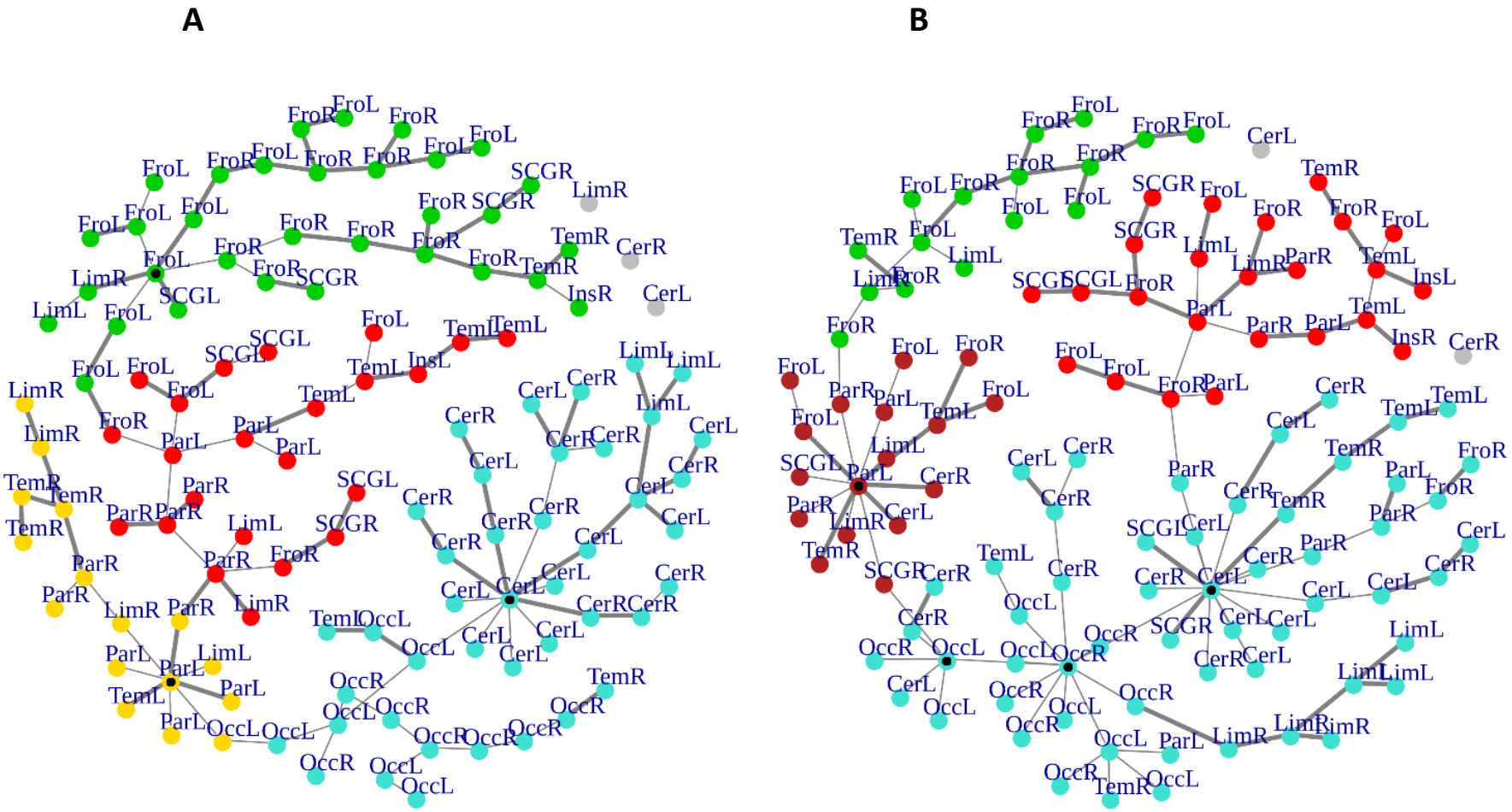

Figure 8 (A), (B). Node clusters and superhighways differences in brain macro-regions. MST for both bvFTD and HCs are shown on the left (A) and right (B) panel, respectively. Node colours define clusters, while thick edges show superhighway paths. A black dot indicates nodes with higher degree centrality (k > 5; i.e., hubs). Nodes are labelled according to macro-regions (i.e., lobes) membership (see Table 5 for label encodings). Figure published in Saba et al., 2019.

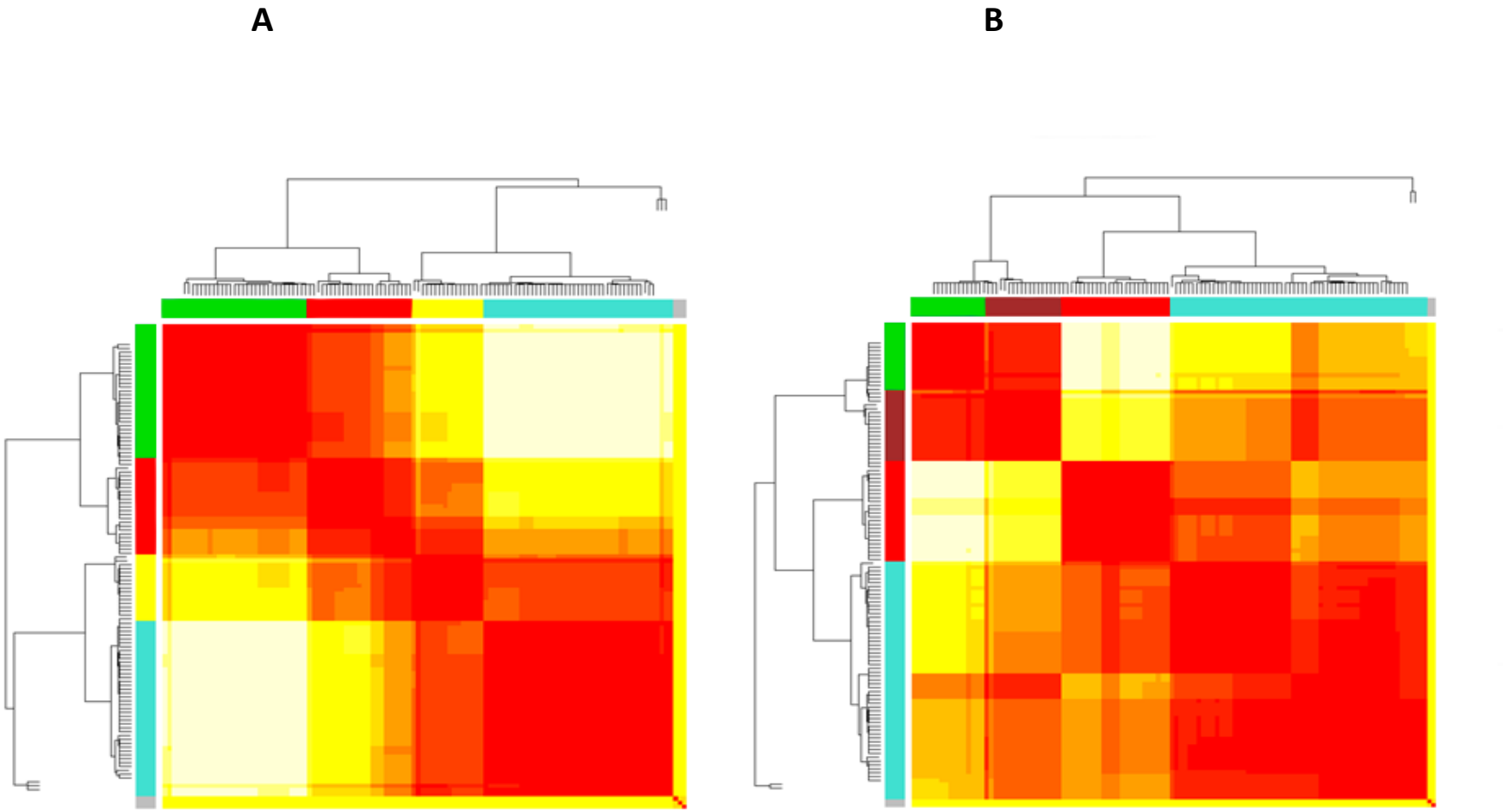

Figure 9 (A), (B). Heatmaps and dendrograms of brain areas clustering calculation. Hierarchical subdivision of brain areas and clustering for both bvFTD and HCs are shown on the left (A) and right (B) panel, respectively. A cutting-height on dendrograms have been applied to obtain the same number of clusters for both groups. We used a cut-off equal to 0.2 to achieve four clusters (yellow-to-red squares within clustering areas). The four clusters are showed as coloured boxes), revealing a clearer subdivision in the bvFTD group (A) respect to HCs (B). Figure published in Saba et al., 2019

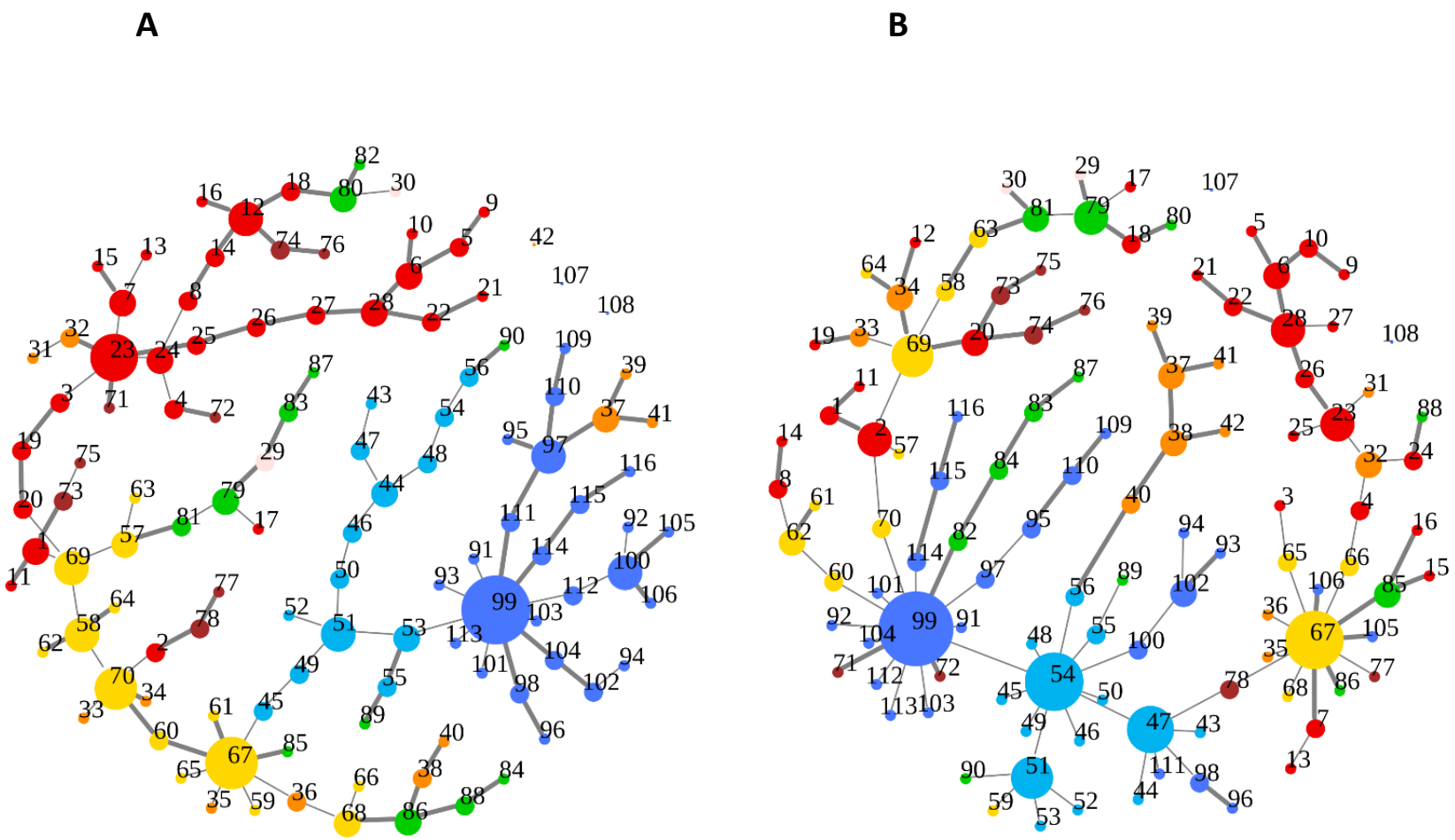

Figure 10 (A), (B). Node degree centrality and superhighways in brain macro-regions. Minimum spanning trees MSTs for both bvFTD and HCs are shown on the left (A) and right (B) panel, respectively. Superhighway paths are highlighted by thick edges and node size is proportional to degree centrality. Macro-regions (i.e., lobes) are identified by node colours, while the node number correspond to AAL 116 region identifier. Identifiers and corresponding areas and macro-regions can be found in Table 5 Macro-region colour code: Red = Frontal; Green = Temporal; Yellow = Parietal; Orange = Limbic; Cyan = Occipital; Brown = Subcortical Gray Matter; Light pink = Insula; Blue = Cerebellum. Figure published in Saba et al., 2019.

Network complexity reduction from HC to bvFTD is evident from bvFTD hierarchical clustering in **Figure 9** (A), where Frontal and Temporal areas (green and red clusters, respectively) are almost completely separated from Parietal (yellow cluster) and Occipital-Cerebellar regions (cyan cluster). On the other hand, HC heatmap in **Figure 9** (B), shows two highly connected network communities (green-brown and red-cyan clusters). Specifically, two different groups of Frontal-Parietal regions (brown and red clusters) are highly connected to Frontal (green cluster) and Temporal-Occipital-Cerebellar regions (cyan cluster), respectively. Notably, network star nodes (i.e., Lingual-L, Occipital-Inf-R, Precuneus-L, and Cerebellum-6-L) traverse and integrate these two highly connected communities in HC (**Figure 10** (B)). Conversely, bvFTD clusters are much more homogeneous (i.e., areas from the same lobe tend to cluster together), involving fewer and isolated stars. This is evident in **Figure 10**, where the bvFTD network (panel (A)) shows a clear lobe segregation (i.e., node colour), especially for Frontal (red), Parietal (yellow), Occipital (light blue), and Cerebellum (blue) lobes, while the HC network (panel (B)) shows a much higher level of integration.

The survival ratio (i.e., the intersection between graphs calculated as the fraction of links found common in two MSTs) was equal to 42%, defining dissimilar topological structures of MSTs in the two groups. These differences are highlighted in **Figure 11,** where edges present in the bvFTD graph but not in the HC one (panel (A)), and vice versa (panel (B)), are shown. More specifically, highly connected star-clusters seen in the HC group were absent in the bvFTD graph. Conversely, leaves and short linear structures seen in the bvFTD group were absent in the HC graph.

Nodes and edges in the axial orientation (x-y)-coordinates of the anatomical automatic labeling (AAL 116) brain atlas are shown in **Figure 12** (A), (B), providing a complete frontotemporal brain state representation, through the visualization of type, number, and origin of connections, confirming the abnormalities found in bvFTD, compared to HC. The most evident feature is a massive grouping of Frontal areas (red nodes in **Figure 12** (A)), disconnected from both Temporal lobes (green nodes in **Figure 12** (A)) and other areas (yellow nodes in **Figure 12** (A)), including the conserved star nodes Precuneus-L and Cerebellum-6-L (nodes #67 and #99 in **Figure 12** (A)).

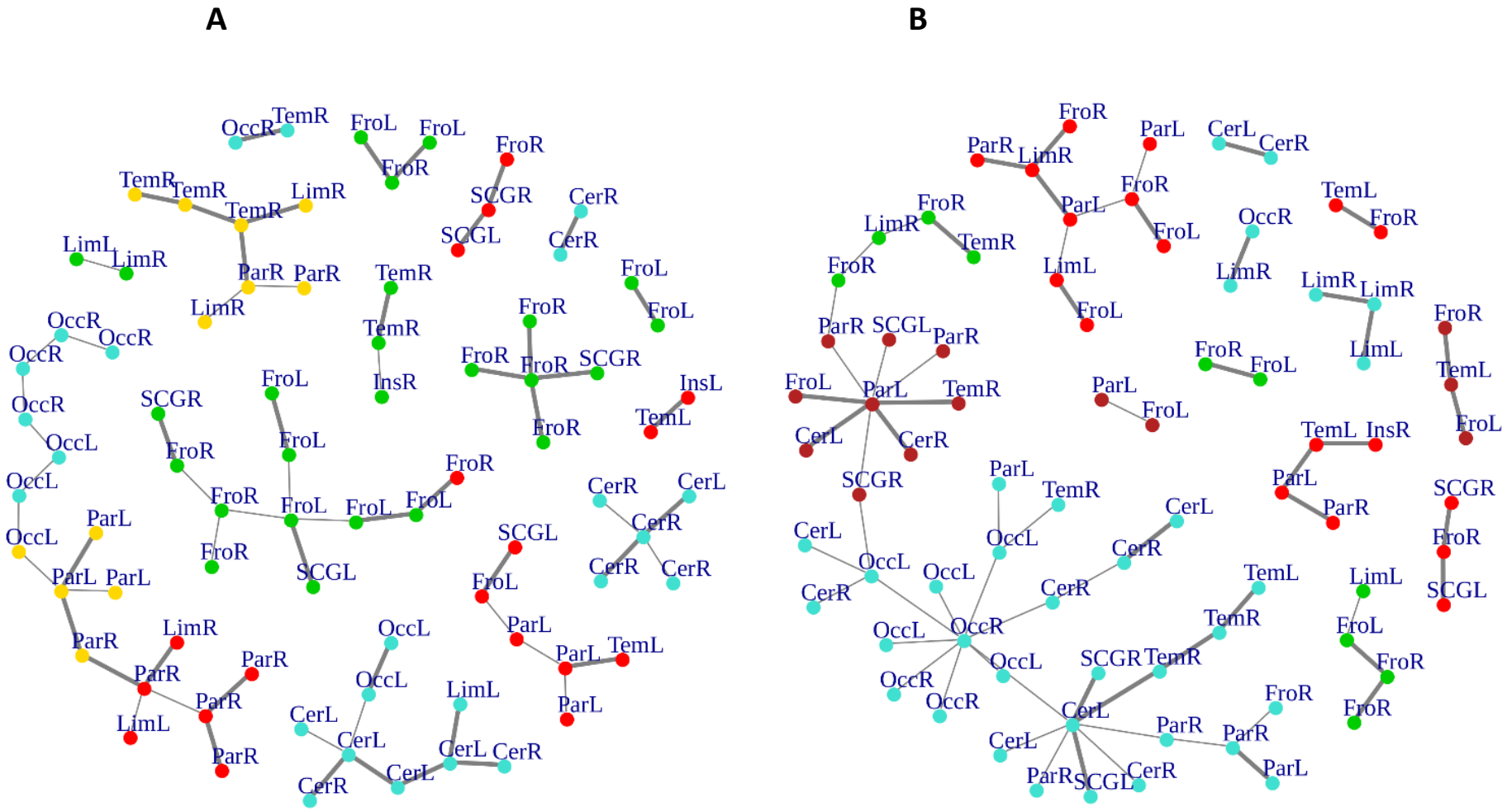

Figure 11 (A), (B). Graph-edges differences between the two groups. MSTs differences for both groups are shown. Left (A) panel shows bvFTD-HC residual graph, while right (B) panel reports the difference HC-bvFTD. Node colours follow cluster membership, as in Figure 8. Node labels indentify macro-regions membership (see Table 5 for label encodings). Figure published in Saba et al., 2019.

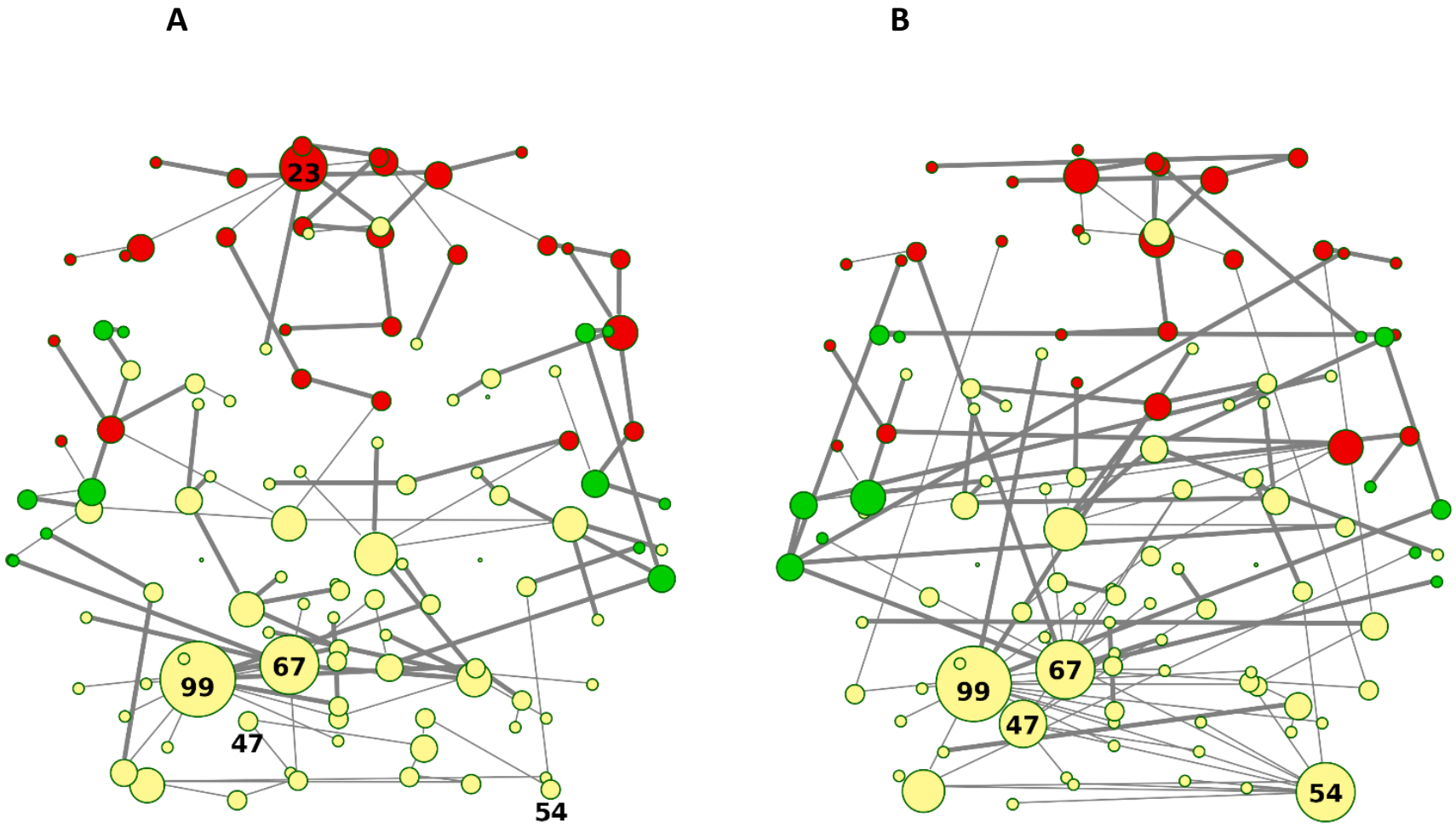

Figure 12 (A), (B). Brain areas spatial location in x-y AAL 116 coordinates with superhighway routes. MSTs for both bvFTD and HCs are shown on the left (A) and right (B) panel, respectively. Red nodes indicate Frontal areas, while Temporal areas are coloured in green. Superhighway paths are highlighted by thick edges and node size is proportional to degree centrality, whose hubs (i.e., nodes having degree centrality > 5) are labelled by AAL 116 region identifier. Left MST (A) reports conserved hubs (areas #67 and #99), lost hubs (areas #47 and #54), and the gained frontal hub (area #23) in bvFTD, respect to HCs. Figure published in Saba et al., 2019.

Strikingly, the massive frontal aggregation in bvFTD belongs entirely to a single cluster (red nodes in **Figure 10** (A) and **Figure 12** (A)), at the centre of which is present a new bvFTD-specific star node (Frontal Sup-Medial-L, node #23 in **Figure 10** (A) and **Figure 12** (A)), indicative of a new isolated functional macro-region in bvFTD. Notably, comparing superhighways distribution between groups (**Figure 12** (A), (B)), HCs show a deeply intertwined connectivity that integrates star nodes with Frontal and Temporal areas, linking them each other. Conversely, bvFTD superhighway connectivity collapses around conserved hubs and within the Frontal macro-region, causing their isolation.

6. 4. Methodological comparison

MST network metrics were compared to other classical graph theory approaches (see Materials and methods, paragraph 5.8), to assess network properties reproducibility and wavelet scale specificity. Network metrics and Wilcoxon rank sum test results are reported in **Table 6** and from **Table 1A** to **Table 4A**. Beside the MST, only the efficiency/cost trade-off-based method (i.e., ECO) showed significant bvFTD/HC separation specifically at scale 2, while all the other scales were non-informative (i.e., non-significant bvFTD/HC differences; **Table 1A**). The EBIC-based method reported few significant indices not directly related to information exchange efficiency (i.e., maximum degree, degree divergence, and assortativity), for both scales 1 and 2, indicating poor discriminant power (**Table 2A**). Lastly, spectral analysis (**Table 3A**) and scale free (**Table 4A**) model-based methods did not show significant case/control differences at any wavelet scale. Notably, both MST and ECO are based on the optimization of the information flow exchange across the functional network, maximizing graph integration and minimizing wiring costs. Common metrics between MST and ECO showing significant results at scale 2 were the same in both methods. However, differently from MST, ECO yielded several disconnected nodes (up to 74) per subject.

7. Discussion

In the present study, we evaluated the power of MST representation within the framework of bvFTD, combining rs-fMRI data and graph theory analysis. Different neuroimaging methods have been proposed to highlight brain damage in bvFTD (Rohrer et al., 2015; Whitwell et al., 2011). However, since the description of the BOLD signal (Ogawa et al., 1990), functional neuroimaging allowed to go beyond the mere anatomical description of brain connectivity, identifying functionally-connected (i.e., synchronised time-dependent fluctuations of the BOLD signal) networks of cortical and subcortical regions (Seeley et al., 2008). In bvFTD, multiple independent studies identified the frontal brain regions as the affected core networks (Lee et al., 2014; Farb et al., 2013; Borroni et al., 2012; Whitwell et al., 2011; Zhou et al., 2010; Seeley et al., 2009).

Graph theory has already been applied in a few MRI studies on bvFTD, demonstrating disruption of the global topologic organization, increased path length and assortativity, with loss of cortical hubs and network centrality, in addition to default brain activity alterations, extending the list of sensible target regions to salience and executive functions (Hohenfeld et al., 2018; Sedeño et al., 2016; Trojsi et al., 2015; Agosta et al., 2013). Despite the wide use of graph theory in the analysis of neurodegenerative disorders, many methodological aspects are left to the experimenter choice, leading to possible confounding results.

When comparing graphs with the same number of nodes (N) and edges (N-1), the MST is an unambiguous method for brain network analysis, allowing to avoid methodological biases (Tewarie et al., 2015). Although it does not completely replace traditional graph theory approaches, MST remains the simplest and most effective representation of a full graph (Stam et al., 2014), where minimum weight (i.e. maximum connectivity) links constitute significant information flow paths. Moreover, it has been recently demonstrated how MST provides robust network estimates, with results in accordance to classical network analytical data (Otte et al., 2015; Tewarie et al., 2015). As indicated by our methodological comparison (see Results, paragraph 6.4), algorithms based on information flow optimization and wiring cost minimization (including MST and ECO methods) achieved the best bvFTD/HC separation performances (**Table 6** and **Table 1A**). On the other hand, fixed-correlation threshold and scale free model-based graphs showed poor or non-significant results, indicating that enforcing an

arbitrary correlation threshold or network nature (i.e., scale free power law distribution) strongly limit network descriptive power. Conversely, MST has the advantage of requiring no correlation thresholds, network density or *a priori* distribution, ensuring full reproducibility and robustness in different conditions. Furthermore, since our results indicated a strong disorder limit tendency in both groups, the MST was able to preserve the connectivity features of the underlying functional networks (Tewarie et al., 2014). Through our TOM-adjusted edge weights, MSTs and relative parameters conserved their neighbourhood node characteristics, highlighting nodes aggregation (i.e. star-type configurations), and providing a valid method to identify a set of shortest paths in MSTs that may be considered as the "critical backbone" of original graph (Tewarie et al., 2014). Our MSTs suggest that the differences between groups may be attributed to functional alterations of such major organization, since they represent the information-flow highways of the fully connected network. Shape-linear configuration tendency in bvFTD graphs (see paragraph 6.2) highlights different impairments: high distance between nodes, low centrality parameter values, and a low exchange information capacity (i.e., low network integration). Connection efficiency loss is particularly evident in **Figure 10**, where the superhighway system in HCs, linking hubs to Frontal and Temporal brain areas, is replaced by a local (i.e., isolated) network surrounding conserved hubs. Functional isolation is a generalized process in bvFTD, where brain areas tend to interact within lobes (i.e., colours in **Figure 10**), showing a homogeneous brain area distribution, longer distances between hubs, and longer within-lobe superhighways. Therefore, bvFTD functional breakdown is not merely described by connectivity loss, but though disease-specific reorganizations and regularization of the information flow. This contrasts with the marked integration of a healthy functional network, where superhighways serve as shortcuts to connect areas from different brain macro-regions. Network regularization has already been observed as a distinctive FTD trait, respect to other neurodegenerative disorders, including Alzheimer's disease (Zhou et al., 2010; de Haan et al., 2009).

We further investigated this aspect by gathering evidences from both global and local network metrics. Although global functional parameters (i.e., strength, diversity, and zero correlation) showed a significantly weaker and reduced connectivity in bvFTD, edge-level and node-level features (i.e., superhighways, and node degree and betweenness centrality), highlighted a more complex scenario, explaining some of the key dysfunctions observed in large scale

resting-state functional networks, including the default-mode (DMN), salience (SN), and executive (EN) networks (Hohenfeld et al., 2018; Sedeño et al. 2016; Trojsi et al., 2015; Irish et al. 2012; Zhou et al., 2010). The first evidence from our data is the formation of a new FTD-specific hub (area #23: Frontal_Sup_Medial_L, **Figure 10** (A)), absent in HCs. This hub is the starting point of a huge superhighway, fully extending within frontal lobe, clearly derived from an elongation of the original route in HCs (**Figure 10** (B)). Specifically, our data showed the involvement of regions: Frontal_Sup_Medial_L/R, Frontal_Sup_Orb_L/R, Frontal_Mid_Orb_L/R, Frontal_Med_Orb_L/R, Rectus_L/R, and Olfactory_L/R (areas #23, #24, #5, #6, #9, #10, #25, #26, #27, #28, #21 and #22 in **Table 5** and **Figure 10** (A)). Notably, all the elements of this superhighway are part of the DMN (Hohenfeld et al., 2018; Trojsi et al., 2015; Zhou et al., 2010), strongly supporting the evidence of a compensation mechanism and frontal DMN decreased connectivity with areas from other lobes. However, this process is not exclusive of the Frontal lobe. Within-lobe superhighway formation, and consequent isolation, involves also the two conserved nodes in bvFTD: Precuneus_L (area #67, parietal lobe in yellow in **Figure 10** (A)) and Cerebellum_6_L (area #99, blue in **Figure 10** (A)), where the former plays a key role in the DMN network. Betweenness difference (*b*) is a good local indicator of these impairments at node level (threshold set at $b = \pm 435$, see paragraph 5.7 and **Table 5A**). Notably, while areas #23 and #67 show a strongly increased node betweenness ($b_{23} = 1545$, and $b_{67} = 879$) from bvFTD to HCs, area #99 loses a great portion of its centrality ($b_{99} = -1534$), supporting the evidence of a functional deterioration of the cerebellar lobule VI, that has been associated with cerebellar atrophy in both bvFTD and Alzheimer's disease (Schmahmann 2016; Guo et al., 2016). Nevertheless, area #99 is the center of an enlarged intra-cerebellar superhighway system, showing that superhighway elongation is due to a generalized network centrality reorganization, rather than a region-specific impairment. It has been recently suggested that long-distance connections have an important role in integrating distinct brain areas, leading to a greater functional diversification, robustness, and specialization (Betzel and Bassett, 2018). However, long-range connections number and length is strictly controlled by their metabolic demand. In contrast, bvFTD long within-lobe superhighways seem not to contribute to the overall functional integration, but rather being the result of a compensatory mechanism, in response to a generalized functional deterioration. To verify this hypothesis, we focused our attention to those areas showing a strong betweenness centrality loss ($b < -435$) in bvFTD respect to HCs. The clearest example in

our data is given by three connected areas (**Figure 10** (B)): Angular_R (area #66, b_{66} = -1552), Frontal_Sup_R (area #4, b_4 = -1359), and Cingulum_Ant_R (area #32, b_{32} = -1299), being involved in DMN, EN, and EN/SN, respectively. As shown in **Figure 10** (B), these three areas connect the Precuneus_L (parietal area #67) and its superhighway system to the frontal superhighway starting from area #23 (Frontal_Sup_Medial_L), that in bvFTD is markedly enlarged (**Figure 10** (A)). In the bvFTD network, area #23 is a new hub, and the #23-67 connection is now a much longer and linear path, suggesting that superhighway elongation could be a compensatory reaction to a less efficient network integration. Notably, Cingulum_Ant_R (area #32) is part of the limbic system, involved in both DMN and salience/executive functions, suggesting that limbic system failure could be an underlying cause of the global network rearrangement observed in bvFTD subjects.

A further support to this hypothesis is represented by the disruption of two HC network hubs (**Figure 10** (B)): Occipital_Inf_R (area #54, b_{54} = -4054) and Lingual_L (area #47, b_{47} = -2913), replaced by a long linear-shaped sequence of occipital areas (**Figure 10** (A)), denouncing a massive loss of degree and betweenness centrality also in this part of the network. Beside hubs, two adjacent connector areas experienced huge loss of betweenness: Fusiform_R (area #56, b_{56} = -531) and ParaHippocampal_R (area #40, b_{40} = -540). Strikingly, while the former is a direct bridge to the hub group, the latter is the first node of a limbic superhighway (**Figure 10** (B)), whose nodes occupy distinct peripheral positions in bvFTD (**Figure 10** (A)), including: Hippocampus_L/R (area #37-38), ParaHippocampal_L/R (areas #39-40), and Amygdala_L/R (areas #41-42). Due to bvFTD mudules isolation respect to HCs, there is a connection loss associated to several limbic areas. Starting from ParaHippocampal_R area (the most damaged), another important loss of betweenness result in Hippocampus_R (area #38, b38 = -328), in addition to less considerable values in Hippocampus_L and ParaHippocampal_L (areas #37-39). Consistent with DMN literature in Frontotemporal Dementia (Irish et al., 2012), some memory, emotional and motivational alterations in bvFTD derived from early atrophy in these areas, involving often limbic regions in self-projective cognitive process changes, such as autobiographical memory.

As explained in detail above, the trade-off between costs and functional integration of brain macro-areas constitutes a key point of this work. Network efficiency needs a strong functional integration between regions with different roles, as well as it requests a higher metabolic

demand, often responsible of ROS production, dangerous for brain degenerative process activation and its development (Palluzzi et al., 2017). Tree based-functional structure better represents this equilibrium, favouring distance minimization with higher information-flow, strongly able to highlight case/control differences. Indeed, efficient superhighways ramified through different macro-regions, contrast with linear, elongated, sometimes short and fragmented, intra-modules superhighways in bvFTD network, further highlighted by hubs betweenness loss.

In the light of these evidences, our hypothesis based on frontal and temporal degeneration as cause of a functional breakdown and reduced functional connections of the other brain areas. As already introduced, long within-lobe superhighways appear as a result of a compensatory mechanism, in response to a generalized pathological deterioration. In fact, these alternative linear links are less efficient, probably characterized by a higher energetic demand that itself foments the disease progression. Therefore, from our results, the effects on functional connectivity do not limited to frontal and temporal areas but also involve other cortical and subcortical areas, including Hippocampal and Parahippocampal areas and Amygdala. Therefore, we suggest an underlying involvement of the limbic system in the observed bvFTD functional deterioration, associated to the well-studied impairments affecting emotion recognition, social inference, and executive functions typical of this neurodegenerative disorder (Hohenfeld et al., 2018; Sedeño et al. 2016; Trojsi et al., 2015; Zhou et al., 2010).

8. Conclusion

The present work had the primary goal of highlighting alterations in brain connectivity of bvFTD subjects, providing at the same time a detailed description of the observed functional impairments, and insights about their possible causes. According to the most recent fMRI literature (Cui et al., 2018; Guo et al., 2017), we applied an MST model to wavelet correlation matrices from bvFTD and HC subjects, exploiting three strongpoints of MST-based methods: (i) assumption-free network construction and reproducibility, (ii) independence from node and edge number during network comparison, and (iii) simplicity of representation (i.e., three branching is directly interpretable in terms of most efficient shortest paths). On the other hand, MSTs have one main limitation: the resulting network is a sparse representation, implicitly excluding triangular connections, thus causing non-applicability of some common clustering metrics (e.g., transitivity and coreness) and evaluation of the network small-worldness. However, we coped with this issue by using topological overlap measures (Zhang and Horvath, 2005) and the extreme value index evaluation (Van Mieghem and Magdalena, 2005).

The combination of this theoretical model with rs-fMRI data allowed us not only to generate a clear picture of the functional divergence of bvFTD from HCs, but also to shed light on the possible causes of topological and functional rearrangements, and compensatory mechanisms, underlying cognitive, social, and executive impairments characterizing bvFTD phenotype. About that, Limbic system offers interesting suggestions concern integration lack between behavior and executive functions in bvFTD pathology.

Further developments to the present work, that now constitute main limitations, are represented by: (i) the lack of clinical and/or metabolic parameters that could confirm or reveal new causal hypotheses, and (ii) a combination with anatomical variables (e.g., grey matter mass), to achieve a better model resolution, and associate degenerative processes to functional deterioration.

Collectively, the application of MST-based analysis to rs-fMRI data looks a promising way to clarify the role of degenerative processes involved in FTD functional breakdown, improving the discovery of new fMRI biomarkers.

9. References

Achard, S. (2015). Basic wavelet analysis of multivariate time series with a visualisation and parametrisation using graph theory. CRAN repository. URL: https://cran.r-project.org/web/packages/brainwaver/brainwaver.pdf

Achard, S., and Bullmore, E. (2007). Efficiency and Cost of Economical Brain Functional Networks. *PLOS Computational Biology* 3, e17. doi:10.1371/journal.pcbi.0030017

Achard, S., Salvador, R., Whitcher, B., Suckling, J., Bullmore, E. (2006). A resilient, low-frequency, small-world human brain functional network with highly connected association cortical hubs. *J Neurosci*. 26, 63-72. https://doi.org/10.1523/JNEUROSCI.3874-05.2006

Agosta, F., Sala, S., Valsasina, P., Meani, A., Canu, E., Magnani, G., et al. (2013). Brain network connectivity assessed using graph theory in frontotemporal dementia. *Neurology* 81, 134–143. doi:10.1212/WNL.0b013e31829a33f8

Albert, R., Barabási, A. L. (2002). Statistical mechanics of complex networks. Statistical mechanics of complex networks. *Rev Mod Phys.* 74, 47-97. https://doi.org/10.1103/RevModPhys.74.47

Antonenko, D., Külzow, N., Sousa, A., Prehn, K., Grittner, U., and Flöel, A. (2018). Neuronal and behavioral effects of multi-day brain stimulation and memory training. *Neurobiol. Aging* 61, 245–254. doi:10.1016/j.neurobiolaging.2017.09.017

Barabasi, A.L., Albert, R. (1999). Emergence of scaling in random networks. *Science* 286, 509–512. doi: 10.1126/science.286.5439.509

Barbey, A. K. (2018). Network Neuroscience Theory of Human Intelligence. *Trends Cogn. Sci. (Regul. Ed.)* 22, 8–20. doi:10.1016/j.tics.2017.10.001

Barbey, A. K., Belli, A., Logan, A., Rubin, R., Zamroziewicz, M., and Operskalski, J. T. (2015). Network topology and dynamics in traumatic brain injury. *Current Opinion in Behavioral Sciences* 4, 92–102. doi:10.1016/j.cobeha.2015.04.002

Betzel, R. F., and Bassett, D. S. (2018). Specificity and robustness of long-distance connections in weighted, interareal connectomes. *PNAS* 115, E4880–E4889. doi:10.1073/pnas.1720186115

Borate, B. R., Chesler, E. J., Langston, M. A., Saxton, A. M., and Voy, B. H. (2009). Comparison of threshold selection methods for microarray gene co-expression matrices. *BMC Res Notes* 2, 240. doi:10.1186/1756-0500-2-240

Borroni, B., Alberici, A., Cercignani, M., Premi, E., Serra, L., Cerini, C., et al. (2012). Granulin mutation drives brain damage and reorganization from preclinical to symptomatic FTLD. *Neurobiol. Aging* 33, 2506–2520. doi:10.1016/j.neurobiolaging.2011.10.031

Borroni, B., Alberici, A., Premi, E., Archetti, S., Garibotto, V., Agosti, C., et al. (2008). Brain Magnetic Resonance Imaging Structural Changes in a Pedigree of Asymptomatic Progranulin Mutation Carriers. *Rejuvenation Research* 11, 585–595. doi: 10.1089/rej.2007.0623

Braunstein, L. A., Wu, Z., Chen, Y., Buldyrev, S. V., Kalisky, T., Sreenivasan, S., et al. (2007). Optimal path and minimal spanning trees in random weighted networks. *Int. J. Bifurcation Chaos* 17, 2215–2255. doi: 10.1142/S0218127407018361

Brett, M., Anton, J.-L., Valabregue, R., and Poline, J.-B. (2002). Region of Interest Analysis Using an SPM Toolbox [Abstract]. *Neuroimage* 16. doi:10.1016/S1053-8119(02)90013-3

Bullmore, E., Fadili, J., Maxim, V., Sendur, L., Whitcher, B., Suckling, J., et al. (2004). Wavelets and functional magnetic resonance imaging of the human brain. *Neuroimage* 23 Suppl 1, S234-249. doi: 10.1016/j.neuroimage.2004.07.012

Bullmore, E., and Sporns, O. (2009). Complex brain networks: graph theoretical analysis of structural and functional systems. *Nat. Rev. Neurosci.* 10, 186–198. doi: 10.1038/nrn2575

Bullmore, E., and Sporns, O. (2012). The economy of brain network organization. *Nat. Rev. Neurosci.* 13, 336–349. doi:10.1038/nrn3214

Chavez, M., Valencia, M., Navarro, V., Latora, V., and Martinerie, J. (2010). Functional Modularity of Background Activities in Normal and Epileptic Brain Networks. *Physical Review Letters* 104. doi:10.1103/PhysRevLett.104.118701

Chiang, S., Cassese, A., Guindani, M., Vannucci, M., Yeh, H. J., Haneef, Z., et al. (2016). Time-dependence of graph theory metrics in functional connectivity analysis. *Neuroimage* 125, 601–615. doi:10.1016/j.neuroimage.2015.10.070

Colon-Perez, L. M., Couret, M., Triplett, W., Price, C. C., and Mareci, T. H. (2016). Small Worldness in Dense and Weighted Connectomes. *Front. Phys.* 4. doi:10.3389/fphy.2016.00014

Cormen, T. H., Leiserson, C. E., Rivest, R. L., Stein, C. (2001). Introduction to Algorithms (2nd ed). MIT Press, Cambridge, MA, USA

Cosseddu, M., Benussi, A., Gazzina, S., Turrone, R., Archetti, S., Bonomi, E., et al. (2018). Mendelian forms of disease and age at onset affect survival in frontotemporal dementia. *Amyotrophic Lateral Sclerosis and Frontotemporal Degeneration* 19, 87–92. doi:10.1080/21678421.2017.1384020

Csardi, G., Nepusz, T. (2006). The igraph software package for complex network research. InterJournal, Complex Systems 1695. http://igraph.sf.net/

Cui, X., Xiang, J., Guo, H., Yin, G., Zhang, H., Lan, F., et al. (2018). Classification of Alzheimer's Disease, Mild Cognitive Impairment, and Normal Controls With Subnetwork Selection and Graph Kernel Principal Component Analysis Based on Minimum Spanning Tree Brain Functional Network. *Front Comput Neurosci* 12. doi:10.3389/fncom.2018.00031

De Vico Fallani, F., Latora, V., and Chavez, M. (2017). A Topological Criterion for Filtering Information in Complex Brain Networks. *PLoS Comput Biol* 13. doi: 10.1371/journal.pcbi.1005305

Drakesmith, M., Caeyenberghs, K., Dutt, A., Lewis, G., David, A. S., and Jones, D. K. (2015). Overcoming the effects of false positives and threshold bias in graph theoretical analyses of neuroimaging data. *Neuroimage* 118, 313–333. doi:10.1016/j.neuroimage.2015.05.011

Edwards, D., de Abreu, G. C. G., and Labouriau, R. (2010). Selecting high-dimensional mixed graphical models using minimal AIC or BIC forests. *BMC Bioinformatics* 11, 18. doi: 10.1186/1471-2105-11-18

Erdös, P., Rényi, A. (1960). On the evolution of random graphs. *Publ. Math. Inst. Hung. Acad. Sci*. 5, 17–61. http://snap.stanford.edu/class/cs224w-readings/erdos60random.pdf

Estrada, E. (2015). Graph and Network Theory. In *Mathematical Tools for Physicists*, 2nd edition. John Wiley & Sons, USA

Farahani, F. V., Karwowski, W., and Lighthall, N. R. (2019). Application of Graph Theory for Identifying Connectivity Patterns in Human Brain Networks: A Systematic Review. *Front. Neurosci.* 13. doi: 10.3389/fnins.2019.00585

Farb, N. A. S., Grady, C. L., Strother, S., Tang-Wai, D. F., Masellis, M., Black, S., et al. (2013). Abnormal network connectivity in frontotemporal dementia: evidence for prefrontal isolation. *Cortex* 49, 1856–1873. doi:10.1016/j.cortex.2012.09.008

Fornito, A., Zalesky, A., and Breakspear, M. (2015). The connectomics of brain disorders. *Nature Reviews Neuroscience* 16, 159–172. doi: 10.1038/nrn3901

Foygel, R., and Drton, M. (2010). Extended Bayesian Information Criteria for Gaussian Graphical Models. *arXiv:1011.6640 [math, stat]*. Available at: http://arxiv.org/abs/1011.6640 [Accessed September 10, 2019].

Fraga González, G., Van der Molen, M. J. W., Žarić, G., Bonte, M., Tijms, J., Blomert, L., et al. (2016). Graph analysis of EEG resting state functional networks in dyslexic readers. *Clin Neurophysiol* 127, 3165–3175. doi: 10.1016/j.clinph.2016.06.023

Ghasemi, M., Seidkhani, H., Tamimi, F., Rahgozar, M., Masoudi-Nejad, A. (2014). Centrality Measures in Biological Networks. *Current Bioinf*. 9. doi**:** 10.2174/15748936113086660013

Gordon, E., Rohrer, J. D., and Fox, N. C. (2016). Advances in neuroimaging in frontotemporal dementia. *J. Neurochem.* 138 Suppl 1, 193–210. doi: 10.1111/jnc.13656

Gore, J. C. (2003). Principles and practice of functional MRI of the human brain. *J Clin Invest* 112, 4–9. doi: 10.1172/JCI200319010

Gorno-Tempini, M. L., Hillis, A. E., Weintraub, S., Kertesz, A., Mendez, M., Cappa, S. F. et al. (2011). Classification of primary progressive aphasia and its variants. *Neurology*. 76, 1006–1014. doi: 10.1212/WNL.0b013e31821103e6

Griffanti, L., Dipasquale, O., Laganà, M. M., Nemni, R., Clerici, M., Smith, S. M., et al. (2015). Effective artifact removal in resting state fMRI data improves detection of DMN functional connectivity alteration in Alzheimer's disease. *Front Hum Neurosci* 9, 449. doi: 10.3389/fnhum.2015.00449

Griffanti, L., Salimi-Khorshidi, G., Beckmann, C. F., Auerbach, E. J., Douaud, G., Sexton, C. E., et al. (2014). ICA-based artefact removal and accelerated fMRI acquisition for improved resting state network imaging. *Neuroimage* 95, 232–247. doi: 10.1016/j.neuroimage.2014.03.034

Guo, H., Liu, L., Chen, J., Xu, Y., and Jie, X. (2017). Alzheimer Classification Using a Minimum Spanning Tree of High-Order Functional Network on fMRI Dataset. *Front. Neurosci.* 11. doi:10.3389/fnins.2017.00639

Guo, C. C., Tan, R., Hodges, J. R., Hu, X., Sami, S., and Hornberger, M. (2016). Network-selective vulnerability of the human cerebellum to Alzheimer's disease and frontotemporal dementia. *Brain* 139, 1527–1538. doi:10.1093/brain/aww003

Haass, C., and Neumann, M. (2016). Frontotemporal dementia: from molecular mechanisms to therapy. *Journal of Neurochemistry* 138, 3–5. doi: 10.1111/jnc.13619

He, Y., Wang, J., Wang, L., Chen, Z. J., Yan, C., Yang, H., et al. (2009). Uncovering Intrinsic Modular Organization of Spontaneous Brain Activity in Humans. *PLOS ONE* 4, e5226. doi:10.1371/journal.pone.0005226

Hohenfeld, C., Werner, C. J., and Reetz, K. (2018). Resting-state connectivity in neurodegenerative disorders: Is there potential for an imaging biomarker? *Neuroimage Clin* 18, 849–870. doi: 10.1016/j.nicl.2018.03.013

Irish, M., Piguet, O., Hodges, J.R. (2012). Self-projection and the default network in frontotemporal dementia. *Nat. Rev. Neurol* 8, 152–161. doi: 10.1038/nrneurol.2012.11

Jenkinson, M., Beckmann, C. F., Behrens, T. E. J., Woolrich, M. W., and Smith, S. M. (2012). FSL. *Neuroimage* 62, 782–790. doi: 10.1016/j.neuroimage.2011.09.015

Kaiser, M. (2011). A tutorial in connectome analysis: topological and spatial features of brain networks. *Neuroimage* 57, 892–907. doi: 10.1016/j.neuroimage.2011.05.025

Knösche, T. R., and Tittgemeyer, M. (2011). The Role of Long-Range Connectivity for the Characterization of the Functional–Anatomical Organization of the Cortex. *Frontiers in Systems Neuroscience* 5. doi:10.3389/fnsys.2011.00058.

Langfelder, P., and Horvath, S. (2008). WGCNA: an R package for weighted correlation network analysis. *BMC Bioinformatics* 9, 559. doi: 10.1186/1471-2105-9-559

Laughlin, S. B., and Sejnowski, T. J. (2003). Communication in neuronal networks. *Science* 301, 1870–1874. doi:10.1126/science.1089662

Lee, S. E., Khazenzon, A. M., Trujillo, A. J., Guo, C. C., Yokoyama, J. S., Sha, S. J., et al. (2014). Altered network connectivity in frontotemporal dementia with C9orf72 hexanucleotide repeat expansion. *Brain* 137, 3047–3060. doi:10.1093/brain/awu248

Lee, M. H., Smyser, C. D., and Shimony, J. S. (2013). Resting-state fMRI: a review of methods and clinical applications. *AJNR Am J Neuroradiol* 34, 1866–1872. doi: 10.3174/ajnr. A3263

Liu, M.-N., Lau, C.-I., and Lin, C.-P. (2019). Precision Medicine for Frontotemporal Dementia. *Front. Psychiatry* 10. doi:10.3389/fpsyt.2019.00075

Lynall, M.-E., Bassett, D. S., Kerwin, R., McKenna, P. J., Kitzbichler, M., Muller, U., et al. (2010). Functional connectivity and brain networks in schizophrenia. *J. Neurosci.* 30, 9477–9487. doi:10.1523/JNEUROSCI.0333-10.2010

Mahoney, C. J., Simpson, I. J. A., Nicholas, J. M., Fletcher, P. D., Downey, L. E., Golden, H. L., et al. (2015). Longitudinal Diffusion Tensor Imaging in Frontotemporal Dementia. *Ann Neurol* 77, 33–46. doi: 10.1002/ana.24296

Mann, D. M. A., and Snowden, J. S. (2017). Frontotemporal lobar degeneration: Pathogenesis, pathology and pathways to phenotype. *Brain Pathology* 27, 723–736. doi: 10.1111/bpa.12486

McKeown, M. J., Hansen, L. K., and Sejnowsk, T. J. (2003). Independent component analysis of functional MRI: what is signal and what is noise? *Curr. Opin. Neurobiol.* 13, 620–629

Mears, D., and Pollard, H. B. (2016). Network science and the human brain: Using graph theory to understand the brain and one of its hubs, the amygdala, in health and disease. *J. Neurosci. Res.* 94, 590–605. doi: 10.1002/jnr.23705

Meier, J., Tewarie, P., and Van Mieghem, P. (2015). The Union of Shortest Path Trees of Functional Brain Networks. *Brain Connect* 5, 575–581. doi: 10.1089/brain.2014.0330

Mumford, J. A., Horvath, S., Oldham, M. C., Langfelder, P., Geschwind, D. H., and Poldrack, R. A. (2010). Detecting network modules in fMRI time series: a weighted network analysis approach. *Neuroimage* 52, 1465–1476. doi: 10.1016/j.neuroimage.2010.05.047

Newman, M. E. J. (2003). Mixing patterns in networks. *Physical Review E* 67. https://doi.org/10.1103/PhysRevE.67.026126

Ogawa, S., Lee, T. M., Kay, A. R., and Tank, D. W. (1990). Brain magnetic resonance imaging with contrast dependent on blood oxygenation. *Proc Natl Acad Sci U S A* 87, 9868–9872.

Olney, N. T., Spina, S., and Miller, B. L. (2017). Frontotemporal Dementia. *Neurol Clin* 35, 339–374. doi: 10.1016/j.ncl.2017.01.008

Otte, W. M., van Diessen, E., Paul, S., Ramaswamy, R., Subramanyam Rallabandi, V. P., Stam, C. J., et al. (2015). Aging alterations in whole-brain networks during adulthood mapped with the minimum spanning tree indices: the interplay of density, connectivity cost and life-time trajectory. *Neuroimage* 109, 171–189. doi:10.1016/j.neuroimage.2015.01.011

Palluzzi, F., Ferrari, R., Graziano, F., Novelli, V., Rossi, G., Galimberti, D., et al. (2017). A novel network analysis approach reveals DNA damage, oxidative stress and calcium/cAMP homeostasis-associated biomarkers in frontotemporal dementia. *PLoS ONE* 12. doi:10.1371/journal.pone.0185797.

Papik, K., Molnar, B., Schaefer, R., Dombovari, Z., Tulassay, Z., and Feher, J. Application of neural networks in medicine — a review. 9

Papo, D., Buldú, J. M., Boccaletti, S., and Bullmore, E. T. (2014). Complex network theory and the brain. *Philos. Trans. R. Soc. Lond., B, Biol. Sci.* 369. doi: 10.1098/rstb.2013.0520

Park, H.-J., and Friston, K. (2013). Structural and functional brain networks: from connections to cognition. *Science* 342, 1238411. doi:10.1126/science.1238411

Perkins, A. D., and Langston, M. A. (2009). Threshold selection in gene co-expression networks using spectral graph theory techniques. *BMC Bioinformatics* 10, S4. doi: 10.1186/1471-2105-10-S11-S4

Pievani, M., de Haan, W., Wu, T., Seeley, W. W., and Frisoni, G. B. (2011). Functional network disruption in the degenerative dementias. *Lancet Neurol* 10, 829–843. doi:10.1016/S1474-4422(11)70158-2

Raichle, M. E. (2015). The brain's default mode network. *Annu. Rev. Neurosci.* 38, 433–447. doi:10.1146/annurev-neuro-071013-014030

Raichle, M. E. (2011). The restless brain. *Brain Connect* 1, 3–12. doi:10.1089/brain.2011.0019

Rashid, B., Damaraju, E., Pearlson, G. D., and Calhoun, V. D. (2014). Dynamic connectivity states estimated from resting fMRI Identify differences among Schizophrenia, bipolar disorder, and healthy control subjects. *Front Hum Neurosci* 8. doi:10.3389/fnhum.2014.00897

Ravasz, E., Somera, A. L., Mongru, D. A., Oltvai, Z. N., and Barabási, A. L. (2002). Hierarchical organization of modularity in metabolic networks. *Science* 297, 1551–1555. ravadoi: 10.1126/science.1073374

R Core team (2018). R: A Language and Environment for Statistical Computing. The R Foundation for Statistical Computing. Available online at https://www.r-project.org/

Rohrer, J. D., Nicholas, J. M., Cash, D. M., van Swieten, J., Dopper, E., Jiskoot, L., et al. (2015). Presymptomatic cognitive and neuroanatomical changes in genetic frontotemporal dementia in the Genetic Frontotemporal dementia Initiative (GENFI) study: a cross-sectional analysis. *Lancet Neurol* 14, 253–262. doi:10.1016/S1474-4422(14)70324-2

Rubinov, M., and Sporns, O. (2010). Complex network measures of brain connectivity: Uses and interpretations. *NeuroImage* 52, 1059–1069. doi: 10.1016/j.neuroimage.2009.10.003

Rutter, L., Nadar, S. R., Holroyd, T., Carver, F. W., Apud, J., Weinberger, D. R., et al. (2013). Graph theoretical analysis of resting magnetoencephalographic functional connectivity networks. *Front. Comput. Neurosci.* 7. doi: 10.3389/fncom.2013.00093

Saba, V., Premi, E., Cristillo, V., Gazzina, S., Palluzzi, F., Zanetti, O., et al. (2019). Brain Connectivity and Information-Flow Breakdown Revealed by a Minimum Spanning Tree-Based Analysis of MRI Data in Behavioral Variant Frontotemporal Dementia. *Front. Neurosci.* 13. doi: 10.3389/fnins.2019.00211

Salvador, R., Suckling, J., Coleman, M. R., Pickard, J. D., Menon, D., and Bullmore, E. (2005). Neurophysiological Architecture of Functional Magnetic Resonance Images of Human Brain. *Cerebral Cortex* 15, 1332–1342. doi: 10.1093/cercor/bhi016

Sedeño, L., Couto, B., García-Cordero, I., Melloni, M., Baez, S., Morales Sepúlveda, J. P., et al. (2016). Brain Network Organization and Social Executive Performance in Frontotemporal

Dementia. *Journal of the International Neuropsychological Society* 22, 250–262. doi:10.1017/S1355617715000703

Seeley, W. W., Crawford, R., Rascovsky, K., Kramer, J. H., Weiner, M., Miller, B. L., et al. (2008). Frontal paralimbic network atrophy in very mild behavioral variant frontotemporal dementia. *Arch. Neurol.* 65, 249–255. doi:10.1001/archneurol.2007.38

Seeley, W. W., Crawford, R. K., Zhou, J., Miller, B. L., and Greicius, M. D. (2009). Neurodegenerative diseases target large-scale human brain networks. *Neuron* 62, 42–52. doi:10.1016/j.neuron.2009.03.024

Schmahmann, J. D. (2016). Cerebellum in Alzheimer's disease and frontotemporal dementia: not a silent bystander. *Brain* 139, 1314–1318. doi:10.1093/brain/aww064

Sporns, O. (2011). Networks of the Brain. The MIT Press – Cambridge, Massachusetts – London, England

Stam, C. J, Tewarie, P., Van Dellen, E., van Straaten, E. C. W., Hillebrand, A., Van Mieghem, P. (2014). The trees and the forest: Characterization of complex brain networks with minimum spanning trees. *Int J Psychophysiol.* 92, 129–138

Telesford, Q. K., Joyce, K. E., Hayasaka, S., Burdette, J. H., and Laurienti, P. J. (2011). The Ubiquity of Small-World Networks. *Brain Connect* 1, 367–375. doi:10.1089/brain.2011.0038

Tewarie, P., Hillebrand, A., Schoonheim, M. M., van Dijk, B. W., Geurts, J. J. G., Barkhof, F., et al. (2014). Functional brain network analysis using minimum spanning trees in Multiple Sclerosis: an MEG source-space study. *Neuroimage* 88, 308–318. doi:10.1016/j.neuroimage.2013.10.022

Tewarie, P., van Dellen, E., Hillebrand, A., and Stam, C. J. (2015). The minimum spanning tree: an unbiased method for brain network analysis. *Neuroimage* 104, 177–188. doi:10.1016/j.neuroimage.2014.10.015

Trojsi, F., Esposito, F., de Stefano, M., Buonanno, D., Conforti, F. L., Corbo, D., et al. (2015). Functional overlap and divergence between ALS and bvFTD. *Neurobiol. Aging* 36, 413–423. doi: 10.1016/j.neurobiolaging.2014.06.025

Tzourio-Mazoyer, N., Landeau, B., Papathanassiou, D., Crivello, F., Etard, O., Delcroix, N., et al. (2002). Automated anatomical labeling of activations in SPM using a macroscopic anatomical parcellation of the MNI MRI single-subject brain. *Neuroimage* 15, 273–289. doi:10.1006/nimg.2001.0978

van den Heuvel, M. P., Stam, C. J., Boersma, M., and Hulshoff Pol, H. E. (2008). Small-world and scale-free organization of voxel-based resting-state functional connectivity in the human brain. *Neuroimage* 43, 528–539. doi:10.1016/j.neuroimage.2008.08.010

van Lutterveld, R., van Dellen, E., Pal, P., Yang, H., Stam C. J., Brewer, J. (2017). Meditation is associated with increased brain network integration. *Neuroimage.* 158, 18–25. https://doi.org/10.1016/j.neuroimage.2017.06.071

Van Mieghem, P., Magdalena, S. M. (2005). Phase transition in the link weight structure of networks. *Phys Rev E Stat Nonlin Soft Matter Phys.* 72, 056138. https://doi.org/10.1103/PhysRevE.72.056138

Van Mieghem, P., van Langen, S. (2005). Influence of the link weight structure on the shortest path. *Phys Rev E Stat Nonlin Soft Matter Phys.* 71, 056113. https://doi.org/10.1103/PhysRevE.71.056113

Wang, F. X., and Chen, G. (2003). Complex Networks: Small-World, Scale-Free and Beyond. *IEEE circuits and systems magaz.* 3, 6-20. doi: 10.1109/MCAS.2003.1228503

Watson C. G. (2018). Graph Theory Analysis of Brain MRI Data. CRAN repository. URL: https://github.com/cwatson/brainGraph

Watts, D.J., and Strogatz, S.H. (1998). Collective dynamics of 'small-world' networks. *Nature*. 393, 440–442. https://doi.org/10.1038/30918

Whitwell, J. L., Josephs, K. A., Avula, R., Tosakulwong, N., Weigand, S. D., Senjem, M. L., et al. (2011). Altered functional connectivity in asymptomatic MAPT subjects: a comparison to bvFTD. *Neurology* 77, 866–874. doi:10.1212/WNL.0b013e31822c61f2

Whitwell, J. L., Weigand, S. D., Boeve, B. F., Senjem, M. L., Gunter, J. L., DeJesus-Hernandez, M., et al. (2012). Neuroimaging signatures of frontotemporal dementia genetics: C9ORF72, tau, progranulin and sporadics. *Brain* 135, 794–806. doi: 10.1093/brain/aws001

Wijk, B. C. M. van, Stam, C. J., and Daffertshofer, A. (2010). Comparing Brain Networks of Different Size and Connectivity Density Using Graph Theory. *PLOS ONE* 5, e13701. doi:10.1371/journal.pone.0013701

Woollacott, I. O. C., and Rohrer, J. D. (2016). The clinical spectrum of sporadic and familial forms of frontotemporal dementia. *Journal of Neurochemistry* 138, 6–31. doi: 10.1111/jnc.13654

Wu, Z., Braunstein, L. A., Havlin, S., and Stanley, H. E. (2006). Transport in Weighted Networks: Partition into Superhighways and Roads. *Phys. Rev. Lett.* 96, 148702. doi:10.1103/PhysRevLett.96.148702

Young, J. J., Lavakumar, M., Tampi, D., Balachandran, S., and Tampi, R. R. (2018). Frontotemporal dementia: latest evidence and clinical implications. *Ther Adv Psychopharmacol* 8, 33–48. doi:10.1177/2045125317739818

Yu, M., Gouw, A. A., Hillebrand, A., Tijms, B. M., Stam, C. J., van Straaten, E. C. W., et al. (2016). Different functional connectivity and network topology in behavioral variant of frontotemporal dementia and Alzheimer's disease: an EEG study. *Neurobiol. Aging* 42, 150–162. doi:10.1016/j.neurobiolaging.2016.03.018

Yu, M., Hillebrand, A., Tewarie, P., Meier, J., van Dijk, B., Van Mieghem, P., et al. (2015). Hierarchical clustering in minimum spanning trees. *Chaos* 25, 023107. doi: 10.1063/1.4908014

Zalesky, A., Fornito, A., and Bullmore, E. (2012). On the use of correlation as a measure of network connectivity. *Neuroimage* 60, 2096–2106. doi: 10.1016/j.neuroimage.2012.02.001

Zhang, B., and Horvath, S. (2005). A general framework for weighted gene co-expression network analysis. *Stat Appl Genet Mol Biol* 4, Article17. doi: 10.2202/1544-6115.1128

Zhang, Z., Telesford, Q. K., Giusti, C., Lim, K. O., and Bassett, D. S. (2016). Choosing Wavelet Methods, Filters, and Lengths for Functional Brain Network Construction. *PLOS ONE* 11, e0157243. doi: 10.1371/journal.pone.0157243

Zhao, T., Liu, H., Roeder, K., Lafferty, J., and Wasserman, L. (2012). The huge Package for High-dimensional Undirected Graph Estimation in R. *J Mach Learn Res* 13, 1059–1062

Zhou, J., Greicius, M. D., Gennatas, E. D., Growdon, M. E., Jang, J. Y., Rabinovici, G. D., et al. (2010). Divergent network connectivity changes in behavioural variant frontotemporal dementia and Alzheimer's disease. *Brain* 133, 1352–1367. doi:10.1093/brain/awq075

10. Appendix

Table 1A. Wilcoxon rank sum tests using Efficiency Cost Optimization (ECO)-based global connectivity parameters at every scale.

Table 2A. Wilcoxon rank sum tests using Extended Bayesian Information Criterion (EBIC)-based global connectivity parameters at every scale.

Table 3A. Wilcoxon rank sum tests using spectral analysis-derived global connectivity parameters at every scale.

Table 4A. Wilcoxon rank sum tests using scale free model-based global connectivity parameters at every scale.

Table 5A. Betweenness and degree centrality in bvFTD versus HCs.

Graph theory applied to neuroimaging data reveal key functional connectivity alterations in brain ofbehavioral variant Frontotemporal Dementia subjects

Table 1A. Wilcoxon rank sum tests using Efficiency Cost Optimization (ECO)-based global connectivity parameters at every scale. Wilcoxon rank sum tests in bvFTD subjects versus healthy controls HCs are shown in the table. The networks from which global parameters are extracted, are built using a fixed edge density that optimizes efficiency and wiring costs. Tests estimate differences (Estimate column) are calculated for each scale (1 to 4), for every global connectivity parameter. Estimates are adjusted for age, sex, and age*sex interaction. Strength, diversity, and rzero are directly derived from the correlation matrix, while the other metrics refer to the resulting networks.

	Estimate	Lower CI95%	Upper CI95%	P-value	Adjusted P	
Cp	0,03808	0,00262	0,07304	0,03452	0,18987	**SCALE 1 (0.1-0.2 Hz)**
Lp	0,14724	-0,21210	0,57595	0,37270	0,51246	
E.global	-0,03549	-0,05620	-0,01530	0,00114	**0,01257**	
kmax	-0,00540	-0,01577	0,00409	0,23495	0,43074	
kappa	-0,20935	-0,94629	0,46821	0,51482	0,56630	
Bmax	-0,02238	-0,05831	0,01911	0,32334	0,50810	
diameter	0,60417	-0,52685	2,00000	0,18425	0,40535	
Ecc	0,13207	-0,65023	0,96280	0,70176	0,70176	
assortativity	0,07303	-0,00176	0,14758	0,05512	0,20209	
thr	0,04262	-0,00441	0,09583	0,07647	0,21029	
strength	-0,02068	-0,05407	0,01853	0,25759	0,45078	
diversity	0,01146	0,00648	0,01651	0,00001	**0,00019**	
rzero	0,04168	-0,01975	0,10343	0,12638	0,35387	
Cp	0,02867	0,00146	0,06092	0,03452	**0,04747**	**SCALE 2 (0.05-0.1 Hz)**
Lp	0,57335	0,21706	0,90915	0,00163	**0,00593**	
E.global	-0,03730	-0,06557	-0,00869	0,01317	**0,02415**	
kmax	-0,01012	-0,01706	-0,00405	0,00215	**0,00593**	
kappa	-0,94466	-1,39061	-0,46604	0,00016	**0,00173**	
Bmax	0,02262	-0,01670	0,06494	0,30483	0,33531	
diameter	1,81250	0,81250	3,00000	0,00093	**0,00509**	
Ecc	1,17626	0,36950	2,03111	0,00375	**0,00825**	
Ass	0,07449	0,00844	0,14458	0,02628	**0,04129**	
thr	0,00439	-0,03531	0,04258	0,81087	0,81087	
strength	-0,04348	-0,08428	-0,00587	0,02562	**0,04061**	
diversity	0,00818	0,00473	0,01162	0,00000	**0,00006**	
rzero	0,07991	0,01578	0,13949	0,01000	**0,02799**	
Cp	0,01937	-0,01410	0,04933	0,26994	0,72176	**SCALE 3 (0.025-0.05 Hz)**
Lp	0,01193	-0,29858	0,33940	0,94658	0,94658	
E.global	-0,01714	-0,04570	0,00870	0,22287	0,72176	
kmax	-0,00578	-0,01252	0,00102	0,17641	0,72176	
kappa	-0,57302	-1,21094	0,00361	0,05389	0,59277	
Bmax	-0,01280	-0,05325	0,02517	0,44910	0,82334	
diameter	-0,13603	-1,13603	0,85417	0,66826	0,87567	
Ecc	-0,11740	-0,79626	0,55021	0,75208	0,87567	
Ass	-0,01238	-0,08018	0,06214	0,79606	0,87567	
thr	0,00698	-0,02585	0,04163	0,63895	0,87567	

strength	-0,00800	-0,06312	0,05292	0,81830	0,81830	
diversity	0,00364	-0,00266	0,00991	0,28703	0,50231	
rzero	0,01044	-0,05878	0,07106	0,74482	0,80211	
Cp	-0,01511	-0,04618	0,01490	0,32807	0,45110	**SCALE 4 (0.013-0.025 Hz)**
Lp	0,33814	0,02203	0,68193	0,03537	0,28512	
E.global	0,00101	-0,02300	0,02362	0,96183	0,96183	
kmax	-0,00578	-0,01391	0,00159	0,11085	0,28512	
kappa	-0,46243	-1,08819	0,10698	0,10824	0,28512	
Bmax	0,02706	-0,00967	0,06794	0,14950	0,28512	
diameter	0,72283	-0,34783	1,75000	0,15552	0,28512	
Ecc	0,74760	-0,01851	1,43487	0,06298	0,28512	
Ass	-0,00411	-0,05995	0,04466	0,90856	0,96183	
thr	-0,01231	-0,03660	0,01092	0,30031	0,45110	
strength	0,00678	-0,05874	0,08161	0,90098	1,00000	
diversity	-0,00007	-0,01233	0,01199	1,00000	1,00000	
rzero	-0,01035	-0,06976	0,05427	0,68581	1,00000	

Legend: Estimate = estimated median of the pairwise differences between subjects in bvFTD against HCs; Lower CI95% = lower bound of the confidence interval (95%); Upper CI95% = upper bound of the confidence interval (95%); P-value = nominal P-value of the Wilcoxon test; Adjusted P = Benjamini-Hochberg adjusted P-value; Cp = clustering coefficient; Lp = average path length; E.global = global efficiency; kmax = maximum degree; kappa = digree divergence; Bmax = maximum betweenness; Ecc = eccentricity; Ass = assortativity; thr = average group wavelet correlation threshold induced by the fixed edge density threshold; rzero = zero correlation. Published in Saba et al., 2019.

Table 2A. Wilcoxon rank sum tests using Extended Bayesian Information Criterion (EBIC)-based global connectivity parameters at every scale. Wilcoxon rank sum tests in bvFTD subjects versus HCs are shown in the table. The networks from which global parameters are extracted, are built from binarized wavelet correlation matrices, using optimal EBIC correlation thresholds. Tests estimate differences (Estimate column) are calculated for each scale (1 to 4), for every global connectivity parameter. Estimates are adjusted for age, sex, and age*sex interaction. Strength, diversity, and rzero are directly derived from the correlation matrix, while the other metrics refer to the resulting networks.

	Estimate	Lower CI95%	Upper CI95%	P-value	Adjusted P	
Cp	-0,00081	-0,03305	0,03605	0,96183	0,96183	**SCALE 1 (0.1-0.2 Hz)**
Lp	0,04357	-0,01671	0,11575	0,13629	0,29984	
E.global	-0,00905	-0,01811	-0,00016	0,04698	0,12921	
kmax	-0,00529	-0,00840	-0,00236	0,00027	**0,00296**	
kappa	-1,36079	-2,16925	-0,51956	0,00152	**0,00834**	
Bmax	-0,00655	-0,01594	0,00552	0,27840	0,51040	
diameter	0,01790	-0,10417	0,17279	0,54760	0,75295	
Ecc	0,10084	-0,17290	0,36841	0,47244	0,74240	
assortativity	0,05493	0,01793	0,09566	0,00363	**0,01331**	
thr	0,01164	-0,03940	0,06382	0,63721	0,77881	
strength	-0,02068	-0,05407	0,01853	0,25759	0,45078	
diversity	0,01146	0,00648	0,01651	0,00001	**0,00019**	
rzero	0,04168	-0,01975	0,10343	0,12638	0,35387	
Cp	-0,00889	-0,04388	0,02701	0,53357	0,64162	**SCALE 2 (0.05-0.1 Hz)**
Lp	0,06249	-0,00860	0,13004	0,08317	0,18297	
E.global	-0,00572	-0,01502	0,00358	0,30483	0,55886	
kmax	-0,00678	-0,00977	-0,00353	0,00006	**0,00031**	
kappa	-2,12916	-3,14915	-1,13648	0,00005	**0,00031**	
Bmax	-0,01039	-0,02096	0,00035	0,05764	0,15852	
diameter	0,00000	-0,70833	0,29167	0,58329	0,64162	
Ecc	0,01691	-0,27581	0,28525	0,90856	0,90856	
Ass	0,03917	0,01116	0,07172	0,00834	**0,03056**	
thr	-0,01459	-0,06613	0,02581	0,40032	0,59403	
strength	-0,04348	-0,08428	-0,00587	0,02562	**0,04061**	
diversity	0,00818	0,00473	0,01162	0,00000	**0,00006**	
rzero	0,07991	0,01578	0,13949	0,01000	**0,02799**	
Cp	0,01214	-0,01868	0,04419	0,44336	0,69671	**SCALE 3 (0.025-0.05 Hz)**
Lp	-0,01482	-0,09378	0,05667	0,58517	0,80461	
E.global	0,00594	-0,00435	0,01543	0,27415	0,50261	
kmax	-0,00277	-0,00585	0,00036	0,07810	0,25353	
kappa	-1,01170	-2,00366	0,18907	0,09219	0,25353	
Bmax	0,00099	-0,00907	0,01086	0,86321	0,93136	
diameter	-0,39583	-0,84926	0,15074	0,21264	0,46781	
Ecc	-0,01529	-0,35564	0,31505	0,93136	0,93136	
Ass	-0,03247	-0,06879	0,00191	0,05894	0,25353	

thr	0,00266	-0,04567	0,05161	0,84630	0,93136	
strength	-0,00800	-0,06312	0,05292	0,81830	0,81830	
diversity	0,00364	-0,00266	0,00991	0,28703	0,50231	
rzero	0,01044	-0,05878	0,07106	0,74482	0,80211	
Cp	0,00177	-0,02842	0,03109	0,93897	1,00000	**SCALE 4 (0.013-0.025 Hz)**
Lp	0,03591	-0,05319	0,12824	0,39367	1,00000	
E.global	-0,00293	-0,01270	0,00852	0,63895	1,00000	
kmax	0,00134	-0,00220	0,00433	0,40441	1,00000	
kappa	0,62218	-0,73929	1,99713	0,31864	1,00000	
Bmax	0,00590	-0,00822	0,01888	0,39367	1,00000	
diameter	0,00000	-0,59069	0,63949	0,92181	1,00000	
Ecc	0,10303	-0,23022	0,43788	0,61854	1,00000	
Ass	0,01550	-0,02494	0,05343	0,49642	1,00000	
thr	0,00547	-0,03988	0,04301	0,85003	1,00000	
strength	0,00678	-0,05874	0,08161	0,90098	1,00000	
diversity	-0,00007	-0,01233	0,01199	1,00000	1,00000	
rzero	-0,01035	-0,06976	0,05427	0,68581	1,00000	

Legend: Estimate = estimated median of the pairwise differences between subjects in bvFTD against HCs; Lower CI95% = lower bound of the confidence interval (95%); Upper CI95% = upper bound of the confidence interval (95%); P-value = nominal P-value of the Wilcoxon test; Adjusted P = Benjamini-Hochberg adjusted P-value; Cp = clustering coefficient; Lp = average path length; E.global = global efficiency; kmax = maximum degree; kappa = digree divergence; Bmax = maximum betweenness; Ecc = eccentricity; Ass = assortativity; thr = average group wavelet correlation threshold induced by the fixed edge density threshold; rzero = zero correlation. Published in Saba et al., 2019.

Table 3A. Wilcoxon rank sum tests using spectral analysis-derived global connectivity parameters at every scale. Wilcoxon rank sum tests in bvFTD subjects versus HCs are shown in the table. The networks from which global parameters are extracted, are built from binarized wavelet correlation matrices. Correlation thresholds are based on optimal spectral clustering. Tests estimate differences (Estimate column) are calculated for each scale (1 to 4), for every global connectivity parameter. Estimates are adjusted for age, sex, and age*sex interaction. Strength, diversity, and rzero are directly derived from the correlation matrix, while the other metrics refer to the resulting networks.

	Estimate	Lower CI95%	Upper CI95%	P-value	Adjusted P	
Cp	-0,00044	-0,03789	0,03534	0,97478	1,00000	**SCALE 1 (0.1-0.2 Hz)**
Lp	-0,17387	-0,55474	0,16620	0,34695	1,00000	
E.global	-0,00190	-0,05566	0,04971	0,89103	1,00000	
kmax	0,00328	-0,00373	0,01067	0,34695	1,00000	
kappa	0,10518	-1,79541	2,41945	0,92444	1,00000	
Bmax	-0,00233	-0,05542	0,04946	0,94120	1,00000	
diameter	-0,50000	-1,35417	0,91667	0,32262	1,00000	
Ecc	-0,29214	-1,20279	0,47997	0,49272	1,00000	
assortativity	-0,01203	-0,07530	0,07203	0,72793	1,00000	
thr	0,00363	-0,01218	0,03077	0,46284	1,00000	
strength	-0,02068	-0,05407	0,01853	0,25759	0,45078	
diversity	0,01146	0,00648	0,01651	0,00001	**0,00019**	
rzero	0,04168	-0,01975	0,10343	0,12638	0,35387	
Cp	-0,03779	-0,10713	0,02780	0,26153	0,48779	**SCALE 2 (0.05-0.1 Hz)**
Lp	0,21096	-0,16293	0,53858	0,33391	0,52471	
E.global	-0,07935	-0,18444	0,01095	0,08486	0,24272	
kmax	0,00617	-0,00957	0,02401	0,52333	0,71957	
kappa	-6,59000	-15,87560	-0,06712	0,04516	0,24272	
Bmax	0,00020	-0,02571	0,02792	0,98739	0,98739	
diameter	0,00000	-1,00000	1,00000	0,88474	0,97321	
Ecc	-0,20007	-0,85746	0,52850	0,66934	0,81809	
Ass	0,08032	0,01592	0,14445	0,01523	0,16750	
thr	0,04673	-0,00382	0,08849	0,08826	0,24272	
strength	-0,04348	-0,08428	-0,00587	0,02562	**0,04061**	
diversity	0,00818	0,00473	0,01162	0,00000	**0,00006**	
rzero	0,07991	0,01578	0,13949	0,01000	**0,02799**	
Cp	-0,00228	-0,05875	0,05393	0,93873	1,00000	**SCALE 3 (0.025-0.05 Hz)**
Lp	0,10288	-0,18806	0,42310	0,48635	1,00000	
E.global	0,00817	-0,08112	0,09296	0,87369	1,00000	
kmax	-0,00022	-0,00984	0,00945	0,96830	1,00000	
kappa	-2,28685	-10,92862	8,71305	0,72052	1,00000	
Bmax	0,00759	-0,00799	0,02336	0,35991	1,00000	
diameter	0,21196	-0,75833	1,32500	0,31330	1,00000	
Ecc	0,21936	-0,32813	0,97630	0,40896	1,00000	
Ass	-0,01365	-0,08818	0,05636	0,67637	1,00000	
thr	0,01656	-0,03002	0,06154	0,48163	1,00000	

strength	-0,00800	-0,06312	0,05292	0,81830	0,81830	
diversity	0,00364	-0,00266	0,00991	0,28703	0,50231	
rzero	0,01044	-0,05878	0,07106	0,74482	0,80211	
Cp	0,02650	-0,01824	0,06949	0,25759	0,78967	**SCALE 4 (0.013-0.025 Hz)**
Lp	-0,08449	-0,31113	0,14897	0,49037	0,78967	
E.global	0,02490	-0,03979	0,07586	0,42085	0,78967	
kmax	-0,00129	-0,00422	0,00231	0,50252	0,78967	
kappa	3,60569	-4,67464	11,76903	0,36756	0,78967	
Bmax	0,00631	-0,00878	0,02156	0,37787	0,78967	
diameter	-0,07353	-1,00000	0,51087	0,70693	0,97203	
Ecc	-0,00215	-0,53531	0,52410	0,99236	0,99236	
Ass	0,00637	-0,04651	0,06474	0,84819	0,99236	
thr	0,00000	-0,03077	0,03077	0,91043	0,99236	
strength	0,00678	-0,05874	0,08161	0,90098	1,00000	
diversity	-0,00007	-0,01233	0,01199	1,00000	1,00000	
rzero	-0,01035	-0,06976	0,05427	0,68581	1,00000	

Legend: Estimate = estimated median of the pairwise differences between subjects in bvFTD against HCs; Lower CI95% = lower bound of the confidence interval (95%); Upper CI95% = upper bound of the confidence interval (95%); P-value = nominal P-value of the Wilcoxon test; Adjusted P = Benjamini-Hochberg adjusted P-value; Cp = clustering coefficient; Lp = average path length; E.global = global efficiency; kmax = maximum degree; kappa = digree divergence; Bmax = maximum betweenness; Ecc = eccentricity; Ass = assortativity; thr = average group wavelet correlation threshold induced by the fixed edge density threshold; rzero = zero correlation. Published in Saba et al., 2019.

Table 4A. Wilcoxon rank sum tests using scale free model-based global connectivity parameters at every scale. Wilcoxon rank sum tests in bvFTD subjects versus HCs are shown in the table. The networks from which global parameters are extracted, are built from binarized wavelet correlation matrices. Correlation thresholds are based on scale free fitting optimization. Tests estimate differences (Estimate column) are calculated for each scale (1 to 4), for every global connectivity parameter. Estimates are adjusted for age, sex, and age*sex interaction. Strength, diversity, and rzero are directly derived from the correlation matrix, while the other metrics refer to the resulting networks.

	Estimate	Lower CI95%	Upper CI95%	P-value	Adjusted P	
Cp	0,02813	-0,00820	0,07969	0,10579	0,15868	**SCALE 1 (0.1-0.2 Hz)**
Lp	-0,18498	-0,53012	0,18509	0,34408	0,45877	
E.global	-0,05428	-0,09635	-0,01544	0,00694	0,04166	
kmax	0,00812	-0,00181	0,02017	0,09764	0,15868	
kappa	-1,44918	-3,32698	0,19650	0,09503	0,15868	
Bmax	-0,03544	-0,07544	0,00176	0,07399	0,15868	
diameter	-0,54444	-1,54444	1,00000	0,69932	0,76289	
Ecc	-0,72001	-1,44239	0,11737	0,08054	0,15868	
assortativity	0,08731	-0,00124	0,16841	0,05195	0,15868	
thr	0,09231	0,03282	0,14832	0,00191	0,02293	
strength	-0,02068	-0,05407	0,01853	0,25759	0,45078	
diversity	0,01146	0,00648	0,01651	0,00001	**0,00019**	
rzero	0,04168	-0,01975	0,10343	0,12638	0,35387	
Cp	0,01192	-0,02301	0,04884	0,46755	0,60642	**SCALE 2 (0.05-0.1 Hz)**
Lp	0,10282	-0,17608	0,50980	0,41980	0,60642	
E.global	-0,05436	-0,09517	-0,00523	0,03629	0,21772	
kmax	-0,00701	-0,01542	0,00101	0,09670	0,38682	
kappa	-0,94650	-2,58975	0,37482	0,14328	0,42983	
Bmax	-0,01385	-0,05558	0,03280	0,55589	0,60642	
diameter	0,51299	-0,48701	1,55385	0,32868	0,60642	
Ecc	0,21861	-0,52175	1,04883	0,55589	0,60642	
Ass	0,08514	0,01340	0,16193	0,02111	0,21772	
thr	0,01259	-0,02551	0,06154	0,38588	0,60642	
strength	-0,04348	-0,08428	-0,00587	0,02562	**0,04061**	
diversity	0,00818	0,00473	0,01162	0,00000	**0,00006**	
rzero	0,07991	0,01578	0,13949	0,01000	**0,02799**	
Cp	0,01381	-0,02570	0,04735	0,42790	1,00000	**SCALE 3 (0.025-0.05 Hz)**
Lp	0,08310	-0,26201	0,44412	0,61341	1,00000	
E.global	-0,00865	-0,05074	0,03845	0,76949	1,00000	
kmax	-0,00620	-0,01441	0,00223	0,15517	1,00000	
kappa	-0,00563	-1,76322	1,40263	0,99503	1,00000	
Bmax	-0,00196	-0,04783	0,04616	0,91560	1,00000	
diameter	0,50000	-0,71131	1,28869	0,22841	1,00000	
Ecc	0,36424	-0,45544	1,10533	0,40633	1,00000	
Ass	0,00755	-0,05893	0,06842	0,84676	1,00000	
thr	-0,00577	-0,03984	0,03077	0,73863	1,00000	

strength	-0,00800	-0,06312	0,05292	0,81830	0,81830	
diversity	0,00364	-0,00266	0,00991	0,28703	0,50231	
rzero	0,01044	-0,05878	0,07106	0,74482	0,80211	
Cp	-0,00044	-0,03789	0,03534	0,97478	1,00000	**SCALE 4 (0.013-0.025 Hz)**
Lp	-0,17387	-0,55474	0,16620	0,34695	1,00000	
E.global	-0,00190	-0,05566	0,04971	0,89103	1,00000	
kmax	0,00328	-0,00373	0,01067	0,34695	1,00000	
kappa	0,10518	-1,79541	2,41945	0,92444	1,00000	
Bmax	-0,00233	-0,05542	0,04946	0,94120	1,00000	
diameter	-0,50000	-1,35417	0,91667	0,32262	1,00000	
Ecc	-0,29214	-1,20279	0,47997	0,49272	1,00000	
Ass	-0,01203	-0,07530	0,07203	0,72793	1,00000	
thr	0,00363	-0,01218	0,03077	0,46284	1,00000	
strength	0,00678	-0,05874	0,08161	0,90098	1,00000	
diversity	-0,00007	-0,01233	0,01199	1,00000	1,00000	
rzero	-0,01035	-0,06976	0,05427	0,68581	1,00000	

Legend: Estimate = estimated median of the pairwise differences between subjects in bvFTD against HCs; Lower CI95% = lower bound of the confidence interval (95%); Upper CI95% = upper bound of the confidence interval (95%); P-value = nominal P-value of the Wilcoxon test; Adjusted P = Benjamini-Hochberg adjusted P-value; Cp = clustering coefficient; Lp = average path length; E.global = global efficiency; kmax = maximum degree; kappa = digree divergence; Bmax = maximum betweenness; Ecc = eccentricity; Ass = assortativity; thr = average group wavelet correlation threshold induced by the fixed edge density threshold; rzero = zero correlation. Published in Saba et al., 2019.

Table 5A. Betweenness and degree centrality in bvFTD versus HCs. Beetweenness (B) and degree (K) centrality, together with their differences (bvFTD-HC), are reported for each area of the AAL 116 atlas. Nodes and hubs (in either group) gaining betweenness (b > 435) are in yellow and light red, respectively. Nodes and hubs (in either group) loosing betweenness (b < -435) are in cyan and green, respectively. White nodes show betweenness differences within the threshold (-435 ≤ b ≤ 435). K1 = bvFTD degree centrality; K0 = HC degree centrality; B1 = bvFTD betweenness centrality; B0 = HC betweenness centrality; k = degree difference; b = betweenness difference; SCGM = Subcortical Gray Matter. Published in Saba et al., 2019.

Area	Lobe	K1	K0	k	B1	B0	b
45	Occipital	2	1	1	2940	0	2940
49	Occipital	2	1	1	2911	0	2911
51	Occipital	4	5	-1	3189	442	2747
60	Parietal	2	2	0	3135	436	2699
19	Frontal	2	1	1	2511	0	2511
53	Occipital	3	1	2	2461	0	2461
3	Frontal	2	1	1	2460	0	2460
58	Parietal	4	2	2	3165	840	2325
20	Frontal	2	3	-1	2560	440	2120
23	**Frontal**	**6**	**4**	**2**	**2686**	**1141**	**1545**
69	Parietal	4	5	-1	3443	1907	1536
70	Parietal	5	2	3	3384	2136	1248
24	Frontal	3	2	1	1220	112	1108
25	Frontal	2	1	1	927	0	927
67	**Parietal**	**8**	**12**	**-4**	**3745**	**2866**	**879**
14	Frontal	2	1	1	832	0	832
50	Occipital	2	1	1	832	0	832
8	Frontal	2	2	0	927	112	815
12	Frontal	4	1	3	749	0	749
57	Parietal	3	1	2	741	0	741
27	Frontal	2	1	1	735	0	735
36	Limbic	2	1	1	735	0	735
46	Occipital	2	1	1	735	0	735
111	Cerebellum	2	1	1	735	0	735
44	Occipital	3	1	2	644	0	644
68	Parietal	3	1	2	641	0	641
86	Temporal	3	1	2	436	0	436
112	Cerebellum	2	1	1	432	0	432
48	Occipital	2	1	1	327	0	327
97	Cerebellum	4	2	2	647	330	317
80	Temporal	3	1	2	221	0	221
29	Insula	2	1	1	220	0	220
104	Cerebellum	2	1	1	220	0	220
1	Frontal	3	2	1	329	112	217
18	Frontal	2	2	0	327	112	215
5	Frontal	2	1	1	111	0	111
88	Temporal	2	1	1	111	0	111
7	Frontal	3	2	1	221	112	109
9	Frontal	1	1	0	0	0	0
11	Frontal	1	1	0	0	0	0
13	Frontal	1	1	0	0	0	0
15	Frontal	1	1	0	0	0	0

16	Frontal	1	1	0	0	0	0
17	Frontal	1	1	0	0	0	0
21	Frontal	1	1	0	0	0	0
30	Insula	1	1	0	0	0	0
31	Limbic	1	1	0	0	0	0
35	Limbic	1	1	0	0	0	0
39	Limbic	1	1	0	0	0	0
41	Limbic	1	1	0	0	0	0
42	Limbic	0	1	-1	0	0	0
43	Occipital	1	1	0	0	0	0
52	Occipital	1	1	0	0	0	0
59	Parietal	1	1	0	0	0	0
61	Parietal	1	1	0	0	0	0
64	Parietal	1	1	0	0	0	0
71	SCGM	1	1	0	0	0	0
72	SCGM	1	1	0	0	0	0
75	SCGM	1	1	0	0	0	0
76	SCGM	1	1	0	0	0	0
77	SCGM	1	1	0	0	0	0
87	Temporal	1	1	0	0	0	0
89	Temporal	1	1	0	0	0	0
90	Temporal	1	1	0	0	0	0
91	Cerebellum	1	1	0	0	0	0
92	Cerebellum	1	1	0	0	0	0
93	Cerebellum	1	1	0	0	0	0
94	Cerebellum	1	1	0	0	0	0
96	Cerebellum	1	1	0	0	0	0
100	Cerebellum	4	2	2	330	330	0
101	Cerebellum	1	1	0	0	0	0
103	Cerebellum	1	1	0	0	0	0
105	Cerebellum	1	1	0	0	0	0
106	Cerebellum	1	1	0	0	0	0
107	Cerebellum	0	0	0	0	0	0
108	Cerebellum	0	0	0	0	0	0
109	Cerebellum	1	1	0	0	0	0
113	Cerebellum	1	1	0	0	0	0
116	Cerebellum	1	1	0	0	0	0
22	Frontal	2	2	0	111	112	-1
55	Occipital	2	2	0	111	112	-1
73	SCGM	2	2	0	111	112	-1
74	SCGM	2	2	0	111	112	-1
83	Temporal	2	2	0	111	112	-1
98	Cerebellum	2	2	0	111	112	-1
110	Cerebellum	2	2	0	111	112	-1
115	Cerebellum	2	2	0	111	112	-1
37	Limbic	3	3	0	221	223	-2
114	Cerebellum	2	2	0	220	222	-2
6	Frontal	3	3	0	329	332	-3
79	Temporal	3	4	-1	435	441	-6
26	Frontal	2	2	0	832	840	-8
10	Frontal	1	2	-1	0	112	-112
28	Frontal	3	4	-1	644	756	-112

33	Limbic	1	2	-1	0	112	-112
65	Parietal	1	2	-1	0	112	-112
81	Temporal	2	3	-1	535	647	-112
102	Cerebellum	2	3	-1	111	223	-112
84	Temporal	1	2	-1	0	222	-222
95	Cerebellum	1	2	-1	0	222	-222
34	Limbic	1	3	-2	0	223	-223
85	Temporal	1	3	-2	0	223	-223
38	Limbic	2	3	-1	111	439	-328
82	Temporal	1	2	-1	0	330	-330
62	Parietal	1	3	-2	0	332	-332
56	Occipital	2	2	0	111	642	-531
40	Limbic	1	2	-1	0	540	-540
63	Parietal	1	2	-1	0	742	-742
32	Limbic	2	3	-1	111	1410	-1299
4	Frontal	2	2	0	111	1470	-1359
99	**Cerebellum**	**11**	**15**	**-4**	**2516**	**4050**	**-1534**
66	Parietal	1	2	-1	0	1552	-1552
2	Frontal	2	4	-2	220	2132	-1912
78	SCGM	2	2	0	111	2592	-2481
47	**Occipital**	**2**	**6**	**-4**	**111**	**3024**	**-2913**
54	**Occipital**	**2**	**11**	**-9**	**220**	**4274**	**-4054**